

Topological design of 2D Phononic Bandgap

Crystals with the Six-fold Symmetry

or the Reduced Symmetry

Zhaoxuan Zhang

Master of Science (by Research)



Swinburne University of Technology

2017

Abstract

Phononic crystals (PnCs) are novel artificial periodical materials which offer great flexibility for manipulating acoustic and elastic waves. Well-designed PnCs may give rise to phononic bandgaps which prevent the propagation of acoustic and elastic waves in a particular frequency range on a wavelength scale and can be used for many applications. The occurrence of bandgaps highly depends on the spatial distribution of the base materials of the PnCs. This thesis investigates the topology optimization of two-dimensional solid PnCs for maximizing specified bandgaps with different lattices and symmetries. The optimization algorithm based on the bi-directional evolutionary structural optimization (BESO) method is established and verified by numerical examples. Many novel patterns with large band gaps for out-of-plane, in-plane, and complete waves are obtained and discussed. Compared with the most commonly used method in the optimization of phononic crystals: Genetic Algorithm, the proposed gradient-based BESO method is much more efficient and able to present solutions with wider bandgaps.

The results show that the structures consisting of the heavier and stiffer metal material (Au or Pb) isolated and embedded in the lighter and softer material (Epoxy) can exhibit broad bandgaps. The complexity of the optimized topologies increases with the band order. For the out-of-plane waves, the number of inclusions in the optimized structure is equal to the band order while for the in-plane waves, the broad bandgap appears when the number of inclusions equals three times the band order.

In the investigation of the effect of the lattice type on the bandgap size, the majority of the results with the hexagonal lattice exhibit the greater bandgap than those with the square lattice. However, the gap size for PnCs with the hexagonal lattice may not always larger than that with the square lattice. At some bands, the gap size for PnCs with the square lattice is larger than that with the hexagonal lattice.

Symmetry reduction has a beneficial influence on the topology characteristics of the optimized structures. Generally, asymmetric design exhibits a large bandgap than its symmetric counterpart. However, in some cases, both symmetric and asymmetric designs have the same topologies and bandgap sizes which demonstrate the symmetric ones tend to be truly optimal. For the out-of-plane waves, the largest bandgap is the first bandgap with the six-fold symmetric

hexagonal lattice. For the in-plane wave, the phononic crystal with the asymmetric hexagonal lattice for the fifteenth bandgap has the greatest bandgap size. For the complete bandgap, the optimized asymmetric square-latticed phononic structure has the biggest bandgap between the second out-of-plane bandgap and the third in-plane bandgap.

For some specified bandgaps of in-plane waves, topology optimization starting from a random initial design is still difficult to obtain the satisfactory solutions due to the coupled longitudinal and transverse waves. From our research, the in-plane bandgap for both square and hexagonal latticed PnCs can be easily achieved by introducing initial guess designs based on the PCVTs.

Keywords: Phononic crystals; Band gap; Topological optimization; Bi-directional evolutionary structural optimization; Lattice type; Symmetry

Declaration

I hereby declare that this thesis-“Topological design of 2D Phononic Bandgap Crystals with the Six-fold Symmetry or the Reduced Symmetry” contains no material that has been accepted for the award of any other degree or certificate in any educational institution and, to the best of my knowledge and belief, it contains no material previously published or written by another person, except where due reference is made in the text of the thesis.



Name: Zhaoxuan Zhang

Date: 08/03/2018

Acknowledgement

I would like to express my deep appreciation to my supervisor, Prof. Xiaodong Huang, for the dedicated guidance and support he presented to my studies over the past two years.

I wish to thank my colleagues at the Swinburne University of Technology for providing a friendly and collaborative atmosphere. I would especially like to thank Yang-fan Li and Dr. Fei Meng, who provided significant collaborations and help in my research.

Also, I have to thank the financial support from the Australian Research Council Future Fellowship (FT130101094) and the Swinburne University of Technology for the duration of my graduate studies, which benefited the completion of my research.

Finally, to my loving parents, Zheng Zhang and Hongyun Han, who emphasized education and kindled my interest in science from its earliest stages, and to the rest of my family who showed unconditional support, thank you.

Table of Contents

Abstract.....	I
Declaration.....	III
Acknowledgement.....	IV
List of figures.....	VIII
List of tables.....	XIV
Chapter 1. Introduction.....	1
1.1 Research background.....	1
1.2 Gap of knowledge.....	2
1.3 Outline of this thesis.....	3
Chapter 2. Literature review.....	4
2.1 Phononic crystals.....	4
2.1.1 Concept of phononic crystals.....	4
2.1.2 Engineering bandgap of PnCs.....	5
2.1.3 Functional phononic crystals.....	10
2.2 Topology optimization.....	14
2.2.1 Genetic algorithm.....	15
2.2.2 Solid isotropic material with penalization.....	16
2.2.3 Evolutional structural optimization/Bi-directional evolutionary structural optimization.....	16
2.3 Topology optimization of phononic bandgap crystals.....	17

Chapter 3. Numerical analysis and topology optimization for phononic crystals	20
3.1 Numerical analysis.....	20
3.2 Topology optimization.....	23
3.2.1 Objective function.....	23
3.2.2 Material interpolation scheme	24
3.2.3 Sensitivity analysis.....	24
3.2.4 Sensitivity filter scheme	25
3.2.5 Average sensitivity numbers with history	26
3.2.6 Update of topology.....	26
3.2.7 BESO procedure	27
Chapter 4. Topology optimization for 2D phononic bandgap crystals with six-fold symmetric hexagonal lattice	29
4.1 Introduction	29
4.2 Hexagonal lattice and six-fold symmetry.....	30
4.3 Optimization results and discussion.....	31
4.3.1 Bandgaps for out-of-plane waves	31
4.3.2 Bandgaps for in-plane waves.....	35
4.3.3 Complete bandgaps for both out-of-plane and in-plane waves	38
4.3.4 Wave transmission for finite PnCs.....	39
4.4 Conclusions	42
Chapter 5. Topology optimization for the 2D phononic bandgap crystals with the reduced symmetry	43

5.1. Introduction	43
5.2 Lattice types and symmetries	44
5.3. Optimization results and discussion.....	45
5.3.1 Square lattice.....	46
5.3.2 Hexagonal lattice.....	54
5.4 Conclusion.....	59
Chapter 6. Conclusion of current and future works	61
6.1 Conclusion of current works	61
6.2 Future works.....	61
Appendix 1	63
Appendix 2	67
References:.....	71
List of publications	82

List of figures

2.1. 1D, 2D and 3D PnCs made of two different elastic materials arranged periodically. Different colors represent different base materials. [42].....	5
2.2. PnCs for (a) surface waves [51]; (b) plate waves [52].....	7
2.3. A locally resonant phononic crystal [57].....	7
2.4. (a) One unit cell of a 3D periodic foundation; (b) the cross-section of a unit cell; (c) frequency bandgap of 3D periodic foundation [90]; (d) the sketch map of a vibration isolation structure [88].....	11
2.5. Transmission spectra in the frequency range of the bandgap and displacement fields at 290 kHz through (a) a straight and (b) a bent waveguide [7].	11
2.6. (a) Schematic diagram of the positive and negative refraction. two snapshots of the outgoing pulses in the negative refraction experiment, obtained by digitally filtering original pulses at the frequency of (b) 0.85 MHz and (c) 0.75 MHz [102].....	12
2.7. (a) An acoustic diode made of a 1D phononic crystal (alternating layers of glass and water) coupled to a nonlinear acoustic medium [83]. (b) A sonic crystal-based acoustic diode [107]. (c) An inverted bi-prism [108]. (d) Schematic model of the directional waveguide [109].	14
3.1. (a) A typical 2D phononic bandgap crystal with the hexagonal lattice constant a , and the dashed red rhombus denotes its primitive unit cell. (b) Six-fold symmetry of the unit cell. (c) Irreducible Brillouin zone of the hexagonal lattice (Γ -X-M- Γ). (d) The	

band diagram of the phononic bandgap crystal.	23
3.2. Schematic illustration of the filter scheme [114].	26
3.3. Flowchart of the proposed BESO method.....	28
4.1. (a) A typical 2D phononic bandgap crystal with the hexagonal lattice constant a , and the dashed red rhombus denotes its primitive unit cell. (b) Six-fold symmetry of the unit cell. (c) Irreducible Brillouin zone of the hexagonal lattice (Γ -X-M- Γ).	30
4.2. Optimized hexagonal-latticed phononic bandgap crystals and their band diagrams for out-of-plane waves; (a) the first bandgap; (b) the second bandgap; (c) the third bandgap; (d) the fourth bandgap; (e) the fifth bandgap; (f) the sixth bandgap; (g) the seventh bandgap; (h) the eighth bandgap; (i) the ninth bandgap; (j) the tenth bandgap.	33
4.3. Different optimized results from three initial topologies	35
4.4. Optimized hexagonal-latticed phononic bandgap crystals and their band diagrams for in-plane waves; (a) the third bandgap; (b) the fifth bandgap; (c) the sixth bandgap; (d) the ninth bandgap.....	36
4.5. (a) Three-fold symmetry and selection of the primitive unit cell (shaded area). (b) Irreducible Brillouin zone of the hexagonal lattice with the three-fold symmetry (Γ -X-M (M')- Γ). (c) Optimized hexagonal-latticed phononic crystal with the three-fold symmetry and its band diagrams for in-plane waves.	37
4.6. Optimized hexagonal-latticed phononic bandgap crystals and their band diagrams for	

in-plane waves with the third bandgap at the volume fraction from 70% to 20%.....	38
4.7. Optimized hexagonal-latticed phononic bandgap crystals and their band diagrams for the complete bandgap; (a) the third in-plane bandgap and the first out-of-plane bandgap; (b) the fifth in-plane bandgap and the third out-of-plane bandgap; (c) the sixth in-plane bandgap and the second out-of-plane bandgap; (d) the ninth in-plane bandgap and the third out-of-plane bandgap..	39
4.8. Model for transmission analysis in COMSOL Multiphysics.....	39
4.9. The transmission spectrum of waves propagating along the Γ -X direction for the phononic structure shown in Figure 4.8.	40
4.10. The field distributions of elastic waves at the normalized frequency, 0.58: (a) displacement distribution of the out-of-plane wave; (b) acceleration distribution of the in-plane P wave; and (c) acceleration distribution of the in-plane S wave.....	41
4.11. The field distributions of elastic waves at the normalized frequency, 0.86: (a) displacement distribution of the out-of-plane wave; (b) acceleration distribution of the in-plane P wave; and (c) acceleration distribution of the in-plane S wave.....	41
4.12. The field distributions of elastic waves at the normalized frequency, 1.12: (a) displacement distribution of the out-of-plane wave; (b) acceleration distribution of the in-plane P wave; and (c) acceleration distribution of the in-plane S wave.....	41
5.1. (a) C_{4v} square lattice; (b) C_1 square lattice; (c) C_{6v} hexagonal lattice; (d) C_1 hexagonal lattice. Left: unit cells (grey area) and symmetry. Right: the first Brillouin zone and	

irreducible Brillouin zone (grey area) in the reciprocal lattice.	44
5.2. Optimized phononic bandgap crystals with the C_{4v} square lattice from the first bandgap to the fifteenth bandgap for the out-of-plane waves.....	47
5.3. Optimized phononic bandgap crystals with the C_1 square lattice from the first bandgap to the fifteenth bandgap for the out-of-plane waves.....	48
5.4. Relative phononic bandgap sizes with the C_1 and C_{4v} square lattice from the first bandgap to the fifteenth bandgap for the out-of-plane waves.....	49
5.5. (a) PCVT at $n=9$; (b) PCVT-based initial design for the phononic bandgap crystal with the C_1 square lattice for the ninth bandgap.....	50
5.6. Optimized phononic bandgap crystals with the C_{4v} square lattice for the $(3n)^{\text{th}}$ bandgap from $n=1$ to $n=15$ for the in-plane waves.	51
5.7. Optimized phononic bandgap crystals with the C_1 square lattice for the $(3n)^{\text{th}}$ bandgap from $n=1$ to $n=15$ for the in-plane waves.	51
5.8. Relative phononic bandgap sizes with the C_1 and C_{4v} square lattice for the $(3n)^{\text{th}}$ bandgap from $n=1$ to $n=15$ for the in-plane waves.	53
5.9. Optimized square-latticed phononic bandgap crystals and their band diagrams for the complete bandgap between the second out-of-plane bandgap and third in-plane bandgap (a) with the C_{4v} symmetry; (b) with the C_1 symmetry.....	53
5.10. Optimized phononic bandgap crystals with the C_{6v} hexagonal lattice from the first bandgap to the fifteenth bandgap for the out-of-plane waves.....	55

5.11. Optimized phononic bandgap crystals with C_1 hexagonal lattice from the first bandgap to the fifteenth bandgap for the out-of-plane waves.....	55
5.12. Relative phononic bandgap sizes with C_1 and C_{6v} hexagonal lattice from the first bandgap to the fifteenth bandgap for the out-of-plane waves.....	56
5.13. Optimized phononic bandgap crystals with C_{6v} hexagonal lattice for the $(3n)^{\text{th}}$ bandgap from $n=1$ to $n=15$ for the in-plane wave mode	57
5.14. Optimized phononic bandgap crystals with C_1 hexagonal lattice for the $(3n)^{\text{th}}$ bandgap from $n=1$ to $n=15$ for the in-plane wave mode	58
5.15. Relative phononic bandgap sizes with C_1 and C_{6v} hexagonal lattice with the $(3n)^{\text{th}}$ bandgap from $n=1$ to $n=15$ for the in-plane wave mode	58
5.16. Optimized square-latticed phononic bandgap crystals and their band diagrams for the complete bandgap (a) between the first out-of-plane bandgap and the third in-plane bandgap for the C_{6v} symmetry; (b) between the second out-of-plane bandgap and the third in-plane bandgap for the C_1 symmetry.....	59
A2.1. VTs and CVTs at $n= 4$ for (a) square domain (b) hexagonal domain. Left: VTs; right: CVTs.	68
A2.2. PCVTs with C_1 symmetry at $n= 4$ for (a) square domain (b) hexagonal domain	68
A2.3. PCVTs for square unit cells with C_{4v} symmetry from $n=1$ to $n=15$	69
A2.4. PCVTs for square unit cells with C_1 symmetry from $n=1$ to $n=15$	69
A2.5. PCVTs for hexagonal unit cells with C_{6v} symmetry from $n=1$ to $n=15$	70

A2.6. PCVTs for hexagonal unit cells with C_1 symmetry from $n=1$ to $n=15$ 70

List of tables

4.1: Mechanical properties of epoxy and Au.....	31
4.2: Relative bandgap size of phononic bandgap crystals for out-of-plane waves with hexagonal lattice and square lattice.....	33
4.3: Relative bandgap size of phononic bandgap crystals for in-plane waves with hexagonal lattice and square lattice.....	36
5.1: Mechanical properties of epoxy and Pb	45

Chapter 1. Introduction

1.1 Research background

Material science focuses on the development of new and better materials for the next generation of engineering applications, which is the significant fabric of the twenty-first century. In the past decades, the in-depth research of material always brought a great revolution in science and technology and therefore improved our daily lives. For example, semiconductors have the property of being a controllable switch, which is the basis of our everyday devices such as computers, the Internet, tablet devices, and smart-phones.

Since two decades ago, many researchers have focused on the composite materials with periodic structures. In 1987, Yablonovitch [1] and John [2] proposed the concept of photonic crystals: periodic structures consisting of two and more materials with different refractive indexes forbid the propagation of electromagnetic waves at a certain range of wavelength. Then, the study of photonic crystals was spread to a wide range of new optical properties and applications.

Photonic crystals manipulate the flow of electromagnetic waves. An analog of photonic crystals is phononic crystals (PnCs) which control the propagation of the acoustic and elastic waves. The analog between the electromagnetic waves and acoustic and mechanic waves have brought up the new research field of PnCs. In 1992, Siglas and Economou [3] studied the structure of spherical inclusions suspended in a host matrix with different elastic wave speeds and detected a narrow elastic bandgap. In the next year, Kushwaha et al. [4] proposed the concept of PnCs and used plane wave expansion method to calculate the band structure of two-dimensional PnCs consisting of two metal materials: Al and Ni. Later on, the first experiment was carried out on a famous sculpture in Madrid, Spain, which proved the existence of sound attenuation in some spectral regions [5].

PnCs are composite materials formed by periodic variation of the mechanical properties of the base materials. Well-designed PnCs exhibit a salient feature called bandgap in which acoustic and mechanical waves are not allowed to travel at a certain frequency range. The property of phononic bandgap gives rise to many practical applications in designing various devices for vibration attenuation [6], waveguides [7], collimation [8] and negative refraction

[9, 10] of acoustic and elastic waves. To employ these novel applications, an adaptable approach to engineering the PnCs with large bandgaps has become an urgent need and attracted much attention in both computational mechanics and physics.

Owing to the fascinating characteristics of the acoustic and elastic bandgap, phononic bandgap engineering received a great deal of attention. The early work mainly focuses on investigating the influential factors on the phononic bandgap size. For instance, different material combinations, inclusion shapes, lattice types, filling ratios, rotation of inclusions, material properties were compared in order to increase the phononic bandgap size [11-16]. Phononic bandgaps physically originate from strong scattering and destructive interference of the multiple scattered waves. Therefore, the occurrence and width of phononic bandgaps highly depend on the spatial arrangement of base materials in the primitive unit cell. The traditional *trial-and-error* approaches may not be able to introduce new configurations of PnCs, and the resulting bandgap width may also be far from optimal one.

Since the implementation of optimization approaches on the design of phononic bandgap structure by Sigmund and Jensen [17] based on the finite element method (FEM) and the solid isotropic material with penalization (SIMP), the topology optimization of PnCs becomes a hot topic. Till now, optimization methods such as Genetic Algorithm [18-20] and BESO [21, 22] have also been developed for the design of phononic bandgap crystals. A variety of novel phononic structures with broad bandgaps have been successfully obtained by utilizing these topology optimization techniques.

1.2 Gap of knowledge

Topology optimization of phononic bandgap crystals is still at an early stage, and most of the previous studies focused on designing PnCs with the four-fold symmetric square lattice. Phononic bandgap crystals with hexagonal lattices were less considered although the previous study revealed that hexagonal-latticed phononic bandgap crystals could present wider bandgaps than those of the square-latticed phononic bandgap crystals [12, 16]. Compared with the square-latticed phononic bandgap crystals, the optimization of hexagonal-latticed phononic bandgap crystals needs to tackle the different unit cell models with the six-fold symmetry, which is more challenging to achieve the desirable bandgaps.

In the recent years, a lot of literature reveals that the symmetry reduction is an efficient way

to enhance the bandgap size in the field of photonic crystals [23-25]. Because of the analog between electromagnetic and elastic waves, many properties of PnCs are comparable to those of photonic crystals. The study of symmetries of scatterers in the phononic bandgap crystal first reveals the strong influence of symmetry on the phononic bandgap [26]. However, because of the high computational load and the complex optimization procedure, most topology optimization approaches on maximizing phononic bandgap assumed that the unit-cell has a primary high-symmetry. As a result, a systematic and comprehensive research on the bandgap design of other symmetric or asymmetrical PnCs is needed, which is the main aim of the current research.

1.3 Outline of this thesis

The structure of the rest of this thesis is outlined as follow:

Chapter 2 gives a literature review of the research fields which are highly related to the current research. The review is first dedicated to the current research status on the phononic crystal, which is followed by the introduction of several popular topology optimization methods. Then, the investigation into topology optimization of phononic bandgap crystals is reviewed at the end of the chapter.

Chapter 3 starts with the detailed implementation of the numerical analysis on the phononic bandgap crystals. It is followed by the basic theory of the BESO method, material interpolation scheme, the sensitivity calculation, element filter scheme, topology updating criteria and algorithms. This chapter ends with a summary of the topology optimization process of BESO.

Chapter 4 optimizes the two-dimensional PnCs with the six-fold symmetric hexagonal lattice for the out-of-plane, in-plane and complete wave modes, then compares their characteristics with the results with four-fold symmetric square lattice. The transmission spectra are analyzed to confirm the validity of the proposed optimization algorithm.

Chapter 5 reports the results and discussions on the optimization of the two-dimensional asymmetrical PnCs with the square lattice and the hexagonal lattice. The newly found phononic structures with large out-of-plane, in-plane, and complete bandgaps are presented. The influence of symmetry is also analyzed for both square and hexagonal lattices.

Chapter 6 gives the conclusions of this thesis and proposes the future work on the topic.

Chapter 2. Literature review

2.1 Phononic crystals

2.1.1 Concept of phononic crystals

It has been over a half-century since scientists set out to investigate the propagation behaviors of elastic waves. However, the phononic crystal is a relatively new research field since the year of 1992 when Siglas and Economou [3] proposed a structure containing spherical scatters embedded in the matrix with a narrow elastic bandgap. In 1993, Kushwaha et al. [4] proposed the concept of PnCs based on the traditional natural crystals. A crystal or crystalline solid in nature (e.g., ice, calcite) is a solid material whose constituents (e.g., atoms, molecules, and ions) are distributed in a periodically ordered microscopic structure, which forms a crystal lattice [27]. By imitating the arrangement of constituents in the natural crystals, PnCs are developed as synthetic materials with periodic variation of the mechanical properties of base materials (i.e., elastic modulus and mass density). One of the most valuable characteristics of PnCs is bandgap, within which the propagation of acoustic and elastic waves is totally prohibited.

The so-called elastic bandgap materials are inhomogeneous elastic materials consisting of one, two and three-dimensional periodic arrangement of inclusions embedded in a host matrix. One example of the one-dimensional phononic crystals is a layered comb-like structure [28, 29]. A two-dimensional phononic crystal is usually composed of parallel cylinders embedded in a host matrix [6, 30]. Three-dimensional PnCs are arrays of spherical inclusions suspended in a host matrix where waves travel in any directions of the space [31, 32]. The simple concept of one, two and three-dimensional (1D, 2D, and 3D) PnCs are illustrated in Figure 2.1.

Bandgap as one of the fascinating characteristics of PnCs has been attracting the growing interests among the academia. As a consequence, many contributions have been devoted to enriching the diversity of applications of PnCs. The following section will be dedicated to the introduction of engineering phononic bandgap and novel applications of the bandgap of PnCs.

In the search for bandgaps, various categories of phononic structures differing in the states of matter with large bandgaps have been investigated, such as solid/solid [4, 33-35], fluid/fluid

[30, 32] and fluid/solid [36-39] composite materials. Because the transverse wave can not propagate in fluids, the fluid/fluid PnCs and some fluid/solid where solid inclusions are separated by the fluid matrix are also known as the sonic crystals [40]. Besides, bandgaps in the porous [14, 41] and cellular [21] PnCs were also obtained. Compared with the composite PnCs, the porous and cellular PnCs can possibly achieve the lighter designs. In this research, we will focus on the design of solid/solid PnCs, which are able to propagate both longitudinal and transverse waves.

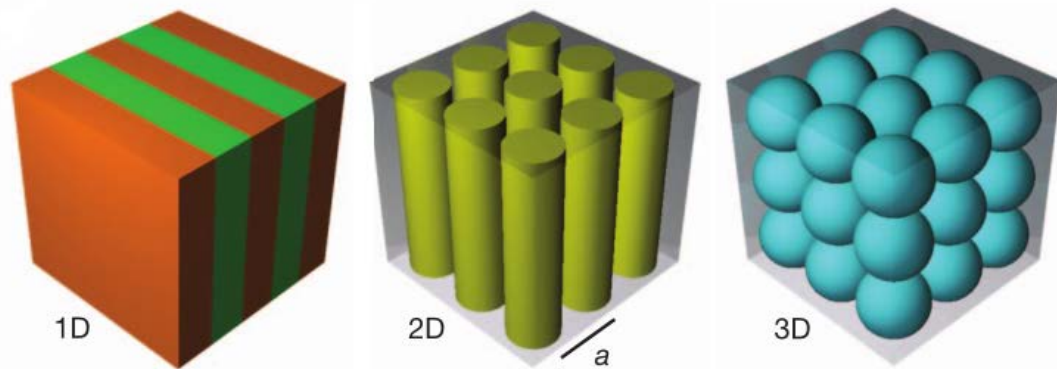


Figure 2.1. 1D, 2D and 3D PnCs made of two different elastic materials arranged periodically. Different colors represent different base materials [42].

2.1.2 Engineering bandgap of PnCs

By now, a lot of works have been carried out to establish the relationship between the scatter properties (shapes, sizes, and lattice structures), the material constants (Young's modulus, Poisson's ratios, mass density) and the phononic bandgaps. Kushwaha and Halevi [12] found the bandgap increases with a larger density-constant contrast and elastic-constant contrast of base materials in two-dimensional composite PnCs. In Kushwaha and Djafari-Rouhani's study [43] into the two-dimensional periodic arrangement of air cylinders suspended in water, several broad acoustic bandgaps were identified. In the several references [12, 32, 34], researchers discovered the effect of the filling ratio of inclusions on the bandgap size. Generally, the bandgap size appears and rises with the increase of the filling ratio before reaching its peak, followed by a gradual drop. The largest bandgap appears at a different filling ratio ranging from 20% to 60% depending on the specific combination of the base materials. The results in [30] showed that, in the liquid system of water and mercury, the configuration of scatters with low density in a matrix with high density is the most favorable for achieving board acoustic

bandgaps. Wu et al. [44] created and tuned acoustic bandgaps in two-dimensional liquid sonic crystals by rotating square rods and found that the width of the lowest gap was raised by adding the rotation angle of the square inclusions. Lai and Zhang [45] discovered that by inserting air rods in the two-dimensional system of Al inclusions in epoxy, a sizeable bandgap for elastic waves can be obtained. Lin et al. [46] studied the bandgap characteristics of scatters embedded in different anisotropic matrices. Vasseur et al. [47] discovered that the phononic structures with hollow inclusions are also able to exhibit bandgaps. The influence of different shapes and symmetries of inclusions on the 2D phononic bandgap were investigated by Kuang et al. [26]. Their research shows that among various shapes and symmetries of inclusions with different lattices, the hexagonal-latticed structure with hexagonal inclusions has the largest relative bandgap. Zhou et al. [48] analyzed the influence of material constants on bandgaps of two-dimensional solid PnCs for elastic waves and concluded that for the out-of-plane waves, the mass density ratio predominates the size of the bandgap, for the in-plane waves, the mass density ratio and the shear modulus ratio are both crucial to the bandgap generation.

Traditional PnCs are commonly infinitely extended along the three spatial directions. The elastic and acoustic waves propagate inside the periodic structure, and the waves are known as the bulk waves. PnCs for bulk waves have attracted a lot of attention; meanwhile, it is also of great importance to investigate the wave behaviors in the semi-infinite structures and structures with finite thickness. However, when a phononic crystal with a low thickness (e.g., a plate, membrane, slab) was considered, two parallel surfaces limit the elastic wave propagation. For the particular case of isotropic solids and for elastic waves polarized in the plane of incidence (a plane containing both the direction of thickness and the direction of propagation), the wave equation has to be tackled by the Lamb waves [40]. When a phononic crystal with semi-infinite boundaries is considered, the propagation of elastic waves become strongly anisotropic, a variety of combinations of transverse and longitudinal polarizations can appear, and surface modes occur at the surfaces of PnCs. As a consequence, the wave equation that satisfies boundary conditions at the surface of a semi-infinite medium has to be solved by the surface wave [40].

Owing to the finite structural dimension, surface wave PnCs and Lamb wave PnCs are favorable in the fabrication and design of bandgap based devices. Recently, surface and Lamb wave PnCs with phononic bandgaps have been investigated and reported in the references [46,

49-56]. Figure 2.2 shows the basic models of surface wave and Lamb wave PnCs.

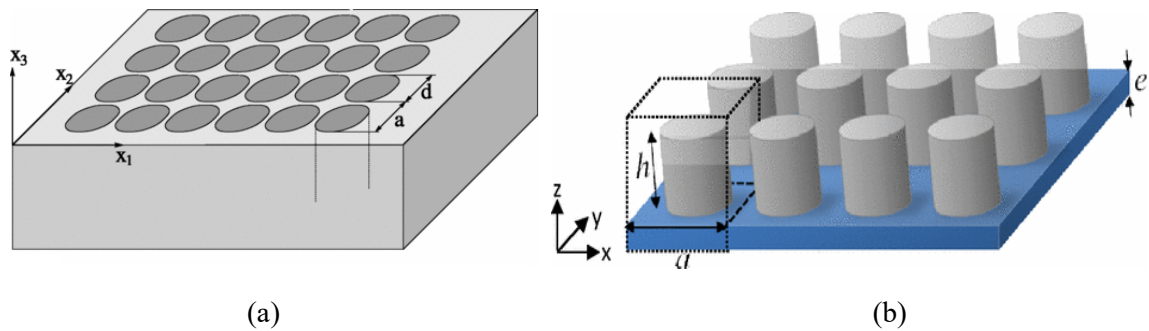


Figure 2.2. PnCs for (a) surface waves [51] and (b) plate waves [52].

The common PnCs exhibit bandgaps because the waves scattered from the inclusions interfere destructively, which is known as Bragg scattering PnCs. It is named after the phenomenon of the Bragg diffraction for X-rays in natural crystals. Similar to the Bragg diffraction for X-rays, the lattice constant of the phononic structures is generally of the same order of the wavelength of phonons. To manipulate the wave propagation in PnCs with a smaller lattice constant, Liu et al. [57] proposed an acoustic structure that uses lead balls in centimeter scale in the center of the unit cells, coated with a thin layer made of silicone rubber (Figure 2.3). Based on the locally resonant mechanism, this structure exhibits acoustic bandgaps, where the lattice constant of the structure is two orders of magnitude smaller than the acoustic wavelength. The locally resonant mechanism makes possible the sound and vibration controllable by compositions in smaller sizes [57]. Such PnCs are also termed with elastic or acoustic metamaterials.

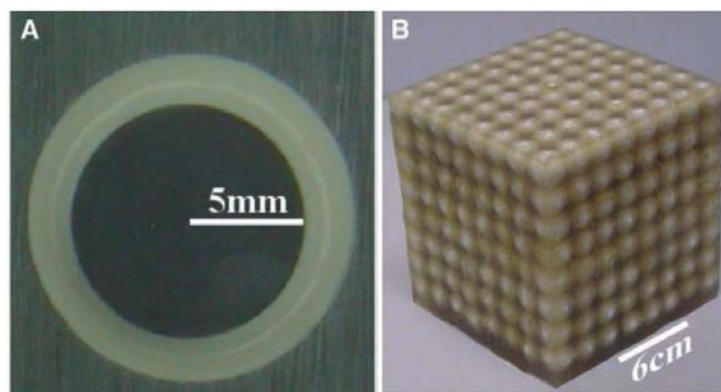


Figure 2.3. A locally resonant phononic crystal [57]

Even though a lot of outcomes in the phononic bandgap crystals engineering have been made, it is also worthwhile to investigate the bandgap generation mechanism of the PnCs because it will provide an in-depth understanding of the fundamental physics of the phononic bandgaps. In 2011, Croënne et al. [58] studied the generation mechanisms and interaction effects of phononic structure in analytical views. According to their research, there are in total three different mechanisms for phononic bandgaps: Bragg scattering, hybridization, and weak elastic coupling effects. The Bragg scattering is the most common and extensively-investigated feature. The Bragg bandgap arises because the waves scattering from the inclusions interfere destructively with each other. Hybridization gaps generate when the scattering resonances of the individual inclusions are coupled with the propagating mode of the scattering material. The bandgaps can also be observed from the weak elastic coupling effects between the individual resonances. Of all these mechanisms, Bragg scattering is the most important and typical mechanism that generates bandgaps of PnCs [59].

The investigation in calculation methods of phononic band structure is also pivotal because they provide fast, reliable and accurate tools to describe the wave propagation in particular phononic-crystalline structures. After some years' discovery and research, several different methods to has been developed such as the plane wave expansion method (PWE) [3, 4, 12, 34, 60], the finite-difference time-domain method (FDTD) [14, 61, 62], the finite element method (FEM) [20, 21, 63], the multiple scattering theory (MST) [64]. Each of these methods has been proved valid and reliable in analyzing various 2D and 3D periodic structures in the field of PnCs, and each has its pros and cons. It is important to consider three methods that are commonly linked to the topology optimization of PnCs: PWE, FDTD, and FEM.

The first application of the PWE method on the calculation of phononic dispersion relation (band structure) can be sourced from the research of Sigalas and Economou [3, 60], Kushwaha and co-workers [4, 12, 34]. Due to the periodicity of the PnCs, the PWE method uses Bloch's theory to expand elastic displacement field and the mechanical properties (e.g., mass density, Young's modulus and Poisson's ratio) of the base materials into the Fourier series. These series are then converted into the wave equations, and the terms are substituted into a typical eigenvalue problem. The wave vectors along the first Brillouin zone boundaries are involved in calculating the eigenvalues and eigenvectors. It is then straightforward to use the eigenvalues to describe the dispersion relation over the wave vectors and to use the eigenvectors to calculate

the elastic wave field distributions [6].

It is well-known that the conventional PWE method fails due to the convergence problems and converge very slow when it comes to the two-phase periodic structure with a big mismatch in material properties. To address the problem, some improved PWE methods are devised [65].

The FDTD method was initially developed to tackle the problems in electromagnetics [66, 67] before its first usage in PnCs [62]. In the FDTD method, the acoustic/elastic wave equations are first discretized with a small spatial variation and time interval. Therefore, the displacement field becomes a function of time at each discretized point and will then be updated for each time step, creating a vast amount of displacement field data which is Fourier-transformed into the frequency space. The eigenfrequencies will be obtained at the positions of peaks in the frequency spectra [59]. Due to the manipulation in the time field, the FDTD method is also able to address other problems, such as transmission and reflection in the PnCs [68], waveguiding and energy trapping in defect states of PnCs [69-71]. The FDTD method has the advantage of computing PnCs with complex topology; however, it brings substantial computational burdens due to the discretization of time and spatial domains. In 2010, Su et al. [72] developed a postprocessing method on the basis of high-resolution spectral estimation, which alleviates the difficulty of FDTD.

The FEM is a popular numerical technique serving the mechanics, physics, mathematics and many other disciplines. It is hard to confirm the earliest creation of FEM; however, in some's perspective, the history of FEM can be traced back the work in 1941 [73, 74]. It was initially aiming to solve the problems in mechanics, and after long time's development, it currently becomes a commonly used method for multiphysics problems, such as the band structure of photonic crystals [75]. Because the calculation of undamped phononic band structure is known as a natural frequency problem, the FEM has been introduced in the phononic calculation and performed well with regard to the accuracy and computational time [63].

The FEM discretizes the design domain (e.g., square unit cell) with a great number of finite elements. It is noted that the accuracy of the final solution highly depends on the size of discretizing mesh. In this way, the continuous displacement field will be represented by the interpolation of the nodal displacement with the help of the shape function. After applying the periodic boundary condition and Bloch's theory, the elastic wave equation can be converted

into the form of matrix equations. Then the eigenfrequencies and eigenvectors can be obtained by solving the matrix equations over the wave vectors over the first Brillouin zone edges.

As the FEM offers flexibility in computing complicated PnCs, it is preferable to serve for topology optimization of phononic crystals for wider bandgaps [20, 21]. In addition to calculating band structure of PnCs, it can also analyze surface acoustic waves [76, 77], point and linear defect states of phononic crystal plates [78].

Owing to the availability of the commercial FEM software in the market, the analysis and design of PnCs become much easier and more convenient. At present, COMSOL Multiphysics [17], ABAQUS [79] and ANSYS [80] have provided convenient FEM software package to analyze the wave behavior in different sorts of phononic structures.

2.1.3 Functional phononic crystals

In the recent years, the applications of PnCs have been largely extended such as vibration attenuation [6], waveguides [7], collimation [8], negative refraction [9, 10], phonon focusing [81], beam splitting [82], unidirectional propagation [83] phonon trapping [69], multiplexing of acoustic waves [84], acoustic invisibility cloaks [85, 86]. The rapid development of these novel applications is greatly owing to the prosperous development of the phononic bandgap engineering.

1). Shock and vibration proofing

Owing to the novel property of acoustic and elastic bandgaps, the PnCs are extensively investigated for its potential in sound, shock and vibration proofing especially in civil engineering [87-93].

Cheng et al. [89] found the vibration attenuation zones existing in the two-dimensional composite periodic structures consisting of concrete, steel, and rubber. Yan et al. [90] theoretically and experimentally investigated the three-dimensional periodic foundation made of concrete, rubber, and iron as a feasible seismic isolator (Figure 2.4a, b). It can be seen from Figure 2.4c that the bandgap is at a low-frequency range that covers the primary frequency range of the seismic waves owing to the locally resonant mechanism [57]. Inspired by the idea of PnCs, Wen and co-authors [88] applied the periodic binary straight beams with different

cross sections to the vibration isolation and accordingly designed a vibration isolation structure.

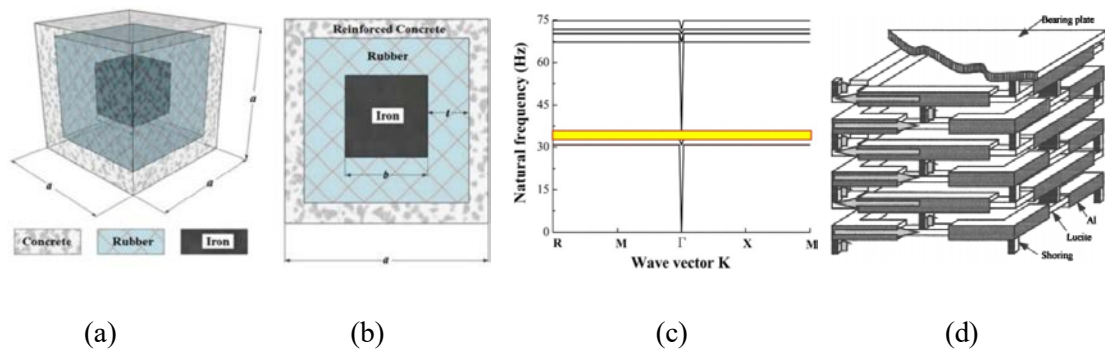


Figure 2.4. (a) One unit cell of a 3D periodic foundation; (b) the cross-section of a unit cell; (c) frequency bandgap of 3D periodic foundation [90]. (d) The sketch map of a vibration isolation structure [88].

2). Acoustic waveguide

The acoustic waveguide is based on the PnCs with defected states. The removal of the inclusions in the PnCs creates an acoustic passway for the incident wave, thus produces acoustic waveguides. Within the phononic bandgap, the acoustic waves that would not propagate otherwise in the PnCs will be guided to pass through the phononic crystal along the line-defeat passway with minimal transmission loss [68, 94, 95].

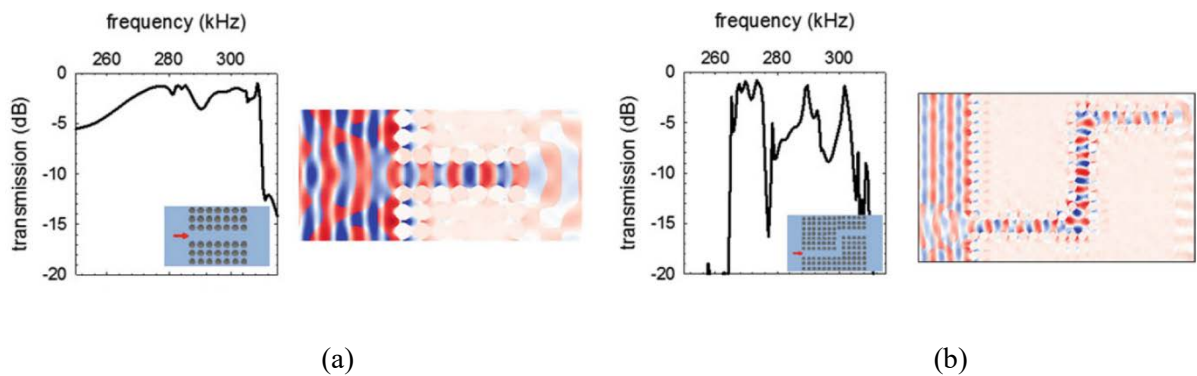


Figure 2.5. Transmission spectra in the frequency range of the bandgap and displacement fields at 290 kHz through (a) a straight and (b) a bent waveguide [7].

Khelif and co-authors [7] carried out the experiment that the acoustic waves were guided and bent in waveguides by deleting inclusions from a periodic two-dimensional phononic crystal consisting of steel rods embedded in water. Figure 2.5 indicates the waves are highly confined within the straight and bending waveguide and guided with weak losses in their research. Khelif et al. [96] created a line defect by replacing a row of solid steel cylinders in

the otherwise perfect phononic crystal with hollow cylinders and analysis the wave propagation in such a structure. Sun and Wu [70] proposed a line-defected phononic crystal consisting of circular steel cylinders in an epoxy matrix and studied the propagation of the surface acoustic waves in phononic waveguide structures using the FDTD method. Chandra et al. [97] analyzed the acoustic waves propagating along the three-dimensional waveguides in phononic structures consisting of lead spheres on a face-centered cubic lattice embedded in an epoxy matrix. In the micrometer scale, Benchabane et al. [98] reported surface wave guidance and confinement in a phononic crystal structure. Other exotic phenomena such as the coupling effect of two parallel phononic crystal waveguide were studied and discussed by Sun and Wu [99].

3). Negative refraction

Refraction is a phenomenon that often occurs when waves travel from a medium to another with different refractive indexes at an oblique angle. The refractive wave is at the different side from the incident wave to the normal in the conventional materials, which is called positive refraction; negative refraction is on the contrary of positive refraction (Figure 2.6a). The negative refraction was first predicted by Veselago in 1968 if a kind of unusual material with both permittivity and permeability simultaneously negative exists [100]. This phenomenon was realized several decades later in the optical [101] and then acoustic [81, 102] regions. Sukhovich and co-authors [102] presented an experimental illustration of negative refraction and focusing of ultrasonic waves in 2D PnCs composed of steel cylinders arranged in the hexagonal lattice and embedded in methanol (Figure 2.6b, c). Li and Chan [103] reported a double-negative acoustic system with both negative density and modulus.

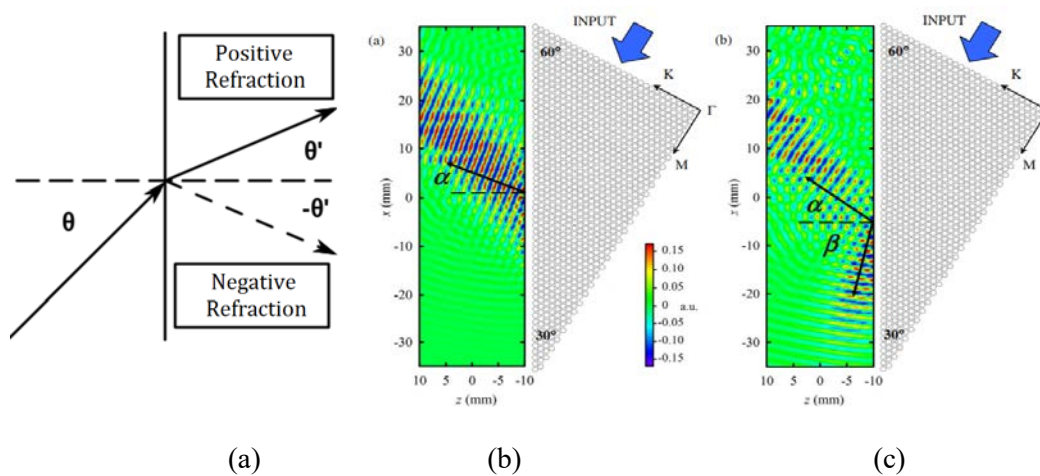


Figure 2.6. (a) Schematic diagram of the positive and negative refraction. Two snapshots of the outgoing pulses in the negative refraction experiment, obtained by digitally filtering original pulses at

the frequency of (b) 0.85 MHz and (c) 0.75 MHz [102].

4). Acoustic diodes and unidirectional acoustic transmission

A diode in the electronic region is a device that allows electrical current to flow unidirectionally. This creation led to an electronic revolution that revealed the age of information [104]. Today, with the emergence of phononic bandgap crystals, scientists have discovered the acoustic counterpart of the electronic diode.

Liang et al. [83, 105] proposed a model of an acoustic diode and illustrated the wave behavior of the unidirectional acoustic transmission by combining layers of water and glass with a nonlinear acoustic material as shown in Figure 2.7. The nonlinear acoustic medium partially converts the incident wave at the frequency of ω to a secondary wave at the frequency 2ω . The superlattice made from water and glass forms a bandgap to prevent the propagation of secondary wave but allows the original wave at the frequency of ω . Nonlinear medium converts the incident wave from the left side into the secondary wave, which can freely pass the structure, while incident wave from the right is complete reflected backward by the superlattice. Boechler et al. [106] found defected state of PnCs can also convert vibrations at the selected frequencies to a different frequency by creating a localized mode, thus realize sound rectification.

Other researchers focused on the linear material without the frequency conversion [107-113]. Li et al. [107] designed acoustic diode based on the asymmetrical sonic crystals and experimentally analyzed the unidirectional acoustic transmission in the structure in Figure 2.7b. An inverted bi-prism phononic crystal (Figure 2.7c) realizing one-sided elastic wave transmission was designed [108]. The proposal of another model that realizes the unidirectional acoustic transmission by making the use of the partial band (distinction of the bandgap of PnCs between two directions) was also reported in [109]. The incident wave from the right lies in the bandgap and thus reverses while waves arisen from the left (45° direction) reside outside the bandgap pass the PnCs as shown in Figure 2.7d [109].

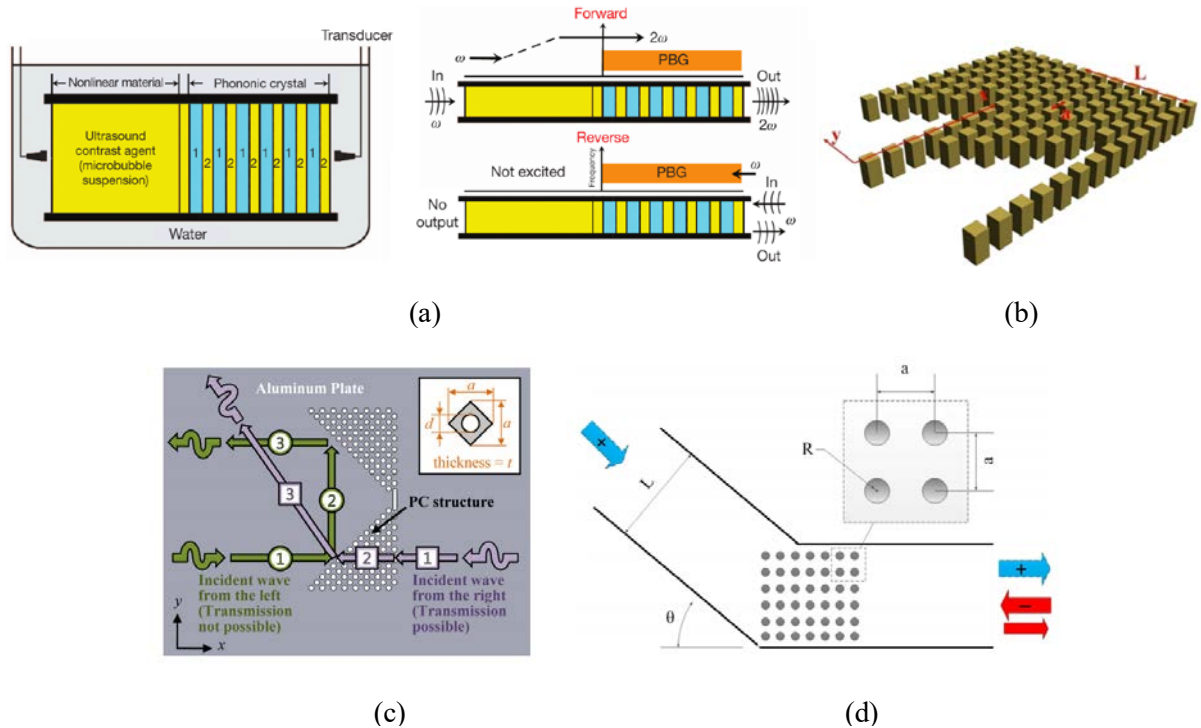


Figure 2.7. (a) An acoustic diode made of a 1D phononic crystal (alternating layers of glass and water) coupled to a nonlinear acoustic medium [83]. (b) A sonic crystal-based acoustic diode [107]. (c) An inverted bi-prism[108]. (d) Schematic model of the directional waveguide [109].

2.2 Topology optimization

Size, shape and topology optimization are three types of structure optimization. In sizing optimization, the model was optimized by changing certain size variables including the cross-sectional areas of beams or frames, and the thicknesses of slabs. This is the original and the simplest method to enhancing the mechanical performance of a structure. By changing the predetermined boundaries of the continuum structures, shape optimization is able to achieve the optimal designs. Compared with the size and shape optimization which updates the size variables and shape boundaries, topology optimization focuses on finding the optimal spatial order and connectivity for the discrete structure and the best location and geometries of cavities for the continuum structure [114]. Topology optimization brings with more effectiveness as well as challenges because it can generate the optimal topology without pre-designed topology automatically.

Topology optimization originates from the investigation of the least-weight truss layout problem by versatile Australian engineer Michell [115]. Since the landmark work published by Bendsøe and Kikuchi in 1988 [116], a significant number of researchers have been devoted to

developing the theory and applications of topology optimization, and it now becomes a well-established technique.

By now, topology optimization has been extensively used in scientific and engineering design. There are a large number of different practical topology optimization approaches that can be categorized into two groups with respect to the involvement of gradient. The gradient-based group includes the homogenization approach [117], the solid isotropic material with penalization (SIMP) [118], the bi-directional evolutionary structural optimization (BESO) [114], level-set approach [119], while the non-gradient-based approaches comprise the early versions of evolutionary structural optimization (ESO) [120, 121] and bi-directional ESO (BESO) [122], the genetic algorithm (GA) [123], ant colonies method [124] and so on.

2.2.1 Genetic algorithm

The GA method is one of the most popular non-gradient-based optimization methods. It was biologically inspired by Darwin's survival of the fittest principle of the natural selection. The genetic algorithm (GA) method was established by John Holland in the 1960s and has been greatly developed since then. At present, the GA method has evolved into an extensively used random search optimization approach solving the problems in all walks of life [125].

The terminology in the GA method includes population, chromosome, gene, crossover, mutation, fitness, and others. A population contains a number of chromosomes that are also called individuals. A chromosome is a binary integer and consists of a certain amount of genes, which represent all of the design variables. For instance, in the topology optimization of phononic bandgap crystals combining the GA method with FEM, a gene can describe the material of a discretized element [20]. The fitness of a chromosome is the evaluation of the objective based on the topology translated from the genes contained in the chromosome. The genes that are usually chosen from two parent chromosomes will be hybridized by combining their genetic materials to make up new chromosomes, which is known as crossover. Mutation is a random modification of one and more genes in the chromosomes. In each iteration, enough chromosomes will be obtained to join the next iteration.

Unlike the gradient-based optimization approaches, the GA method has a different set of the optimization procedure. It does not require material interpolation scheme and sensitivity

calculation, which makes the process more straightforward and accessible. At first, a random population will be generated to start with. The objective function (e.g., bandgap width) of each (chromosome) will be calculated to obtain the fitness in every iteration step. According to the fitness, the chromosomes in the population are selected to provide their genes for the iteration. In the population of the next generation, new chromosomes are achieved by crossover, mutation and direct inheritance from old chromosomes. The procedure will be terminated with chromosomes having optimal and stable average fitness after sufficient iterations [126].

2.2.2 Solid isotropic material with penalization

Bendsøe proposed the original idea of SIMP method in the year of 1989 [127], and it was improved in mathematical theory and was extended to a wide range of applications by Sigmund and others [128].

The SIMP method is based on the FEM where the design domain is discretized into a number of finite elements. Under the circumstance, every element is represented by a design variable ranged continuously from 0 or a minimal value (void) to 1 (solid). The design variables valued between 0 and 1 are called intermediate material. To achieve nearly 0/1 design and avoid intermediate material, a penalization scheme was introduced by adding a penalty power to the material properties (e.g., Young's modulus in the minimization of compliance problem) of the intermediate materials. The value of penalty power should be larger than 1 and normally 3. Based on FEM, the sensitivity of objective and constraint functions with regard to design variables can be calculated and used to update the design variables. In some cases, a filtering scheme which averages the sensitivity over the neighboring elements was introduced to solve the checkerboard and mesh-dependent problems. The procedure will continue until the particular convergence criteria are met [118].

2.2.3 Evolutionary structural optimization/Bi-directional evolutionary structural optimization

The ESO method was first created by Xie and Steven in 1992 [120]. Since then it has been widely used in a variety of topology optimization problems [121]. Its simple concept lies in the evolvement towards the optimal topology by gradual removing of inefficient material from a structure. Later on, the bi-directional ESO (BESO) [122] was established by Querin et al.,

which extends the idea of ESO from merely deleting material to allowing the material to be gradually added and deleted simultaneously. Generally, the BESO algorithm starts from a nearly full design and random initial design in the design domain. Based on FEM, the design domain is discretized and represented by 0/1 design variables indicating void/solid elements. The element will be ranked according to some criteria (sensitivity numbers, von Mises stress, and others). Then, a threshold is determined by the target volume fraction in each iteration. The material will be added to the elements above the threshold and removed in the elements below the threshold. In each iteration step, the volume fraction of the solid material changes by a small amount. The above steps will repeat until the prescribed volume constraint is achieved.

To be noted, the early-stage ESO and BESO are greatly based on a heuristic concept and lack theoretical rigors. Particularly, the optimal design was selected by comparison out of a very great amount of intuitively generated results [121, 129].

Huang and Xie [114, 130] developed a new BESO method to avoid the deficiencies of the previous ESO/BESO method. The filter scheme of the sensitivity number was adopted to avoid the checkerboard and the mesh-dependent problems [131]. In the complete 0/1 design, the sensitivity number of the void elements can not be derived directly from a mathematical way. Rozvany and Querin advised a sequential element rejection and admission (SERA) method where the void elements are substituted by ‘virtual’ elements with very low Young’s modulus [132]. Finally, in the setting of discrete design variable without the intermediate variable, the optimization may suffer from oscillation in the evolution process and difficulty of convergence. To address the problem, two efficient measures were proposed. One is to add the intermediate discrete values between 0/1 value to stabilize the optimization process [133]; another is to calculate the average of the sensitivity number with its history information [130].

2.3 Topology optimization of phononic bandgap crystals

In the design of phononic crystal-based devices, PnCs with wider bandgaps mean the better performance of the devices. It is well known that bandgaps physically originate from strong scattering and destructive interference of the multiple scattered waves. Therefore, the occurrence and width of phononic bandgaps highly rely on the spatial arrangement of base materials within the primitive unit cell. The early work mainly focuses on the influential factors on the phononic bandgap size which may not be able to introduce new configurations of PnCs, and the resulting bandgap width may also be far from optimal one. As a result, topology

optimization approached are of great significance to search for the largest bandgaps as well as the expectant features of the phononic crystal-based structures.

Topology optimization was firstly introduced in the design of 2D phononic bandgap crystals with the square lattice by Sigmund and Jensen [17] based on FEM and SIMP. However, the approach encountered the difficulty of opening bandgaps, and therefore the optimization just enlarged the existing bandgaps. Thereafter, many solid-solid, porous and cellular bandgap PnCs are designed by topology optimization. In the field of solid-solid phononic bandgap crystals, Hussein et al. [134] carried out an optimization work of one-dimensional periodic unit cells for longitudinal waves in the target frequency based on GAs. Gazonas et al. [18] combined GAs with FEM to search for the optimal phononic structures by maximizing the acoustic bandgap. In 2007, Hussein et al. [135] linked GA with FEM to design 2D PnCs with multiple bandgaps and conducted the optimization for a range of material constants (i.e., Young's modulus ratio and density ratio). Dong et al. [20] used a two-stage GA and FEM to perform the bandgap optimization of the 2D PnCs with and without filling ratio constraint of the inclusions. In their research, many new structures were obtained with relatively wide bandgaps. Based on a multiple elitist GA with the adaptive fuzzy fitness granulation, two-dimensional asymmetrical PnCs are designed by Dong et al. [136].

In many of the above research, the optimization process is very time-consuming because in GA's search for the optimal solutions, each iteration requires the calculation of a population of chromosomes, which exerts heavy computational burdens. Toward a fast, efficient and easy-implement optimization for phononoc bandgap structures, Li et al. [21] applied the BESO method in conjunction with FEM to the phononic bandgap optimization. Chen et al. [137] proposed an approach to design PnCs for maximizing spatial decay of evanescent waves based on BESO.

In the field of two-dimensional porous and cellular bandgap crystals, Bilal and Hussein [138] proposed a specialized GA in combination with the reduced Bloch mode expansion method for the design of silicon and void PnCs with wide bandgaps. Dong et al. [139] presented a study on the multi-objective optimization of porous PnCs in both square and hexagonal lattices with the reduced symmetry by using a fast non-dominated sorting-based GA II. Li et al. [21] used BESO and FEM on topology optimization of cellular PnCs to enlarge the relative elastic bandgaps with a bulk or shear modulus constraint. A record-breaking result of the relative

bandgap at 144.41% was obtained for the out-of-plane wave mode in their research.

In conclusion, the topology optimization of phononic bandgap crystals is still on its early stage, and a lot of work still needs to be done. For example, to the authors' best knowledge, there is no topological design conducted on the two-dimensional solid-solid phononic bandgap crystals with six-fold symmetric hexagonal lattice. Additionally, although the symmetry reduction has been investigated by Dong et al. [136], the results provided in their research are relatively few to conduct a comprehensive analysis of the effects of symmetry on the bandgap size. The further research on the topological design of phononic bandgap crystals is full of opportunities as well as challenges, which forms the main objectives of the current research.

Chapter 3. Numerical analysis and topology optimization for phononic crystals

This chapter investigates the numerical analysis and topology optimization of two-dimensional (2D) solid PnCs. Section 3.1 describes the numerical analysis of the phononic crystals. The implementation of BESO is introduced in Section 3.2.

3.1 Numerical analysis

In the Cartesian coordinate system, the stress tensor is shown below

$$\boldsymbol{\sigma} = \begin{bmatrix} \sigma_{xx} & \sigma_{xy} & \sigma_{xz} \\ \sigma_{yx} & \sigma_{yy} & \sigma_{yz} \\ \sigma_{zx} & \sigma_{zy} & \sigma_{zz} \end{bmatrix}$$

Note that the shear components $\sigma_{ij} = \sigma_{ji}, i, j = x, y, z$.

In the free vibration system, the relationship of the stress and displacement can be expressed by

$$\sigma_{ij,j} = \rho \ddot{u}_i \quad (3.1)$$

The strain is defined for small deformation with

$$\begin{cases} \varepsilon_x = \partial u / \partial x, \gamma_{yz} = \partial w / \partial y + \partial v / \partial z \\ \varepsilon_y = \partial v / \partial y, \gamma_{xz} = \partial u / \partial z + \partial w / \partial x \\ \varepsilon_z = \partial w / \partial z, \gamma_{xy} = \partial v / \partial x + \partial u / \partial y \end{cases}$$

where u, v, w are the displacements along x, y, z directions. The above equations can be written in the Einstein notation as follows.

$$e_{ij} = 1/2(u_{i,j} + u_{j,i}) \quad (3.2)$$

where $e_{ij} = \begin{cases} \varepsilon_x, i = j \\ \gamma_{ij}, i \neq j \end{cases}$

In the isotropic materials, the linear relationship between stress and strain depends on two independent Lamé's constants,

$$\begin{cases} \sigma_{xx} = \lambda\theta + 2\mu\varepsilon_x, \sigma_{yz} = \mu\gamma_{yz} \\ \sigma_{yy} = \lambda\theta + 2\mu\varepsilon_y, \sigma_{xz} = \mu\gamma_{xz} \\ \sigma_{zz} = \lambda\theta + 2\mu\varepsilon_z, \sigma_{xy} = \mu\gamma_{xy} \\ \theta = \varepsilon_x + \varepsilon_y + \varepsilon_z \end{cases}$$

The above equations can be rewritten in the Einstein notation as follows.

$$\sigma_{ij} = \lambda\theta\delta_{ij} + 2\mu e_{ij} \quad (3.3)$$

where the Kronecker delta $\delta_{ij} = \begin{cases} 1, i = j \\ 0, i \neq j \end{cases}$.

From equation (3.1-3.3), the propagation of elastic waves in PnCs is governed by

$$\rho \frac{\partial^2 \mathbf{u}_i}{\partial t^2} = \sum_{j=1}^3 \left\{ \frac{\partial}{\partial x_i} \left(\lambda \frac{\partial u_j}{\partial x_j} \right) + \frac{\partial}{\partial x_j} \left[\mu \left(\frac{\partial u_j}{\partial x_i} + \frac{\partial u_i}{\partial x_j} \right) \right] \right\} \quad (3.4)$$

where λ and μ are the Lamé's coefficients; ρ is the material density.

In this thesis, only 2D PnCs are considered. As the wave field is independent of z , equation (3.4) can be divided into two sets of equations governing the out-of-plane mode (u_z) and the mixed in-plane mode (u_x and u_y), respectively,

$$-\rho(\mathbf{r})\omega^2 u_x = \frac{\partial}{\partial x} \left[(\lambda + 2\mu) \frac{\partial u_x}{\partial x} + \lambda \frac{\partial u_y}{\partial y} \right] + \frac{\partial}{\partial y} \left[\mu \left(\frac{\partial u_x}{\partial y} + \frac{\partial u_y}{\partial x} \right) \right] \quad (3.5)$$

$$-\rho(\mathbf{r})\omega^2 u_y = \frac{\partial}{\partial y} \left[(\lambda + 2\mu) \frac{\partial u_y}{\partial y} + \lambda \frac{\partial u_x}{\partial x} \right] + \frac{\partial}{\partial x} \left[\mu \left(\frac{\partial u_y}{\partial x} + \frac{\partial u_x}{\partial y} \right) \right] \quad (3.6)$$

$$-\rho(\mathbf{r})\omega^2 u_z = \frac{\partial}{\partial y} \left[\mu \left(\frac{\partial u_z}{\partial y} \right) \right] + \frac{\partial}{\partial x} \left[\mu \left(\frac{\partial u_z}{\partial x} \right) \right] \quad (3.7)$$

where $\mathbf{r}(x, y)$ is the position vector.

According to the Bloch theory [140], the displacement vector can be expressed as

$$\mathbf{u}(\mathbf{r}, \mathbf{k}) = \mathbf{u}_{\mathbf{k}}(\mathbf{r}) e^{i(\mathbf{k} \cdot \mathbf{r})} \quad (3.8)$$

where $\mathbf{u}_{\mathbf{k}}(\mathbf{r})$ is a periodic function of \mathbf{r} with the same periodicity as the structure. $\mathbf{k} = (k_x, k_y)$ is the Bloch wave vector. To this end, the governing equation can be converted to a typical eigenvalue equation under the framework of the FEM [40]

$$(\mathbf{K}(\mathbf{k}) - \omega^2 \mathbf{M})\mathbf{u} = 0 \quad (3.9)$$

where \mathbf{K} and \mathbf{M} are the stiffness matrix and the mass matrix which are assembled from the elemental stiffness matrixes and elemental mass matrixes that are elaborated in Appendix 1.

The above equation is solved by sweeping wave vectors \mathbf{k} along the boundary of the first irreducible Brillouin zone, which depends on the lattice type and symmetry. Here, a simple example of a symmetric hexagonal-latticed phononic crystal is shown in Figure 3.1a and its first irreducible Brillouin zone ($\Gamma \rightarrow X \rightarrow M \rightarrow \Gamma$) as shown in Figure 3.1c. The relationship between eigenfrequency ω and \mathbf{k} forms its band diagram for the Au/epoxy system as shown in Figure 3.1d. The band diagram indicates that the complete bandgap (grey area) between the third in-plane band and the second out-of-plane band is achieved. Even so, it is still unclear if the bandgap can be further enlarged and the bandgap at other specified bands can be found. These questions will be addressed by the developed topology optimization algorithm in the next section.

Generally, the size of the bandgap between the n^{th} and $(n+1)^{\text{th}}$ band can be reasonably measured by the gapsize-midgap ratio. As discussed above, the elastic waves can be decoupled into the in-plane waves and out-of-plane waves for 2D PnCs. For the bandgaps for the in-plane waves and out-of-plane waves only, the relative bandgap between n^{th} and $(n+1)^{\text{th}}$ band is defined by

$$GAP_n = \frac{\Delta\omega_n}{\omega_n^c} = 2 \frac{\min(\omega_{n+1}(\mathbf{k})) - \max(\omega_n(\mathbf{k}))}{\min(\omega_{n+1}(\mathbf{k})) + \max(\omega_n(\mathbf{k}))} \quad (3.10)$$

For the complete bandgaps, the relative bandgap between the n^{th} and $(n+1)^{\text{th}}$ band for the out-of-plane waves and at the same time, between the m^{th} and $(m+1)^{\text{th}}$ band for in-plane waves can be measured by

$$GAP_n = \frac{\Delta\omega_{nm}}{\omega_{nm}^c} = 2 \frac{\min(\omega_{n+1}^{out}(\mathbf{k}), \omega_{m+1}^{in}(\mathbf{k})) - \max(\omega_n^{out}(\mathbf{k}), \omega_m^{in}(\mathbf{k}))}{\min(\omega_{n+1}^{out}(\mathbf{k}), \omega_{m+1}^{in}(\mathbf{k})) + \max(\omega_n^{out}(\mathbf{k}), \omega_m^{in}(\mathbf{k}))} \quad (3.11)$$

where ω_n^c and ω_{nm}^c are the midgap, $\omega_n^c = \frac{1}{2}(\min(\omega_{n+1}(\mathbf{k})) + \max(\omega_n(\mathbf{k})))$ for single modes and $\omega_{nm}^c = \frac{1}{2}(\min(\omega_{n+1}^{out}(\mathbf{k}), \omega_{m+1}^{in}(\mathbf{k})) + \max(\omega_n^{out}(\mathbf{k}), \omega_m^{in}(\mathbf{k})))$ for combined wave modes. $\Delta\omega$ is the absolute bandgap size. When $GAP_n \leq 0$, it means that the bandgap does not exist.

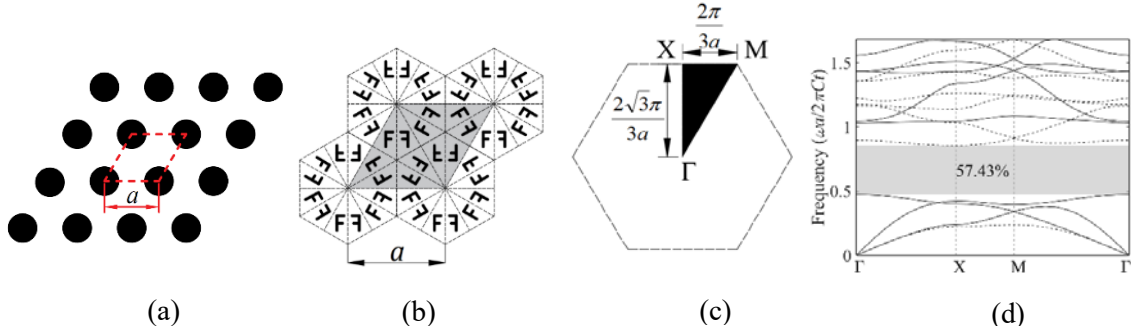


Figure 3.1. (a) A typical 2D phonic bandgap crystal with the hexagonal lattice constant a , and the dashed red rhombus denotes its primitive unit cell. (b) Six-fold symmetry of the unit cell. (c) Irreducible Brillouin zone of the hexagonal lattice (Γ -X-M- Γ). (d) The band diagram of the phonic bandgap crystal. The dashed and solid lines denote the out-of-plane and in-plane phononic bands, respectively.

3.2 Topology optimization

3.2.1 Objective function

Topology optimization aims to find an optimal material distribution of the primitive unit cell with the maximum bandgap between two adjoined bands. The primitive unit cell is discretized with finite elements and each element is assigned with an artificial design variable,

x_i ($i = 1, 2, \dots, n$), where $0 \leq x_i \leq 1$. $x_i = 0$ denotes that element i is composed of material 1, epoxy, and $x_i = 1$ denotes element i is composed of material 2, Au or Pb. The optimization objective is to maximize the n th bandgap as

$$\text{Max} : f(\mathbf{X}) = \text{GAP}_n, \quad \mathbf{X} = \{x_1, x_2, \dots, x_n\} \quad (3.11)$$

Thus, the optimization goal is to seek the optimal combination of design variables, \mathbf{X} .

3.2.2 Material interpolation scheme

To establish the relationship between design variables and material properties, the following material interpolation scheme can be assumed.

$$\rho(x_i) = (1 - x_i)\rho_1 + x_i\rho_2 \quad (3.12a)$$

$$\lambda(x_i) = (1 - x_i)\lambda_1 + x_i\lambda_2 \quad (3.12b)$$

$$\mu(x_i) = (1 - x_i)\mu_1 + x_i\mu_2 \quad (3.12c)$$

where subscripts 1 and 2 denote material 1 and 2, respectively. In the most BESO examples, the intermediate material should be penalized to obtain 0/1 design in the final solution. Whereas in the design of PnCs, the massive difference in material constants between the matrix and scatters leads to broader bandgap. In this course, the topology will automatically evolve to the full or near 0/1 design without the usage of the penalty factor.

3.2.3 Sensitivity analysis

The current BESO method [114, 141] is a gradient-based optimization algorithm and gradually updates the topology of the primitive unit cell based on sensitivity analysis. The elemental sensitivity is characterized by the derivative of the proposed objective function with respect to the variation of design variable x_i and given by

$$\alpha_i = \frac{\partial(GAP_n)}{\partial \omega(\mathbf{k})} \frac{\partial \omega(\mathbf{k})}{\partial x_i} \quad (3.13)$$

where

$$\frac{\partial \omega(\mathbf{k})}{\partial x_i} = \frac{1}{2\omega(\mathbf{k})} \mathbf{u}^T \left(\frac{\partial \mathbf{K}}{\partial x_i} - \omega^2(\mathbf{k}) \frac{\partial \mathbf{M}}{\partial x_i} \right) \mathbf{u} \quad (3.14)$$

where $\frac{\partial \mathbf{K}}{\partial x_i}$ and $\frac{\partial \mathbf{M}}{\partial x_i}$ are calculated depending on the wave modes according to equations (A1.5-A1.8) in Appendix 1. After that, the elemental sensitivity numbers are needed to be averaged with neighboring elements according to the filter scheme and with their historical information so as to stabilize the evolutionary process.

3.2.4 Sensitivity filter scheme

The filter scheme smooths the elemental sensitivity numbers according to those of their neighboring elements. The filter has a length scale r_{\min} which identifies the adjacent elements that affect the smoothed sensitivity of the i th element. This is illustrated by drawing a circle of radius r_{\min} with the center at the centroid of the i th element as shown in Figure 3.2. Usually, the value of r_{\min} should be larger than one so that Ω_i includes more than only the i th element. The smoothed elemental sensitivity number of the i th element α_i^s is obtained by

$$\alpha_i^s = \frac{\sum_{j=1}^K w(r_{ij}) \alpha_j}{\sum_{j=1}^K w_i(r_{ij})} \quad (3.15)$$

where K is the total number of elements whose centers are located in the sub-domain Ω_i , $w(r_{ij})$ is the weight factor defined as

$$w(r_{ij}) = r_{\min} - r_{ij} \quad (j = 1, 2, \dots, K) \quad (3.16)$$

where r_{ij} is the distance between the center of the i th element and the center of the j th element.

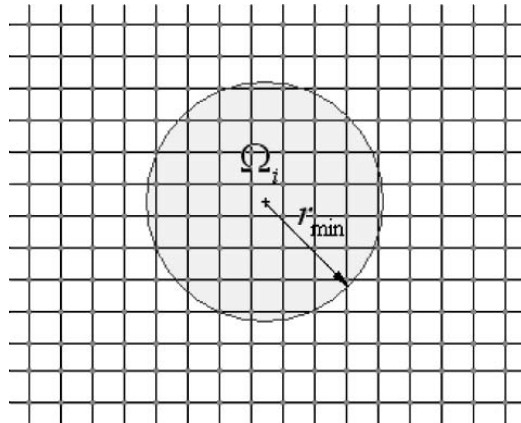


Figure 3.2. Schematic illustration of the filter scheme[114].

3.2.5 Average sensitivity numbers with history

In the BESO methods, large fluctuations can often appear in the evolutionary process of the objective function. This is because the sensitivity numbers of the elements are based on discrete design variables. For this reason, the objective function can be difficult to converge. A simple averaging scheme is established to avoid this problem [114].

$$\alpha_i = \frac{\alpha_i^k + \alpha_i^{k-1}}{2} \quad (3.17)$$

where superscript k is the current iteration number. The updated sensitivity number to be used in the later topology update will include the whole history of the sensitivity information in the previous iterations. It is noted that the averaging scheme increases the stability of the evolutionary process but has little influence on the final solution.

3.2.6 Update of topology

To update the design topology iteratively, BESO increases the design variables for elements with high sensitivities and decreases design variables for elements with low sensitivity numbers simultaneously as

$$x_i^{k+1} = \begin{cases} \min(x_i^k + \Delta x, 1) & \text{when } \alpha_i > \alpha_{th} \\ \max(x_i^k - \Delta x, 0) & \text{when } \alpha_i < \alpha_{th} \end{cases} \quad (3.18)$$

where $\Delta x = 0.1$ denotes the variation of design variables in each iteration. α_{th} is the threshold of sensitivity numbers, which is determined by the volume fraction of constituent materials. As a result, new design variables, \mathbf{X} , are found and formed a new topology.

3.2.7 BESO procedure

To summarise, the evolutionary procedure of the present BESO method in maximizing bandgap size follows these five steps:

1. Discretize the design domain with a large number of finite elements and generate the initial guess design.
2. Conduct finite element analysis and calculate the element sensitivity number using equation (3.13) and (3.14).
3. Filter the sensitivity number with adjacent elements using equation (3.15) and average the sensitivity with its historical information according to equation (3.17).
4. Update topology in the unit cell according to equation (3.18).
5. Repeat steps 2-4 until the convergence criteria are achieved.

Such an iterative process evolves the material distribution in the primitive unit cell towards its optimum. The detailed implementation of BESO refers to the flowchart in Figure 3.3 and the reference [114].

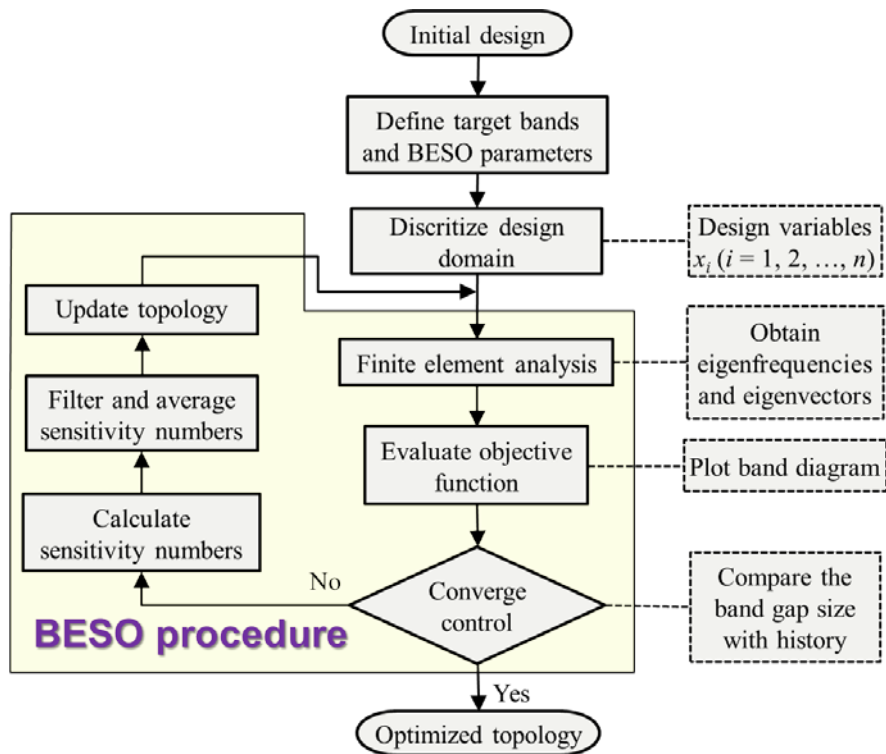


Figure 3.3. Flowchart of the proposed BESO method

Chapter 4. Topology optimization for 2D phononic bandgap crystals with six-fold symmetric hexagonal lattice

4.1 Introduction

Since the bandgaps have been detected in the photonic and phononic structures in the electromagnetics and acoustics, the search of the broad bandgaps never stops. The research in the photonics is years ahead of that of phononics. Because of the analog between electromagnetic and elastic waves, many properties of PnCs are comparable to those of photonic crystals. In the field of photonic bandgap engineering, the hexagonal lattice has been investigated by Sigmund and Hougaard [142]. Their designs with large bandgaps are of great importance to provide meaningful guidance for the later research. In [142], the optimal photonic bandgap structure at the band order increasingly from one to fifteen are presented. Among them, the biggest bandgap appears at the first band in the structure with the hexagonal lattice. Some other studies also confirmed the photonic crystals with the hexagonal lattice tends to have larger photonic gaps than those with the square lattice [23, 143].

In the field of phononic bandgap engineering, some previous studies revealed that hexagonal-latticed phononic bandgap crystals could present wider bandgaps than square-latticed ones for some simple topologies [12, 16]. In 2015, Dong et al. [139] conducted the topology optimization on porous PnCs, where many hexagonal-latticed patterns were achieved with very large bandgaps.

Based on the above research, one may expect that the structures with hexagonal lattice may exhibit wider bandgaps. However, the optimization of the two-dimensional PnCs towards bigger bandgaps mainly concentrated on the systems with the four-fold symmetric square lattice. Compared with square-latticed phononic bandgap crystals, the optimization of hexagonal-latticed phononic bandgap crystals needs to tackle with different unit cell models with 6-fold symmetry, which is more challenging to achieve the desirable bandgaps.

This chapter investigates topology optimization of two-dimensional solid hexagonal-latticed PnCs for maximizing desirable bandgaps. The materials considered in this study are Au and epoxy, same as in [22] to compare the influence of lattice on bandgap size. The optimization algorithm based on the BESO method is successfully established, and various novel patterns

with extremely large bandgaps for the out-of-plane, in-plane and combined (both in-plane and out-of-plane) waves are obtained. The results demonstrate that the bandgaps of hexagonal-latticed phononic bandgap crystals are relatively larger compared with those of square-latticed ones. The transmission analysis of the finite phononic structures formed by the optimized PnCs shows that the out-of-plane waves and in-plane waves can be transmitted and prohibited, which agrees well with the optimization results.

The rest of this chapter is organized as follows: section 4.2 states the hexagonal lattice and the six-fold symmetry. Detailed optimization results and discussions for the out-of-plane, in-plane and combined wave modes are presented in section 4.3. This is followed by conclusions in section 4.4.

4.2 Hexagonal lattice and six-fold symmetry

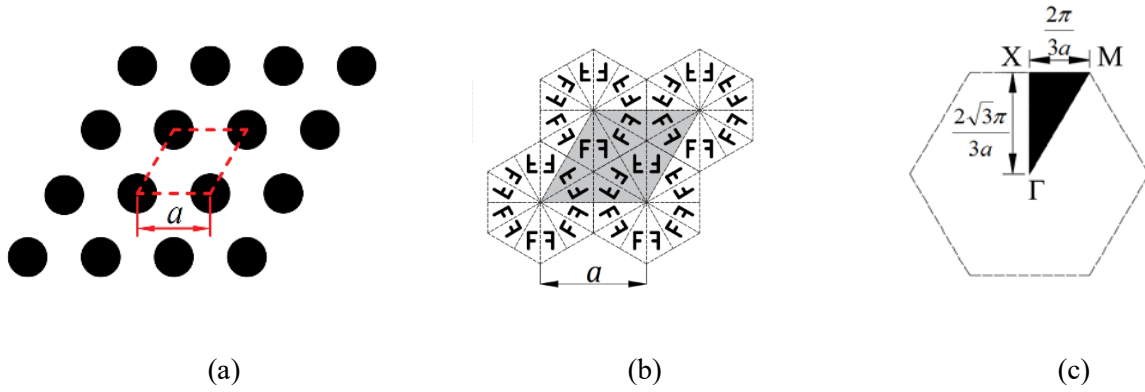


Figure 4.1. (a) A typical 2D phononic bandgap crystal with the hexagonal lattice constant a , and the dashed red rhombus denotes its primitive unit cell. (b) Six-fold symmetry of the unit cell. (c) Irreducible Brillouin zone of the hexagonal lattice (Γ -X-M- Γ).

Different from the 2D PnCs with 4-fold reflection symmetry and 4-fold rotational symmetry; the hexagonal lattice has 6-fold reflection symmetry and 6-fold rotational symmetry. Figure 4.1a shows an example of hexagonal-latticed PnCs and Figure 4.1b demonstrates the six-fold symmetry of the hexagonal lattice. A unit cell with the hexagonal lattice can be either a hexagon or a rhombus. The rhombus unit cell is employed in this research because it is easier to be meshed with four-node elements in FEM. The rhombus unit cell is represented by red rhombic dash line with the side of length a in Figure 4.1a and the gray area in Figure 4.1b. The unit cell is divided into 12 similar triangles because of the symmetry in Figure 4.1b. Figure 4.1c shows the first Brillouin zone for the hexagonal lattice, in which the black triangle represents the irreducible Brillouin zone that constitutes 1/12 of the first Brillouin zone. Due to the

relationship between the hexagonal lattice and its reciprocal lattice, the side length of Γ -X is equal to $2\sqrt{3}\pi/3a$ and X-M, $2\pi/3a$.

4.3 Optimization results and discussion

Based on the established BESO algorithm in the last chapter, this section will present numerical optimization results of hexagonal-latticed two-component solid phononic bandgap crystals for the out-of-plane, in-plane, and combined waves. In the following numerical examples, all solutions were obtained with less than 100 iterations. Compared with the Genetic Algorithm with hundreds, even thousands of iterations, the proposed gradient-based BESO method is much more efficient and allows a finer mesh to represent the clear boundary of the optimized design. The primitive unit cell is discretized with a 64×64 grid mesh, which is fine enough to depict its topology and has a good accuracy for the calculation of band diagram. It is also assumed that the phononic bandgap crystals are formed by epoxy and Au and the volume fraction of Au is restricted to be 40% of the total volume. The properties of constituent materials have been listed in Table 4.1. The frequency is normalized to $\omega a/2\pi C_t$, where $C_t = 1160\text{m/s}$ is the transverse wave speed in epoxy. The r_{\min} in the filter scheme in equation (3.16) is set to be 3.

Table 4.1: Mechanical properties of epoxy and Au

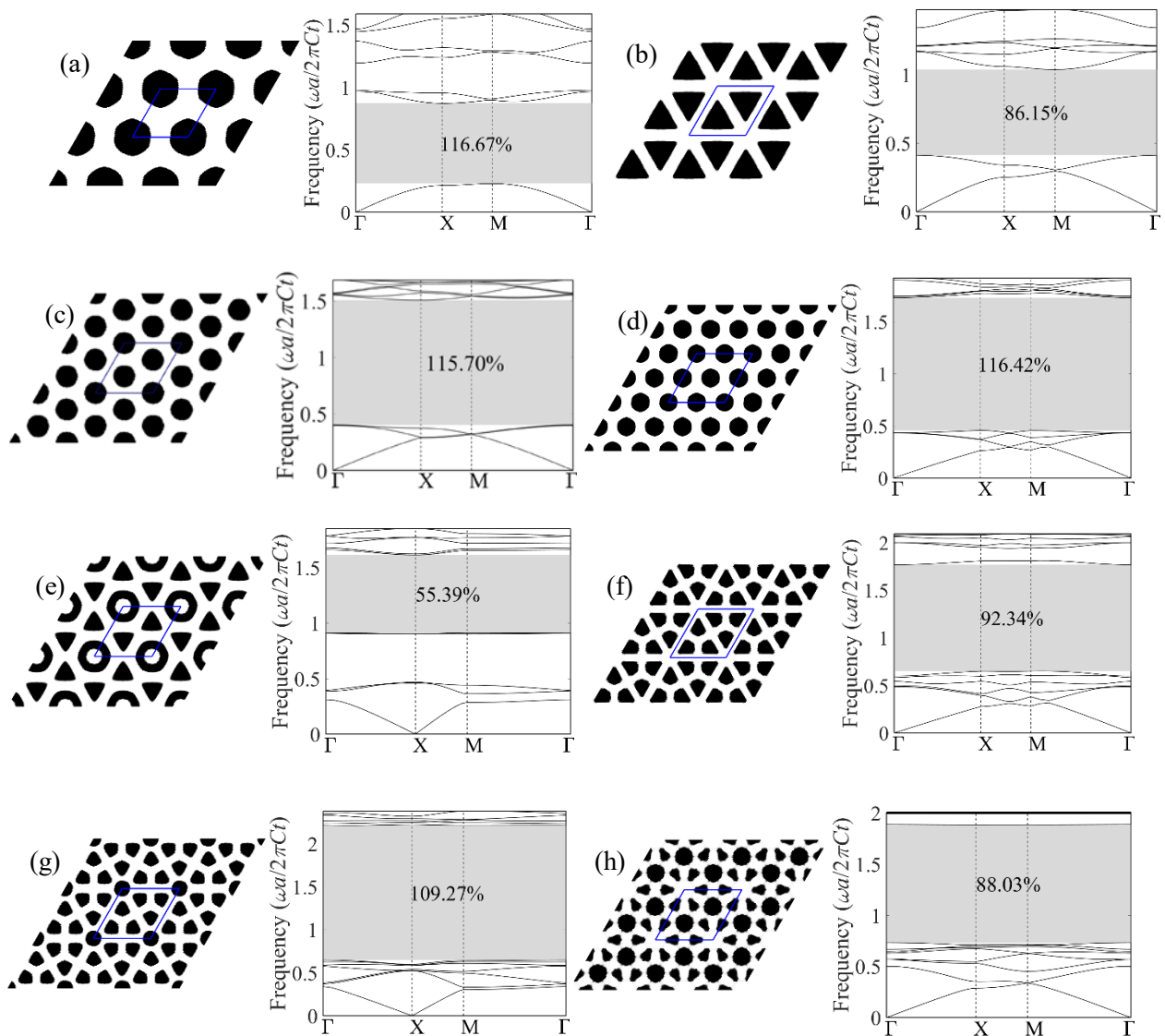
	ρ (kg/m ³)	λ (GPa)	μ (GPa)
Epoxy	1200	6.38	1.61
Au	19500	65.45	29.93

The topology optimization follows the process that has been elaborated in Chapter 3. It is noted that to solve equation (3.9), the wave vectors \mathbf{k} should be swept along the boundary of the first irreducible Brillouin zone ($\Gamma \rightarrow X \rightarrow M \rightarrow \Gamma$) as shown in Figure 4.1c.

4.3.1 Bandgaps for out-of-plane waves

In this example, the optimization objective is to find the maximum bandgaps for out-of-plane waves. Figure. 4.2 presents the optimized topologies of phononic bandgap crystals and

their corresponding band diagrams for the first ten bandgaps. The phononic bandgap crystals are shown with 3×3 arrays of unit cells, and the primitive unit cells are given in the rhombus boxes. It is noted that we opened the bandgaps between two adjacent bands at the different positions in the band diagram; thus in the following paragraphs, the first phononic bandgap means there is one band below the bandgap in its band diagram in Figure 4.2, whose band order is one; the second bandgap denotes there are two bands below the bandgap, whose band order is two, and so on.



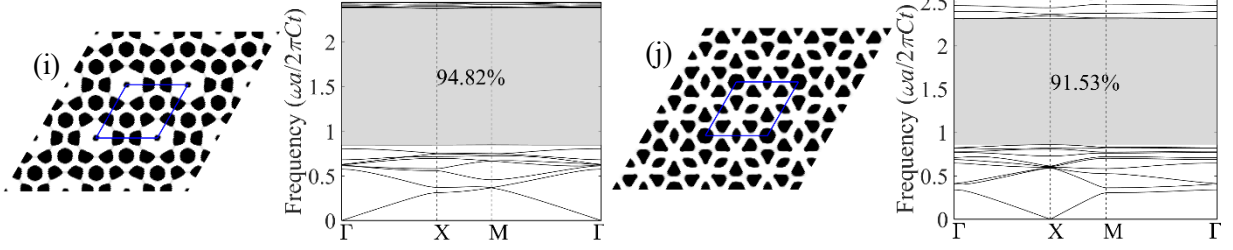


Figure 4.2. Optimized hexagonal-latticed phononic bandgap crystals and their band diagrams for out-of-plane waves; (a) the first bandgap; (b) the second bandgap; (c) the third bandgap; (d) the fourth bandgap; (e) the fifth bandgap; (f) the sixth bandgap; (g) the seventh bandgap; (h) the eighth bandgap; (i) the ninth bandgap; (j) the tenth bandgap.

The band diagrams indicate that all bandgaps are successfully opened, and the maximum gap width 116.67% is the first bandgap and the minimum gap width 55.39% is the fifth bandgap. Table 4.2 compares the bandgap size of PnCs with hexagonal lattice and square lattice [22]. The maximum bandgap is at the first bandgap for both lattices. The bandgap size of the hexagonal-latticed phononic crystal is about 10% larger than that of the square-latticed phononic crystal, about 106%. This further confirms the previous conclusion that hexagonal-latticed phononic bandgap crystals could present wider bandgaps than square-latticed phononic bandgap crystals [12, 16]. However, the gap size for PnCs with hexagonal lattice may not always larger than that of the square lattice, e.g., the second and eighth bandgaps. This well indicates that the lattice type has a substantial impact on the formation and size of the bandgap.

Table 4.2: Relative bandgap size of phononic bandgap crystals for out-of-plane waves with hexagonal lattice and square lattice

	Hexagonal lattice	Square lattice
the first band	116.67%	106.13%
the second band	86.15%	105.43%
the third band	115.70%	77.15%
the fourth band	116.42%	105.01%
the fifth band	55.39%	87.40%
the sixth band	92.34%	81.96%

the seventh band	109.27%	104.59%
the eighth band	88.03%	105.25%

As expected, all the optimized topologies of hexagonal-latticed phononic bandgap crystals are different from those of the square-latticed phononic bandgap crystals as reported in [22]. Many triangular and flower petal-shaped inclusions are formed for the hexagonal-latticed phononic bandgap crystals. Such shaped inclusions may provide better scattering properties and attribute to the increase of gap width in some cases. However, the optimized topologies of the two lattice types still share some similarities. Firstly, the heavier and stiffer material (Au) is isolated and embedded in the lighter and softer material (Epoxy). Secondly, the complexity of the optimized topologies increases with the band order. Thirdly, the distribution of inclusions in most cases follows the periodic centroidal Voronoi diagram in analogy to the law that was previously noticed in photonic bandgap crystals by Sigmund and Hougaard [142].

BESO starts from a randomly generated primitive unit cell in the above examples, but different initial guess designs may lead to different solutions. For example, Figure 4.3 shows three initial guess designs and their corresponding solutions aiming at maximizing the gap between the third and fourth bands. Although the target bandgaps successfully achieved for all cases, the optimized bandgap size and topology are different. Those topologies provide engineers with more options for designing phononic bandgap crystals. Nevertheless, it also indicates that the proposed BESO method may lead to a local optimum, which highly depends on initial guess design. In order to obtain the possible maximum bandgap, it is suggested that more initial guess designs can be tested for the current BESO method.



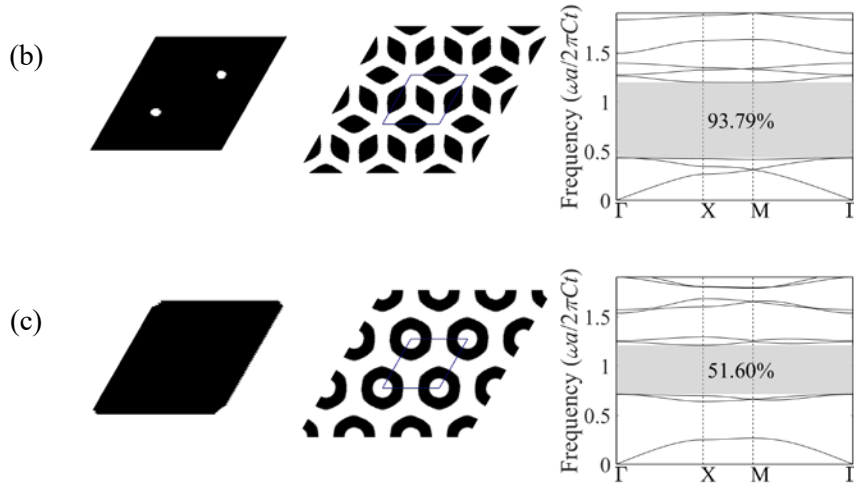
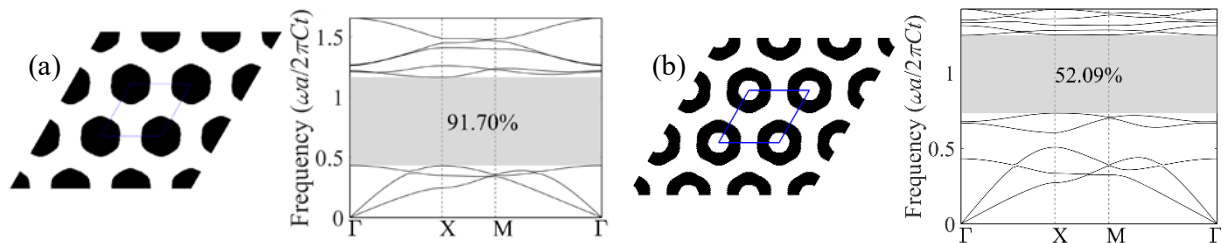


Figure 4.3. Different optimized results from three initial topologies

4.3.2 Bandgaps for in-plane waves

This example aims to optimize bandgaps for in-plane waves, where longitudinal and in-plane shear waves are coupled together. The resulting optimized topologies and their band diagrams are listed in Figure 4.4. The obtained maximum gap is the third bandgap, with the size of 91.70% and the minimum gap is the fifth bandgap, with the size of 52.09%. Table 4.3 compares the optimized bandgap size of in-plane waves for PnCs with hexagonal lattice and square lattice [22]. Similar to out-of-plane waves, the bandgap size depends from case to case. Compared with the square lattice [22], the hexagonal lattice has a larger bandgap between the third band and the fourth band, as shown in Figure 4.4a, which is close to circular inclusions extensively investigated [26].



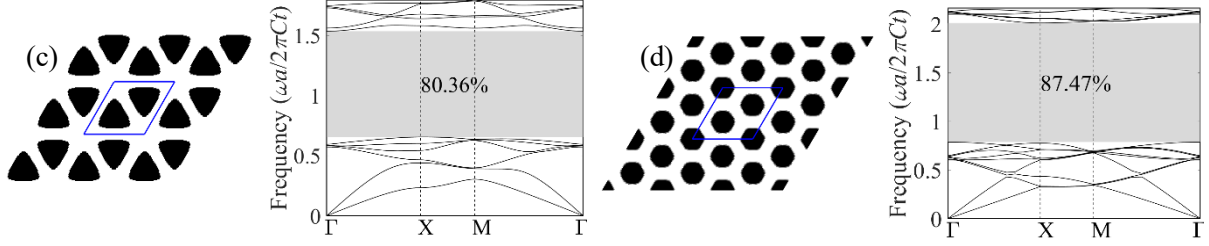


Figure 4.4. Optimized hexagonal-latticed phononic bandgap crystals and their band diagrams for in-plane waves; (a) the third bandgap; (b) the fifth bandgap; (c) the sixth bandgap; (d) the ninth bandgap.

Table 4.3: Relative bandgap size of phononic bandgap crystals for in-plane waves with hexagonal lattice and square lattice

	Hexagonal lattice	Square lattice
the third band	91.70%	87.00%
the fifth band	52.09%	48.99%
the sixth band	80.36%	86.73%
the eighth band	×	57.26%

In all cases, the heavier and stiffer material (Au) is also isolated and embedded in the lighter and softer material (epoxy). Different from the optimized square-latticed phononic bandgap crystals with nearly circular rods and ring inclusions [22], the optimized hexagonal-latticed phononic bandgap crystals are with nearly hexagonal rod and ring, triangular rod inclusions. This difference can reasonably attribute to the scattering properties of inclusion under the different lattice type.

Topology optimization of bandgaps for in-plane waves is extremely complicated due to the coupled longitudinal and shear waves. The current BESO method failed to obtain a solution at other bands e.g. the eighth bandgap identified for the square lattice [22]. The topology for the square lattice had a rod inclusion and a ring inclusion in the primitive unit cell as identified in [144]. However, it is impossible to have a rod and a ring simultaneously to construct a sixfold symmetric topology for the hexagonal lattice. To obtain the eighth bandgap for the hexagonal lattice, it is necessary to reducing symmetry constraint from the sixfold symmetry to the

threefold symmetry as shown in Figure 4.5a. With the reduction of the symmetry, the corresponding irreducible Brillouin zone has to be expanded as given in Figure 4.5b. As a result, the optimized topology for the eighth bandgap and its band diagram are shown in Figure 4.5c, which clearly indicates that the eighth bandgap with 53.75% is successfully obtained.

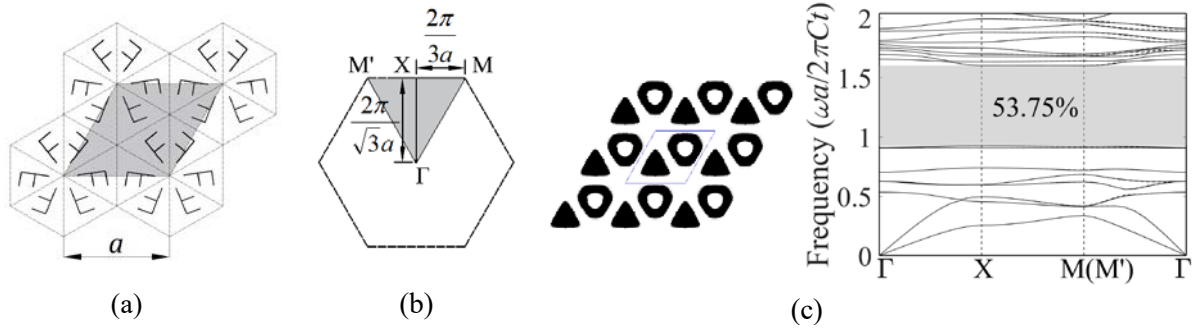


Figure 4.5. (a) Three-fold symmetry and selection of the primitive unit cell (shaded area). (b) Irreducible Brillouin zone of the hexagonal lattice with the three-fold symmetry (Γ -X-M (M')- Γ). (c) Optimized hexagonal-latticed phononic crystal with the three-fold symmetry and its band diagrams for in-plane waves.

The volume fraction may also affect the bandgap size of optimized PnCs. Take maximizing the bandgap between the third and fourth bands as an example, Figure 4.6 shows the optimized topologies and their band diagrams for different volume fractions. With a volume fraction of 70%, the optimized topology of the primitive unit cell is a rounded hexagonal inclusion embedded in the matrix. With the decrease of the volume fraction V_f , the rounded hexagonal inclusion becomes smaller and smaller; meanwhile, the bandgap size gradually increases and achieves its maximum value, 91.70%, around $V_f = 40\%$. Further decreasing the volume fraction causes that the hexagonal inclusion turns into the circular rod and ring and the bandgap size decreases accordingly. It seems that $V_f = 40\%$ is the best volume fraction and was chosen for all our numerical examples. Even so, we also noticed that the best volume fraction for maximizing bandgap could depend from case to case.

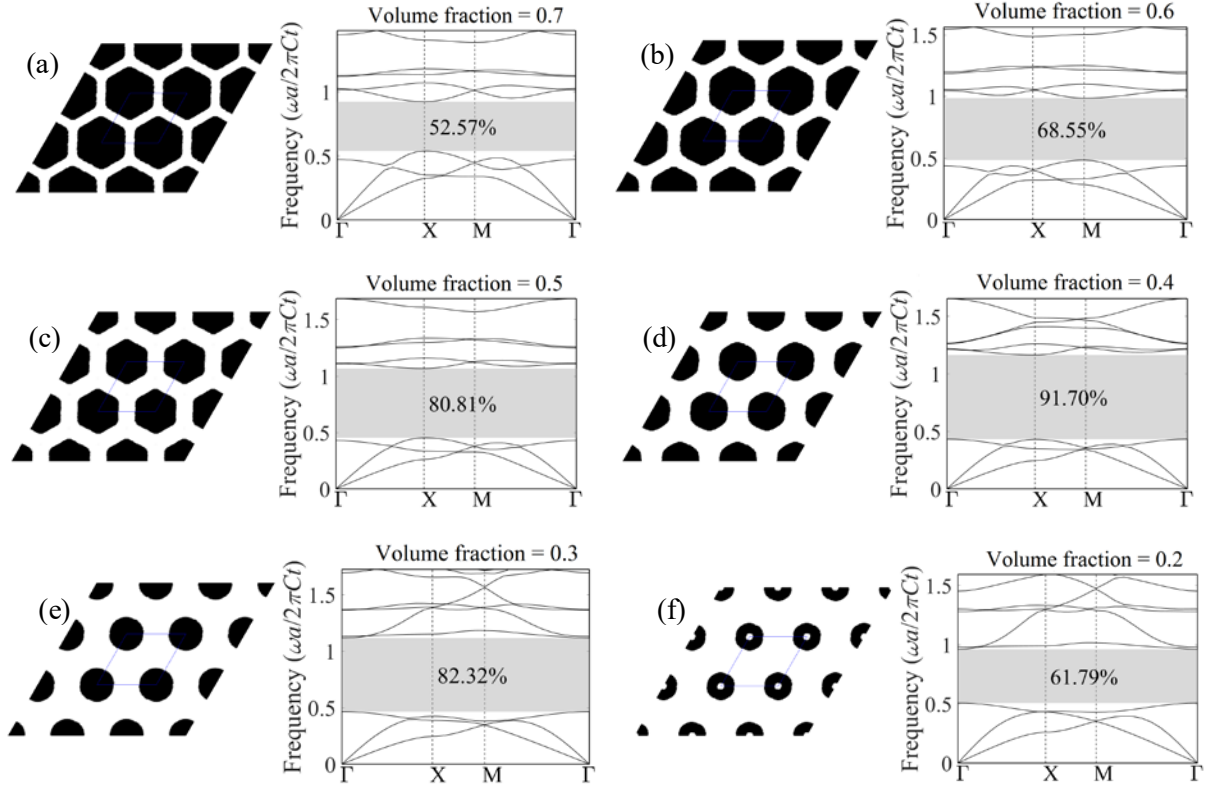


Figure 4.6. Optimized hexagonal-latticed phononic bandgap crystals and their band diagrams for in-plane waves with the third bandgap at the volume fraction from 70% to 20%.

4.3.3 Complete bandgaps for both out-of-plane and in-plane waves

It is of significance to find complete bandgaps of PnCs, in which any propagating Bloch waves are forbidden, whatever the direction of incidence and the polarization. Complete bandgap crystals require both out-of-plane and in-plane bandgaps. However, it is still challenging to optimize the complete bandgap since the proper combination of band orders between out-of-plane and in-plane waves can hardly be determined by a *priori* assumption. Among them, in-plane bandgaps are significantly harder to achieve than out-of-plane ones according to our optimization work. Therefore, our priority is to guarantee in-plane bandgaps. Accordingly, it is more feasible to open and enlarge complete bandgaps from our optimized in-plane topologies than from randomly generated designs and optimized out-of-plane topologies. Fortunately, after calculation, we found that both an out-of-plane bandgap and an in-plane bandgap appeared in all the results in Figure 4.4, from which we conducted optimization and achieved desired results listed in Figure 4.7. Their band diagrams show that the complete bandgaps for both out-of-plane and in-plane waves are successfully obtained. As expected, the optimized topologies are similar to the solutions above, with nearly hexagonal and triangular

rods and rings.

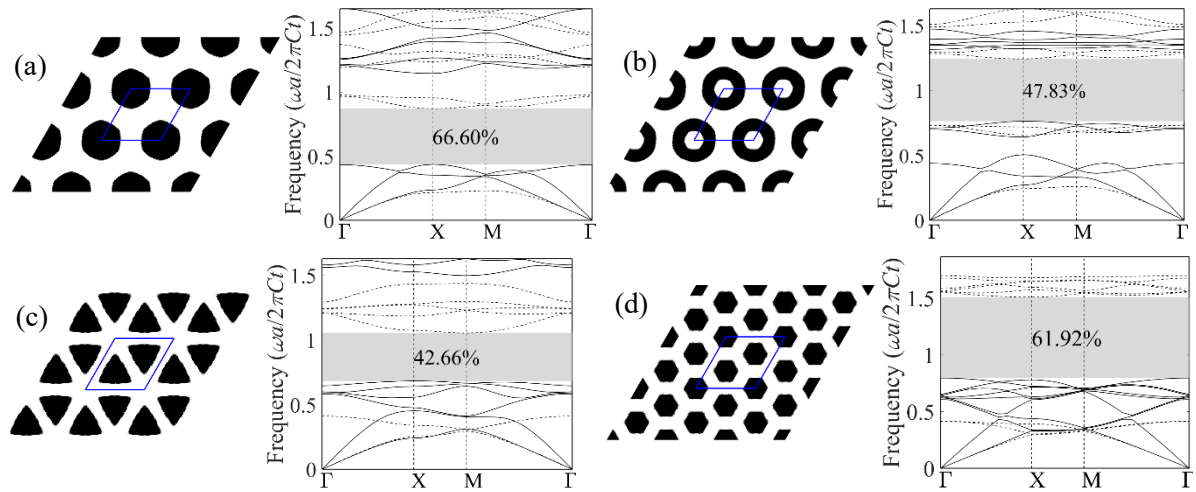


Figure 4.7. Optimized hexagonal-latticed phononic bandgap crystals and their band diagrams for the complete bandgap; (a) the third in-plane bandgap and the first out-of-plane bandgap; (b) the fifth in-plane bandgap and the third out-of-plane bandgap; (c) the sixth in-plane bandgap and the second out-of-plane bandgap; (d) the ninth in-plane bandgap and the third out-of-plane bandgap. In the band diagrams, dot lines denote the bands of out-of-plane waves and solid lines denote the bands of in-plane waves.

4.3.4 Wave transmission for finite PnCs

PnCs are assumed to be infinite and arranged periodically along the plane and only evanescent waves within a bandgap are allowed to transmit with the exponential decrease [145]. Therefore, it is necessary to check the transmission spectrum for a finite phononic structure. Based on the optimized design for the complete bandgap shown in Figure 4.7c, the finite phononic structure is formed by ten layers of the primitive unit cell along the direction of wave propagation as shown in Figure 4.8 and simulated by the commercial FEM software, Comsol Multiphysics. Both left and right boundaries are defined as the perfect matched layers in order to reduce the interference of reflective waves. The incident wave excitation is applied on the left side of the phononic bandgap crystals, and the transmitted response is measured on the right side as shown in Figure 4.8. The periodic boundary condition is applied at the top and bottom edges.

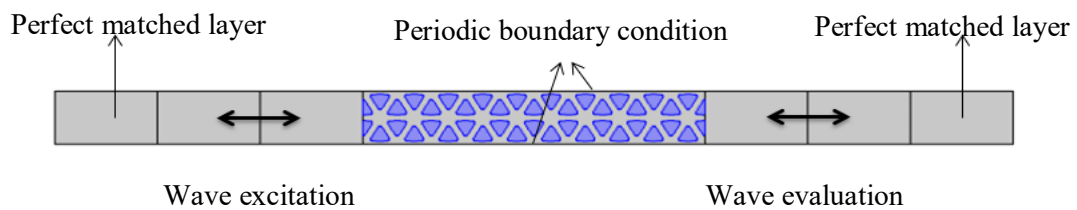


Figure 4.8. Model for transmission analysis in COMSOL Multiphysics.

It should note that the transmission of out-of-plane waves cannot be directly simulated in Comsol Multiphysics. Fortunately, the governing equation of out-of-wave is formally equivalent to the acoustic wave equation in fluid-fluid PnCs by substituting $1/\mu$ and $\sqrt{\mu/\rho}$ for mass density and wave speed, respectively [60]. The resulting pressure field is equivalent to out-of-plane displacement in solid-solid PnCs. The transmission coefficient is defined by

$$TC = 10 \times \log_{10}(A_t/A_i) \quad (12)$$

where A represents either out-of-plane displacement or in-plane acceleration amplitude. The subscripts t and i denote transmission and incidence, respectively.

The calculated transmission spectrum for the phononic structure along Γ -X direction is shown in Figure 4.9 for incident in-plane longitudinal (P), transverse (S), and out-of-plane waves, respectively. It can be seen that there are significant drops in transmission coefficient for out-of-plane waves at normalized frequency 0.4-1.04, and for in-plane P and S waves at normalized frequency 0.64-1.49. Those frequency ranges correspond to the bandgaps for out-of-plane waves and in-plane waves as shown in Figure 4.7c. The overlap between them indicates the complete bandgap between frequency 0.64-1.04.

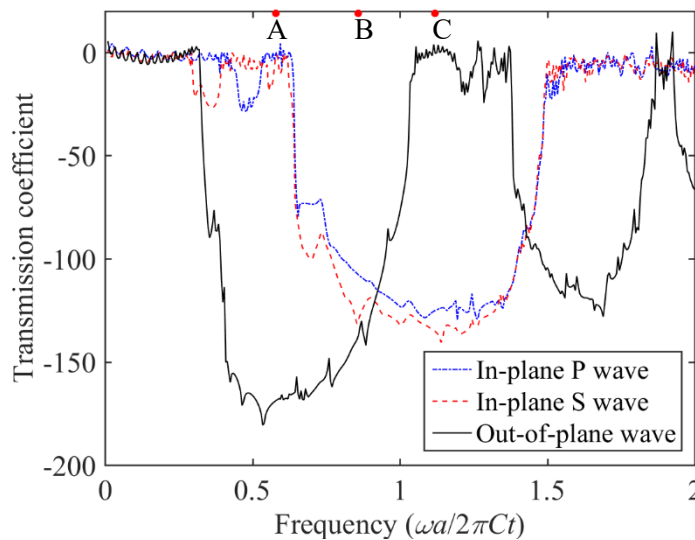


Figure 4.9. The transmission spectrum of waves propagating along the Γ -X direction for the phononic structure shown in Figure 4.8.

We can further investigate the field distributions at three typical frequencies, 0.58, 0.86 and 1.12 which correspond to points A , B and C as shown in Figure 4.9. The simulation field distributions are shown in Figures 4.10, 4.11 and 4.12 for the normalized frequency 0.58, 0.86, and 1.12, respectively. Figure 4.10 shows the out-of-plane waves are quickly evanescent but in-plane P waves and S waves are

transmitted through the phononic structure at the normalized frequency 0.58. When the normalized frequency is 0.86, all waves are quickly evanescent, and no wave can be transmitted through the phononic structure as shown in Figure 4.11. At the normalized frequency 1.12, it can be observed from Figure 4.12 that the out-of-plane wave is transmitted through the phononic structure but the in-plane P wave and S wave are quickly evanescent. All those results agree well with the band diagram in Figure 4.7c and the transmission spectrum in Figure 4.9.

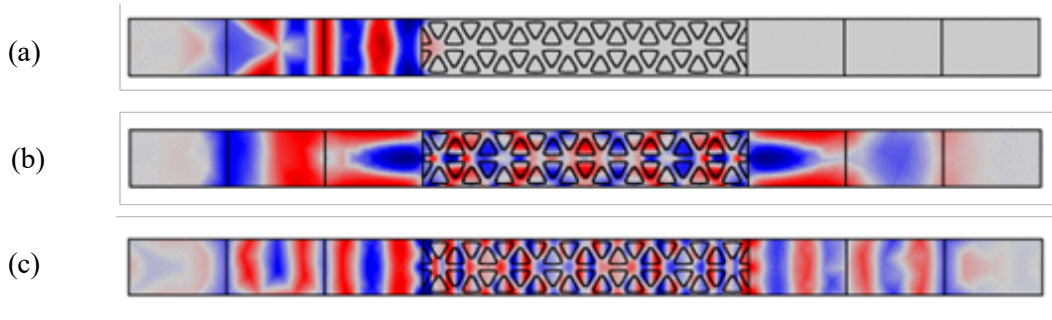


Figure 4.10. The field distributions of elastic waves at the normalized frequency, 0.58: (a) displacement distribution of the out-of-plane wave; (b) acceleration distribution of the in-plane P wave; and (c) acceleration distribution of the in-plane S wave.

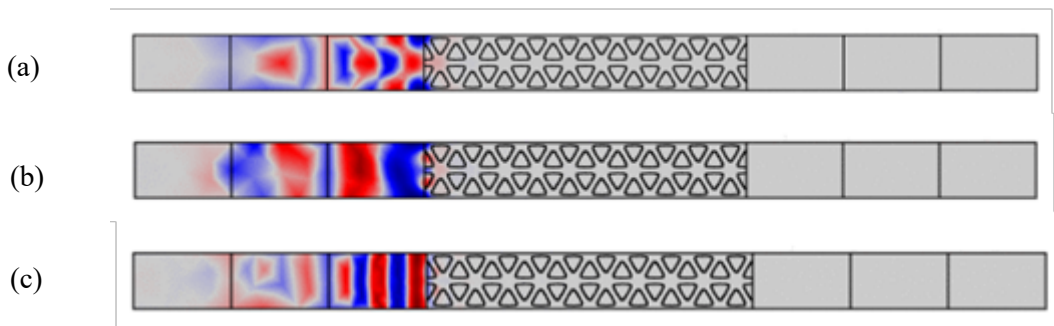


Figure 4.11. The field distributions of elastic waves at the normalized frequency, 0.86: (a) displacement distribution of the out-of-plane wave; (b) acceleration distribution of the in-plane P wave; and (c) acceleration distribution of the in-plane S wave.

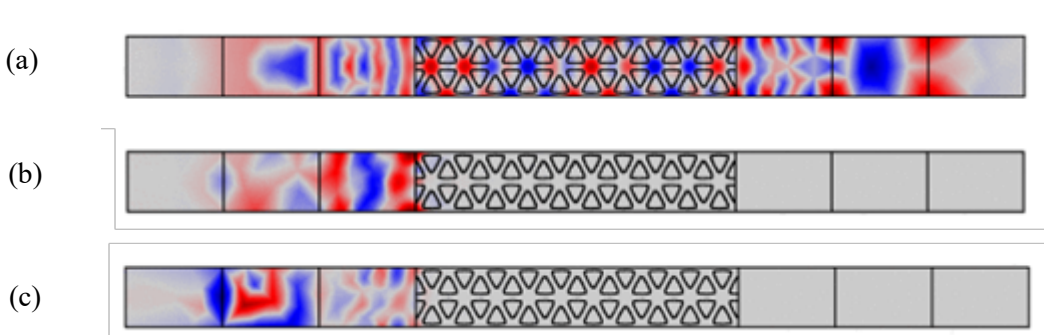


Figure 4.12. The field distributions of elastic waves at the normalized frequency, 1.12: (a) displacement

distribution of the out-of-plane wave; (b) acceleration distribution of the in-plane P wave; and (c) acceleration distribution of the in-plane S wave.

4.4 Conclusions

This paper has presented the optimization results from the established topology optimization procedure of hexagonal-latticed PnCs based on FEM and BESO for maximizing specified bandgaps. Our numerical examples demonstrate the effectiveness of the proposed method and some innovative designs with 6-fold symmetric hexagonal lattice are obtained for bandgaps of out-of-plane, in-plane and combined waves. The results are systematically compared with optimized phononic bandgap crystals with square lattice [22]. Meanwhile, the proposed BESO method is extended to achieve complete bandgaps, which are independent of the direction of wave incidence and polarization. The optimized phononic crystal is further used for constructing the finite phononic structure. The results demonstrate that the transmission and forbiddance of the out-of-plane and in-plane waves occur at different frequency ranges as expected. The proposed topology optimization provides a useful approach to designing hexagonal-latticed PnCs with large bandgaps. Due to the requirement of the six-fold symmetry of PnCs, it is hard to obtain optimized solutions of some specified bandgaps for in-plane waves. In those cases, reducing symmetry constraint, e.g., from the six-fold to three-fold symmetry, is necessary. Meanwhile, the selection of initial design influences the optimized bandgap and topology.

Chapter 5. Topology optimization for the 2D phononic bandgap crystals with the reduced symmetry

5.1. Introduction

PnCs have been a topic of great interest for several years [146], and many state-of-the-art techniques including topology optimization have been employed to engineer the phononic bandgap [59]. However, in the majority of the phononic bandgap optimization works, the lattices are considered to be symmetric. Under such assumption, the band diagram calculation only takes the wave vectors over the irreducible Brillouin zone edges into consideration [40]. Besides, the four-fold and six-fold symmetries reduce the design variable to $1/8$ and $1/12$ of the unit cell for the square and the hexagonal lattice. As a result, the computational cost has been alleviated to the minimum extent. However, from the viewpoint of optimization, the prescribed symmetry, as an extra constraint in the geometry of the unit cell, abates the possibility of achieving broad phononic bandgaps.

Previous topology optimization attempts involving the symmetry breaking on the acoustic, porous and solid PnCs [18, 136, 139] reveals the bandgap size benefits from symmetry breaking. Gazonas et al. [18] employed the GA method and the FEM method to carry out phononic bandgap design for two-dimensional acoustic wave structures with an arbitrarily asymmetric lattice. In Dong et al.'s research [139], the optimization process is based on multiple objectives of simultaneously maximizing the bandgap size and minimizing the volume fraction under different symmetry assumptions. By gradually breaking the symmetry of both square and hexagonal lattice for two-dimensional porous PnCs, the bandgap size of the optimized porous phononic structures increases. In the field of two-dimensional solid-solid PnCs, Dong et al. [136] linked the FDTD method with the multiple elitist GA method with adaptive fuzzy fitness granulation for the phononic bandgap engineering. With this technique, they achieved larger bandgap size in the asymmetric PnCs than in the symmetric ones for the out-of-plane and combined wave modes, but the attempt for in-plane mode failed to exhibit wider bandgap. Due to the enormous computational load, only a limited number of results are reported in their research with the square lattice, and the hexagonal lattice is not considered, which is not enough for a comprehensive understanding on how the symmetry influences the optimal solution for the different lattices and for different band orders in the two-dimensional

solid phononic bandgap crystals.

The above works are based on GAs that inevitably comes with heavy computational loads, and thus, a faster and more efficient topology optimization technique other than GAs is worthwhile to be attempted. In this chapter, the topology optimization for asymmetrical 2D phononic bandgap crystals with both square lattice and the hexagonal lattice is conducted by using the BESO method in conjunction with the FEM. The base materials used for constructing the unit cell in this study are Pb and epoxy, same as in [136] to show the improvement of the solutions.

The rest of this chapter is organized as follows: Section 5.2 states different lattices and symmetries. Detailed optimization results and discussions for the out-of-plane, in-plane and combined out-of-plane and in-plane modes are presented in Section 5.3. This is followed by conclusions in Section 5.4.

5.2 Lattice types and symmetries

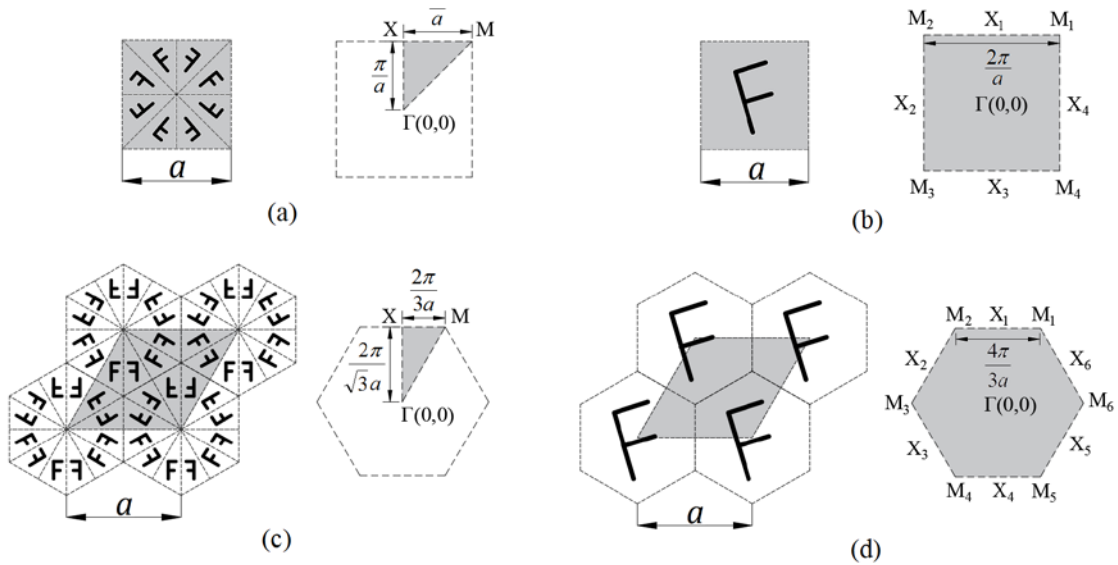


Figure 5.1. (a) C_{4v} square lattice; (b) C_1 square lattice; (c) C_{6v} hexagonal lattice; (d) C_1 hexagonal lattice. Left: unit cells (grey area) and symmetry. Right: the first Brillouin zone and irreducible Brillouin zone (grey area) in the reciprocal lattice.

Among five classic Bravais lattices in the 2D system, we take the square lattice and the hexagonal lattice as examples to investigate the influence of symmetry on bandgap width because the square lattice and the hexagonal lattice have the highest 2D symmetry. Figure 5.1

illustrates the symmetry in the primitive unit cell for (a) symmetric square lattice, (b) asymmetric square lattice, (c) symmetric hexagonal lattice, (d) asymmetric hexagonal lattice and their reciprocal lattices. The symmetric square lattice has 4-fold reflection symmetry and 4-fold rotational symmetry (C_{4v}) and the symmetric hexagonal lattice has 6-fold reflection symmetry and 6-fold rotational symmetry (C_{6v}) while the asymmetric square and hexagonal lattice only have a onefold rotational symmetry (C_1). The irreducible Brillouin zones of symmetric structures constitute 1/8 and 1/12 of the first Brillouin zones for the square lattice and the hexagonal lattice, respectively; while the irreducible Brillouin zones of asymmetric structures comprise the entire first Brillouin zones for both lattices. However, owing to time-reverse symmetry $\omega(\mathbf{k}) = \omega(-\mathbf{k})$ [147], the wave vector required in asymmetric calculation reduces to half of the first Brillouin zone.

5.3. Optimization results and discussion

In this section, numerical optimization results of two-component solid phononic bandgap crystals will be presented. Different lattices and symmetries are considered, i.e., the C_{4v} and C_1 symmetry in the square lattice, and the C_{6v} and C_1 symmetry in the hexagonal lattice. In the following examples, the primitive unit cell is mapped to a fine 64×64 grid in resolution, same with the mesh used in Chapter 4. Material phases in use are Epoxy as material 1 and Pb as material 2 and their physical properties have been listed in Table 5.1 in which ρ represents the mass density, C_l longitudinal wave speed, and C_t transverse wave speed. The frequency is normalized to $\omega a / 2\pi C_t$, where $C_t = 1160 \text{m/s}$ is the transverse wave speed in epoxy.

Table 5.1: Mechanical properties of epoxy and Pb

	ρ (kg/m ³)	C_l (m/s)	C_t (m/s)
Epoxy	1200	2830	1160
Au	19500	2158	860

In the calculation of band diagram and derivation of the sensitivity numbers, the construction of the element stiffness matrix in equation (A4) requires the Lamé's constants λ and μ which

can be converted from the wave speeds of the materials by

$$\mu = \rho \cdot C_t^2 \quad (5.1)$$

$$\lambda = \rho \cdot C_l^2 - 2\mu \quad (5.2)$$

The topology optimization is based on BESO in combination with FEM, whose implement has been elaborated in Chapter 3. It is noted that to solve equation (3.9), for the C_{4v} and C_{6v} symmetry, the wave vectors \mathbf{k} should be swept along the boundary of the first irreducible Brillouin zone ($\Gamma \rightarrow X \rightarrow M \rightarrow \Gamma$); while for the asymmetrical case, the wave vectors \mathbf{k} must be swept over the edges over half of the first Brillouin zone ($\Gamma \rightarrow X_4(X_2) \rightarrow M_1(M_2) \rightarrow \Gamma \rightarrow X_1 \rightarrow M_1(M_2)$ for the C_1 square lattice and $X_6(X_2) \rightarrow M_6(M_3) \rightarrow \Gamma \rightarrow X_6(X_2) \rightarrow M_1(M_2) \rightarrow \Gamma \rightarrow X_1 \rightarrow M_1(M_2)$ for the C_1 hexagonal lattice) as shown in Figure 5.1. In the optimization process, no volume constraint is applied in order to obtain the possible largest bandgaps. The r_{\min} in the filter scheme equation (3.16) is set to be 3.

5.3.1 Square lattice

5.3.1.1 Bandgaps for out-of-plane waves

In this section, the bandgaps of the two-dimensional PnCs with C_{4v} and C_1 square lattice for the out-of-plane wave mode are optimized. To thoroughly investigate and analyze the characteristics of the asymmetric phononic bandgap crystals, the first fifteen optimized bandgap structures are presented in Figure 5.2 for the C_{4v} symmetry and in Figure 5.3 for the C_1 symmetry with the square lattice. The phononic bandgap crystals are shown with 3×3 arrays of unit cells and the primitive unit cells are given in the square boxes for their corresponding lattices.

It can be seen from Figure 5.2 and Figure 5.3, even though being deprived of the symmetry condition, the asymmetric optimized topologies still have two ordinary distribution laws with the symmetric designs. Firstly, the heavier and stiffer material Pb forms one and multiple inclusions isolated by the lighter and softer epoxy matrix. Secondly, the complexity of the optimized topologies increases along with the band order. To specify, the band order is equal to the number of the scatters (Pb) embedded in the epoxy in a unit cell for both C_1 symmetry

and C_{4v} symmetry.

It is noticed that in some cases, the topologies for the higher bandgaps are rotated and resized from those for the lower bandgaps. For C_{4v} symmetry, the optimized structures with the first, second, fourth and eighth bandgaps are very similar. The phononic crystal with the fourth bandgap in Figure 5.2d can be considered an augmented supercell consisting of 2×2 times the original unit cell of the phononic crystal with the first bandgap in Figure 5.2a. The PnCs with the second bandgap (Figure 5.2b) and the eighth bandgap (Figure 5.2h) turn out to be 45° -rotated augmented supercells of the phononic crystal with the first bandgap. The rule is found less common for the C_1 symmetric square lattice than C_{4v} square lattice as only the phononic crystal with the fifth bandgap (Figure 5.3e) with C_1 square lattice have the rotated augmented geometry.

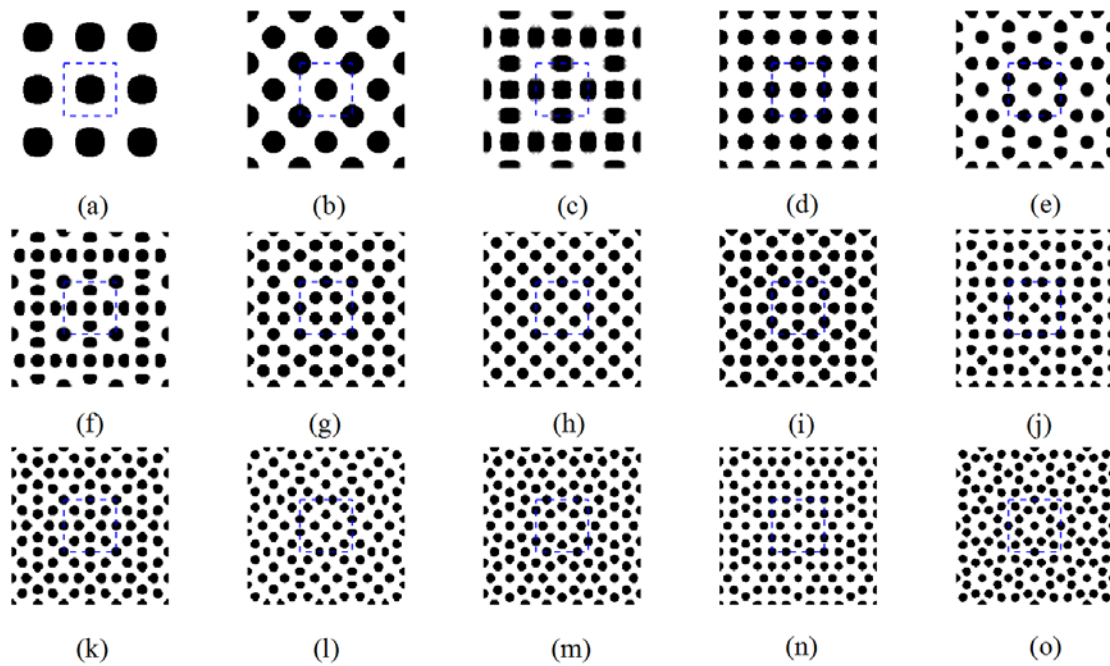
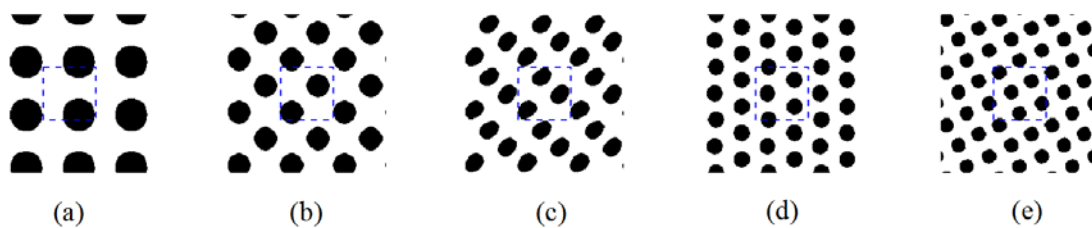


Figure 5.2. Optimized phononic bandgap crystals with the C_{4v} square lattice from the first bandgap to the fifteenth bandgap for the out-of-plane waves.



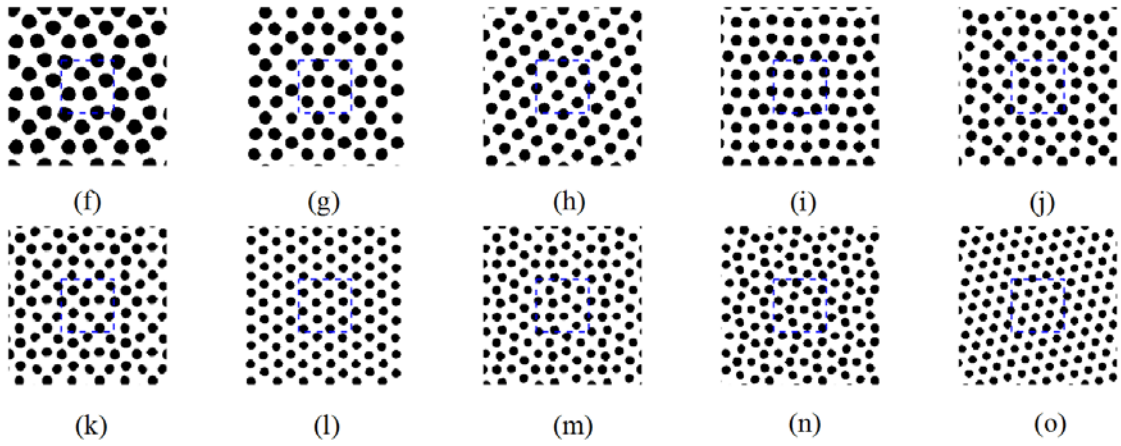


Figure 5.3. Optimized phononic bandgap crystals with the C_1 square lattice from the first bandgap to the fifteenth bandgap for the out-of-plane waves.

The relative bandgap sizes with C_{4v} and with C_1 square lattice are given in Figure 5.4. The biggest bandgap for the C_1 square lattice appears at the fifteenth bandgap, about 0.77, increasing by 7% compared with the widest symmetric bandgap: the seventh bandgap whose size is 0.72. The narrowest bandgap is the third bandgap for both C_1 and C_{4v} cases, whose size for the C_1 symmetry is 0.50, 6% wider than that for the C_{4v} symmetry, 0.47. The average bandgap size for the C_1 symmetry is 0.69, having a nearly 6% rise compared to that of the C_{4v} symmetry, 0.65. Therefore, for the out-of-plane wave mode, we can conclude that removing symmetry restriction yields a noticeable improvement in the gap size of the optimized PnCs.

However, the increase of bandgap size is not for all the results with the square lattice. The advantage of symmetry breaking is observed at the results for the third to sixth, eighth to tenth, twelfth to fifteen bandgaps; for the other bandgaps, the gap sizes of symmetric results failed to make a difference from those of the symmetric PnCs. For these bandgaps, the symmetric and asymmetric topologies are merely the translation of each other. This is because the symmetric solutions are truly optimal for these cases.

It is interesting to find that the scatters in the bandgap crystal with the fifteenth gap are arranged in the same way as a traditional hexagonal-lattice phononic crystal. Furthermore, at some band order with large gap size, such as fourth and sixth structures, in which the scatters are also hexagonally distributed and the bandgap sizes are much bigger than other non-hexagonally-distributed solutions. This trend validates the conclusion in Chapter 4 that the hexagonal lattice has an advantage in exhibiting bigger bandgap size than square lattice.

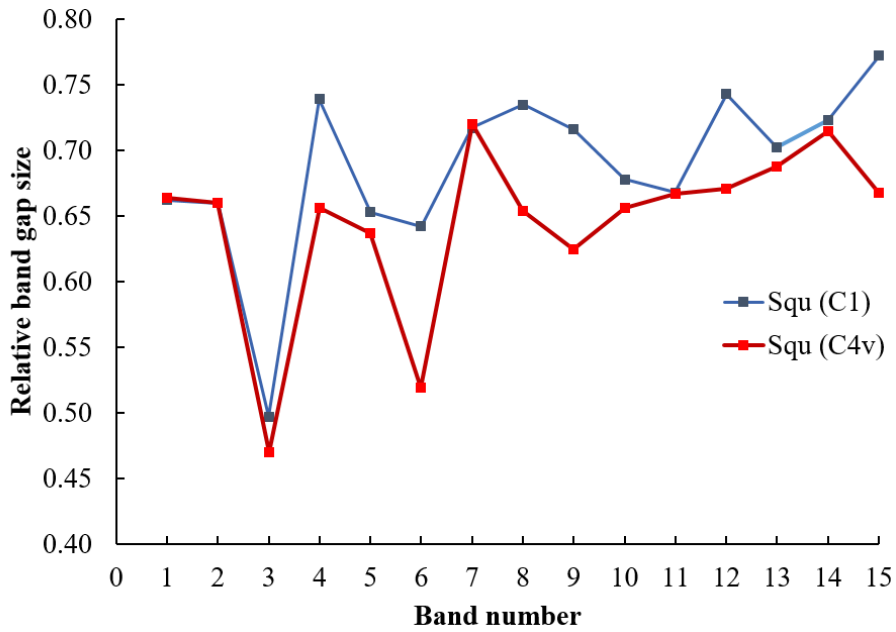


Figure 5.4. Relative phononic bandgap sizes with the C_1 and C_{4v} square lattice from the first bandgap to the fifteenth bandgap for the out-of-plane waves.

5.3.1.2 Bandgaps for in-plane waves

It is complicated to open phononic bandgaps for the in-plane mode due to the coupling of transverse and longitude waves. In the early years, only a few phononic bandgap structures can be obtained until Li et al. [144] discovered the connections between the topology and phononic bandgap order for in-plane waves, and therefore proposed a method to simplify the optimization process by using the initial designs.

In [144], results with large bandgaps are metal rods embedded in the epoxy matrix. They concluded that in the two-dimensional phononic structures with large bandgaps, the number of solid rods within the unit cell (usually square unit cell) is equal to one-third of the band order [144]. That means in our study with the material combination of Pb and epoxy, the third bandgap can be obtained by placing one solid Pb rod in the matrix; the sixth bandgap requires two Pb rods distributed in the unit cell, and so on. In [144], it is also mentioned that the ring shape scatters also activate bandgaps at the band order of five times scatter number; however, the average bandgap size of PnCs containing ring-shaped scatters is much lower than that with circular rods. In order to obtain wider bandgaps, we only consider topology with rod scatters.

In [144], the position of scatters is determined by the periodic centroidal Voronoi

tessellations (PCVT). The PCVTs for the square lattice has been developed [148, 149]. However, the PCVTs for the hexagonal lattice are necessary to investigate. The procedure to compute a PCVT is discussed, and the PCVTs for symmetric and asymmetric, square and hexagonal lattices are given in Appendix 2.

The PCVT-based initial designs are generated by filling Pb rods with the centers at the centroids of the PCVT, and the rest of the unit cell is filled with epoxy. For example, PCVT with nine seeds and the PCVT-based initial design with the C_1 hexagonal lattice are shown in Figure 5.5.

The radii of the rods are calculated as follow:

$$r = \sqrt{\frac{fa}{n\pi}} \quad (5.3)$$

where f is the volume fraction of Pb in the initial design; a is the area of the unit cell; n is the band order. Here, f is set at 0.4.

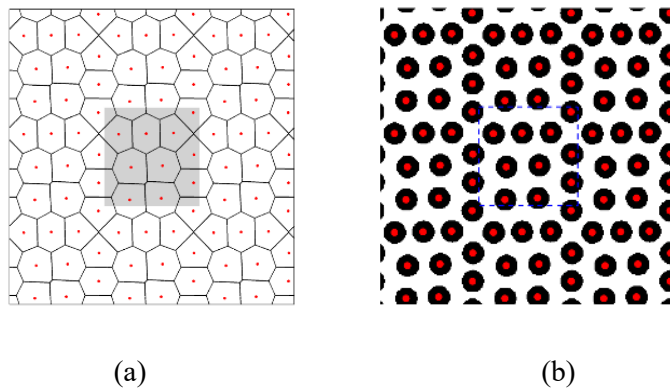


Figure 5.5. (a) PCVT at $n=9$; (b) PCVT-based initial design for the phononic bandgap crystal with the C_1 square lattice for the ninth bandgap.

The topology optimization for the in-plane waves is performed on the PCVT-based initial designs. Figure 5.6 and 5.7 shows the optimized topologies for C_{4v} symmetry and C_1 symmetry, respectively. The circular scatters in the initial designs are evolved into scatters of different shapes such as square, rectangle, circle, oval and triangle, but the positions of scatters are basically the same with the centroids in the PCVTs.

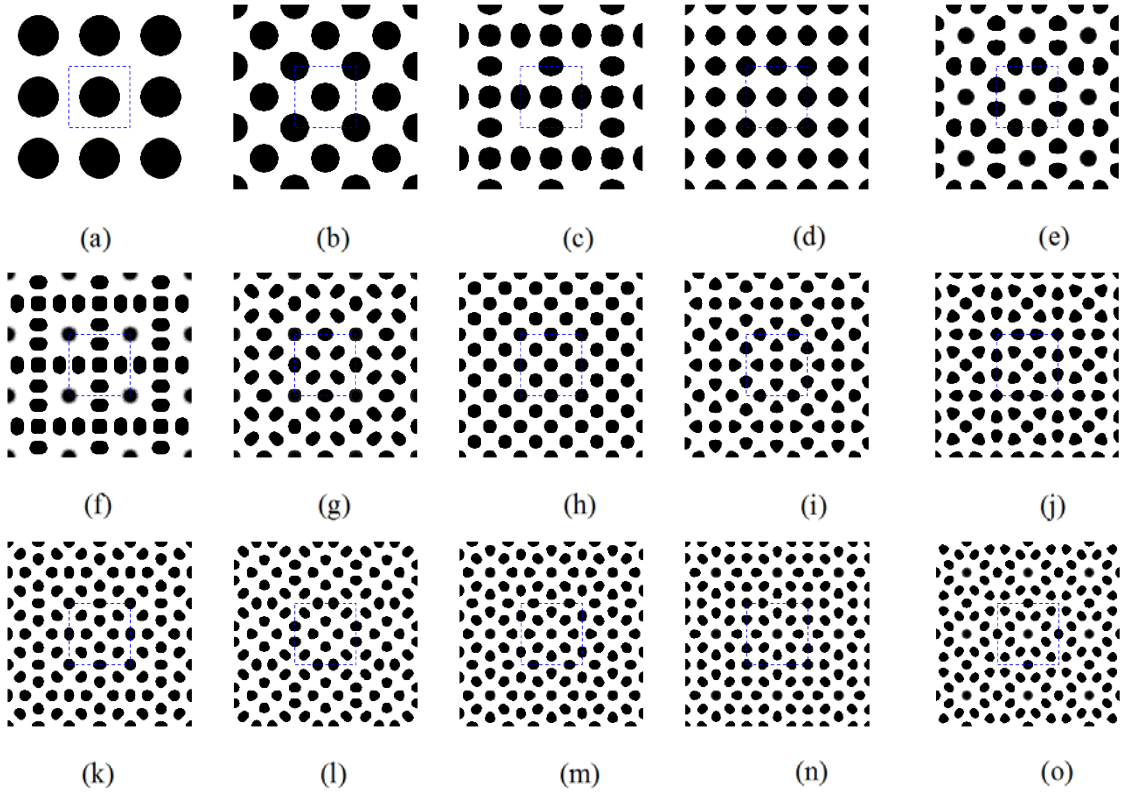


Figure 5.6. Optimized phononic bandgap crystals with the C_{4v} square lattice for the $(3n)^{\text{th}}$ bandgap from $n=1$ to $n=15$ for the in-plane waves.

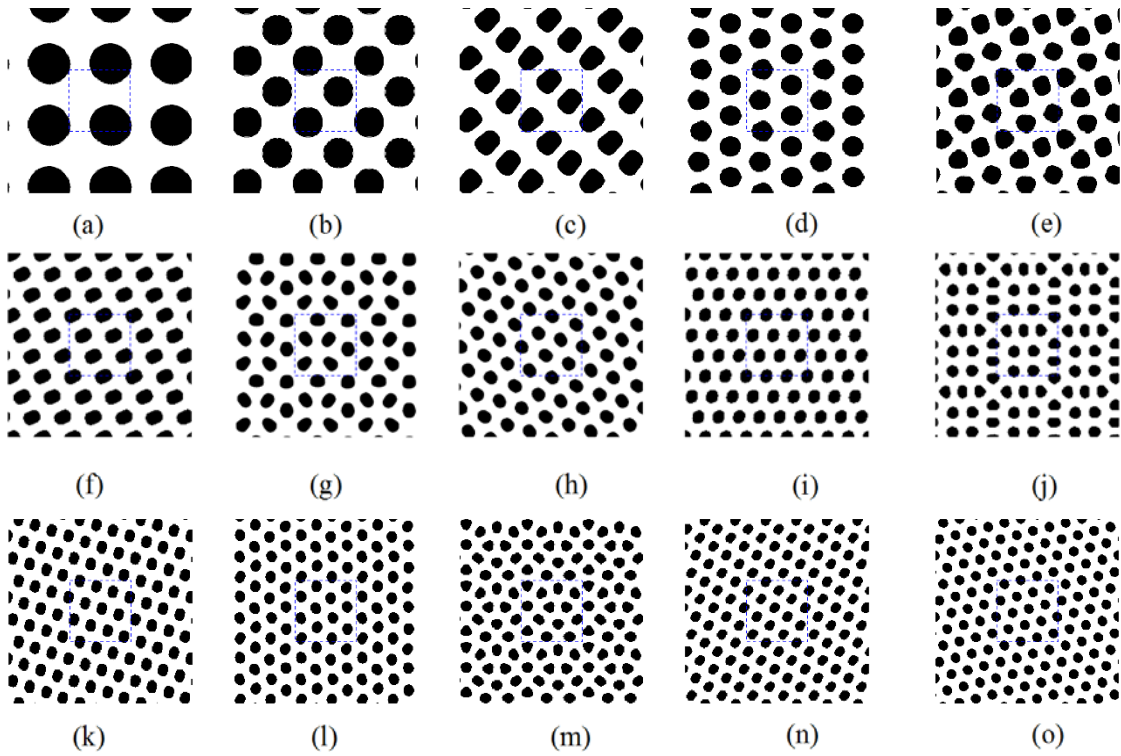


Figure 5.7. Optimized phononic bandgap crystals with the C_1 square lattice for the $(3n)^{\text{th}}$ bandgap from $n=1$ to $n=15$ for the in-plane waves.

Figure 5.8 shows the relative bandgap sizes for the C_{4v} and C_1 square lattice for the in-plane wave mode. The square-latticed PnCs with the twenty-first bandgap have the almost identical topologies for the C_{4v} and C_1 symmetry with the largest bandgap size of 0.464. It is the first time to present a two-dimensional solid phononic bandgap crystal for the in-plane wave mode whose bandgap is larger than the third bandgap, which illustrates the meaningfulness of the high-order bandgap maximization for the in-plane wave mode. Compared with the results reported in [136] whose in-plane bandgap sizes for C_{4v} and C_1 square lattice are 0.455 and 0.457 respectively, our optimized structures give even larger bandgaps. The smallest bandgap is the eighteenth bandgap with the size of 0.371 for the C_{4v} symmetry and the ninth bandgap with the size of 0.381 for the C_1 symmetry. The average bandgap size with the C_1 symmetry is 0.445, which is 4.3% bigger than average relative bandgap with the C_{4v} symmetry at 0.426. Compared with the out-of-plane wave mode, the symmetry reduction has a less impact on the in-plane bandgap size for the square lattice.

It is particularly interesting to notice that the results with the C_{4v} symmetry at the twenty-seventh and thirty-sixth bands are a little bit better than those with the C_1 symmetry at the same bands. This is quite different from the case with the square lattice for the out-of-plane wave mode, where all the solutions with the C_1 symmetry have bigger or equal bandgap sizes compared with those with the C_{4v} symmetry.

From the results, we also found the symmetry reduction will not affect the results when the PCVTs with or without symmetry are same. To specify, the results optimized from the initial designs based on the PCVTs in Figure A2.3b and Figure A2.4b are identical. Thus, at these band order, the symmetric designs are the best options because the large bandgap size and the low computational cost can be simultaneously achieved for the symmetric design.

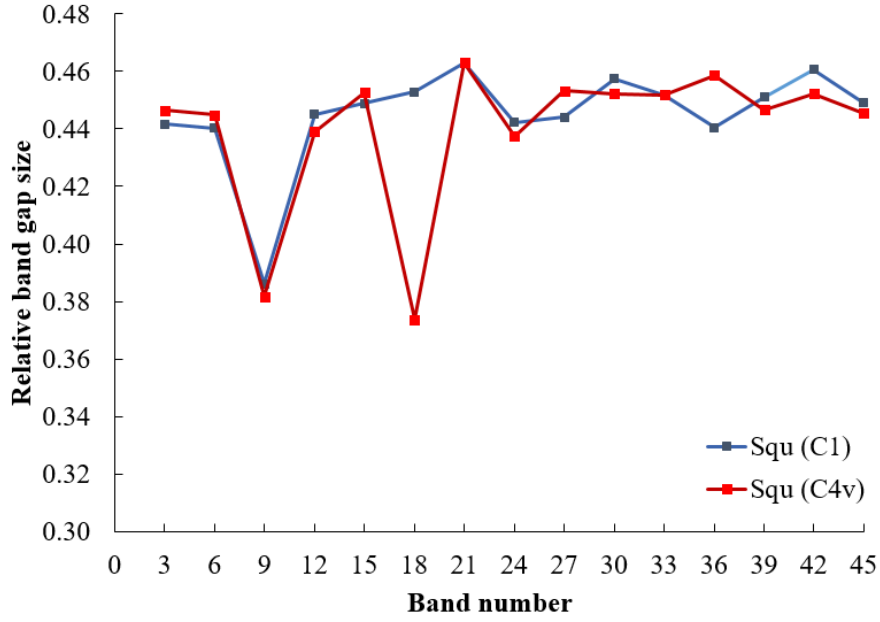


Figure 5.8. Relative phononic bandgap sizes with the C_1 and C_{4v} square lattice for the $(3n)^{\text{th}}$ bandgap from $n=1$ to $n=15$ for the in-plane waves.

5.3.1.3 Complete bandgaps for both out-of-plane and in-plane waves

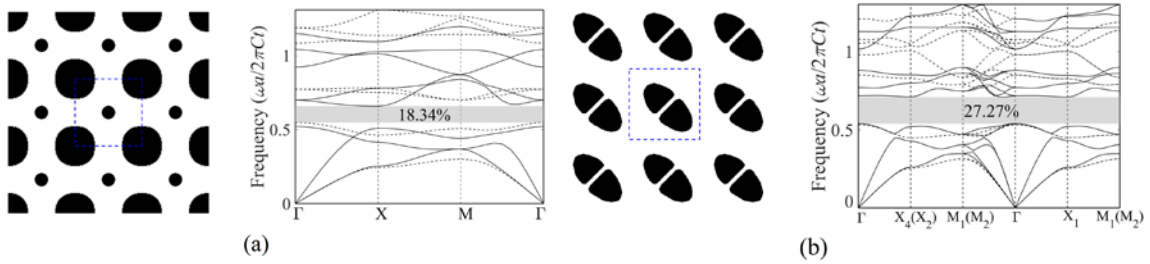


Figure 5.9. Optimized square-lattice phononic bandgap crystals and their band diagrams for the complete bandgap between the second out-of-plane bandgap and third in-plane bandgap (a) with the C_{4v} symmetry; (b) with the C_1 symmetry. In the band diagrams, dot lines denote the bands of the out-of-plane waves and solid lines denote the bands of the in-plane waves.

Complete bandgaps are complicated to open because it requires both out-of-plane and in-plane bandgaps. According to Section 4.3, the complete bandgap may exist in the optimized in-plane structures. After optimization starting with the optimized in-plane results in the last section, only narrow complete bandgaps with the size less than 0.15 are obtained, and the topologies of the complete-bandgap results are very similar with the optimized in-plane results. This is because the out-of-plane bandgap resides in the much higher frequency than the in-plane bandgap and only a portion of bandgaps overlap to form complete bandgaps. On the contrary, the two results with the C_{4v} and C_1 square lattice shown in Figure 5.9 have the

narrower out-of-plane and in-plane bandgaps; but the gaps match well to exhibit relatively large complete bandgaps.

From Figure 5.9a, the solution with the C_{4v} symmetry contains two scatters of different sizes. In Figure 5.9b, each of the two scatters in the solution with the C_{4v} symmetry resembles a semi-ellipse. The two semi-ellipses are of the similar size and are separated to form a tunnel in between along the minor axis of the semi-ellipses. The complete bandgap size for the C_1 symmetry is 0.273, 49% bigger than that for the C_{4v} symmetry at 0.183. Compared with the results reported in [136], for the C_1 symmetry, the present solution has a more regular topology and a larger bandgap size whereas, for the C_{4v} symmetry, the optimized results are similar in both topology and gap size. The volume fraction of the inclusion material Pb is 0.270 for the C_1 symmetry and 0.323 for the C_{4v} symmetry. The bandgaps are located between the second out-of-plane bandgap and third in-plane bandgap for both C_1 and C_{4v} symmetries.

5.3.2 Hexagonal lattice

In this section, the bandgap maximization of PnCs with the C_1 and C_{6v} hexagonal lattices are carried out. To our best knowledge, topology optimization of asymmetric solid PnCs has never been reported for the hexagonal lattice so far. Thus, the results in this subsection will be meaningful to present a heuristic guide for the design of PnCs with the C_1 and C_{6v} hexagonal lattices.

5.3.2.1 Bandgaps for out-of-plane waves

The first fifteen optimized bandgap structures are presented in Figure 5.10 for the C_{6v} symmetry and Figure 5.11 for the C_1 symmetry with the hexagonal lattice. In analogy to the square lattice, some of the optimized topologies with the high-order bandgaps are rotated and resized from the result with the first bandgap. For C_{6v} symmetry, the bandgap structures with the third, fourth and ninth bandgap are the resized supercell of the result of the first bandgap. For C_1 symmetry, this trend is also observed in more solutions such as the PnCs with the third, fourth, sixth, seventh, ninth, twelfth and thirteenth bandgap.

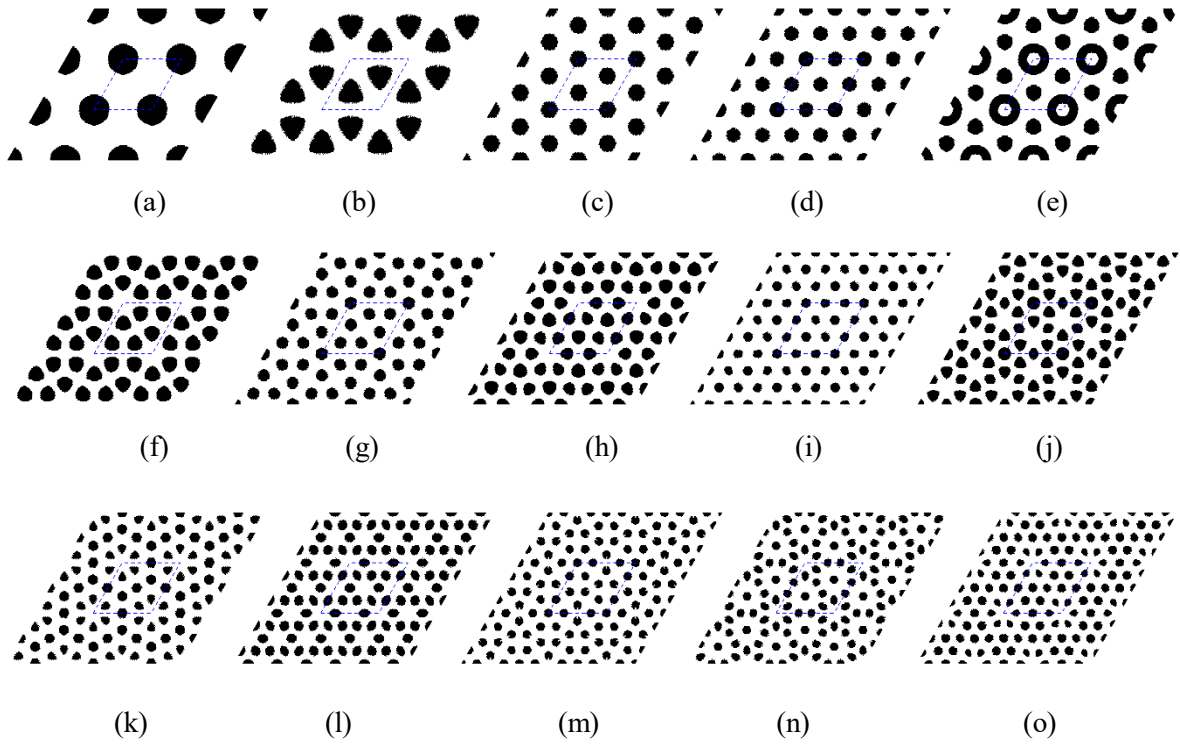


Figure 5.10. Optimized phononic bandgap crystals with the C_{6v} hexagonal lattice from the first bandgap to the fifteenth bandgap for the out-of-plane waves.

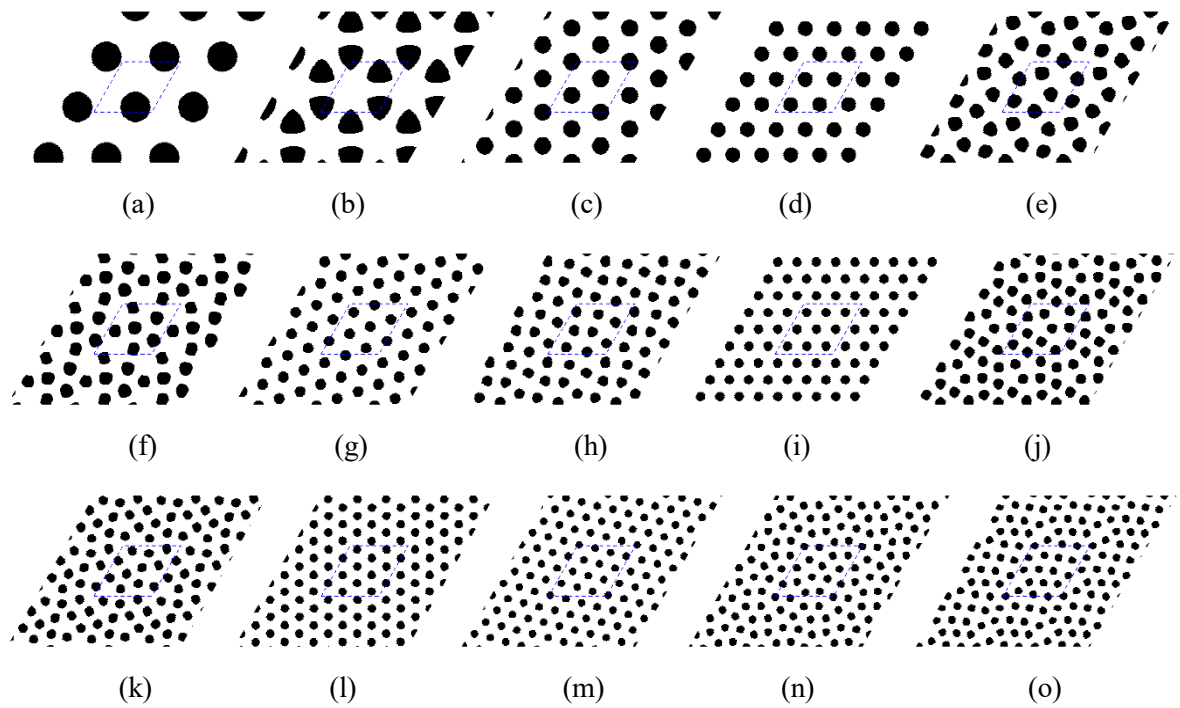


Figure 5.11. Optimized phononic bandgap crystals with C_1 hexagonal lattice from the first bandgap to the fifteenth bandgap for the out-of-plane waves.

Figure 5.12 shows the relative bandgap sizes of the out-of-plane waves with the C_{6v} and C_1 hexagonal lattice. The widest bandgaps for both C_1 and C_{6v} hexagonal lattice are the first bandgap, about 0.77. The pattern is similar to the traditional designs, but the shape of Pb inclusions is a rounded hexagon instead of a circular or a normal hexagonal rod in the traditional designs. Such a material distribution is assumed to be the best topology for the phononic bandgap design with the hexagonal lattice for the out-of-plane wave mode. The second bandgap of phononic crystal with the C_1 hexagonal lattice has the smallest relative size of 0.48. Different from other optimized structures, the C_{6v} hexagonal-latticed phononic crystal with the fifth bandgap consists of a ring-shaped scatter and two circular scatters, and the unusual topology brings it the smallest bandgap of 0.42. The average bandgap size with the C_1 symmetry is 0.70, which is 10.3% higher than the average relative bandgap of the C_{6v} symmetry, 0.63. Compared with the square lattice in the previous section, the symmetry reduction has a greater influence on the hexagonal lattice for the out-of-plane waves.

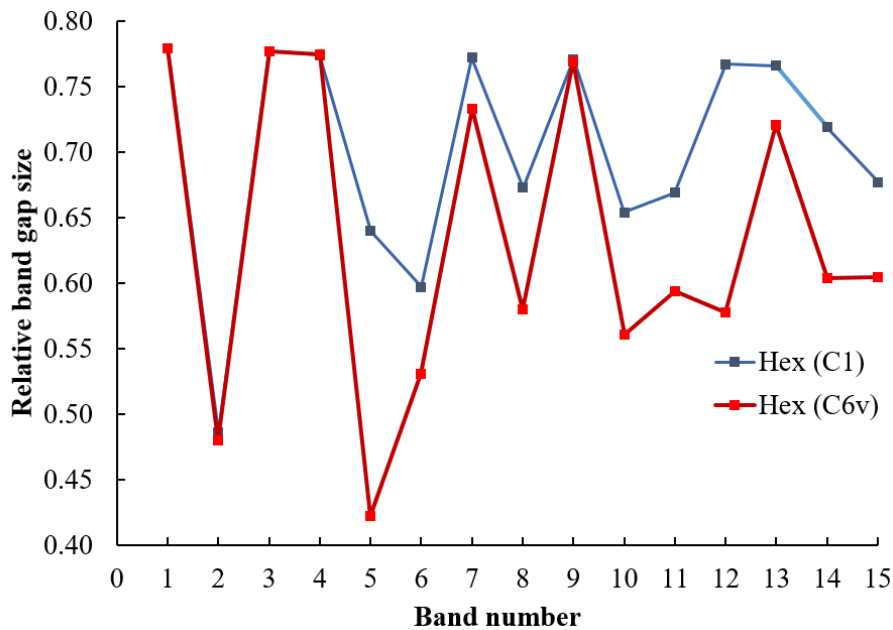


Figure 5.12. Relative phononic bandgap sizes with C_1 and C_{6v} hexagonal lattice from the first bandgap to the fifteenth bandgap for the out-of-plane waves.

5.3.2.2 Bandgaps for in-plane waves

Now we turn to the bandgap size maximization for the in-plane wave mode. The optimized results are obtained in the same method as illustrated in Section 5.3.1.2. Figure 5.13 and Figure 5.14 listed optimized PnCs with the C_{6v} and C_1 hexagonal lattices. The C_{6v} symmetric phononic

crystal with the fifteenth bandgap is different from other results as it consists of three ring-shaped inclusions. This is because the five seeds in the C_{6v} symmetric square-latticed PCVT (Figure A2.5e) are very close to each other, which is too difficult to form a topology with five rod-shaped inclusions.

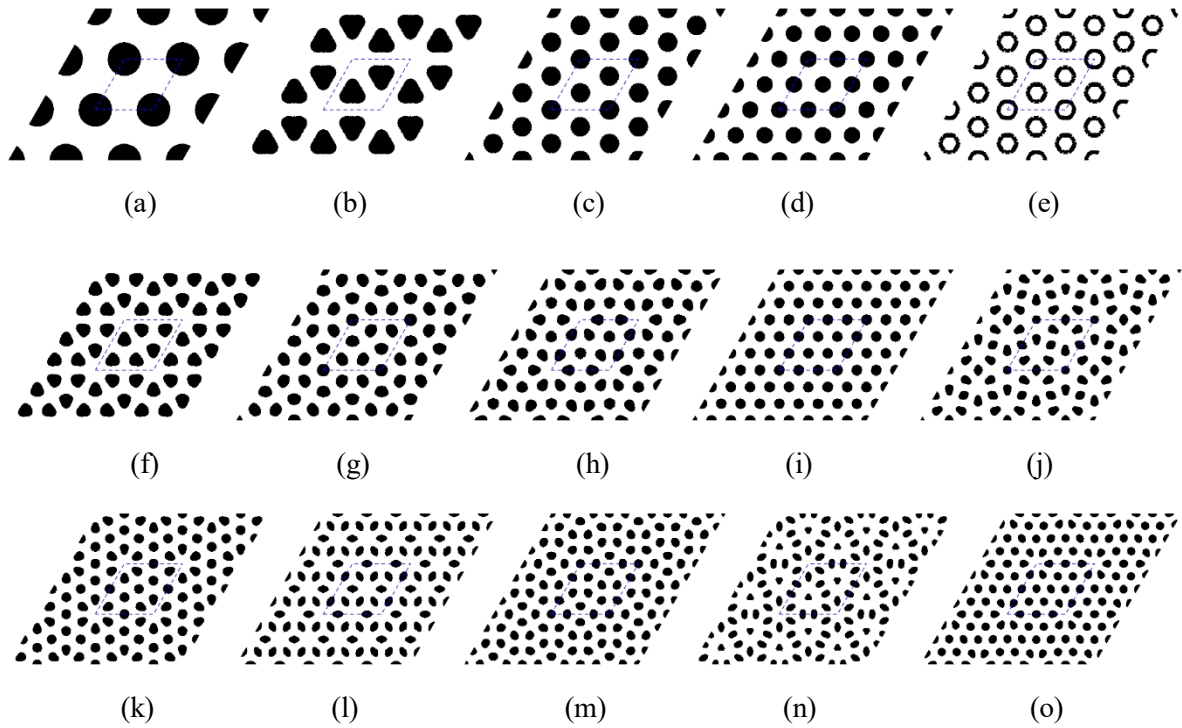
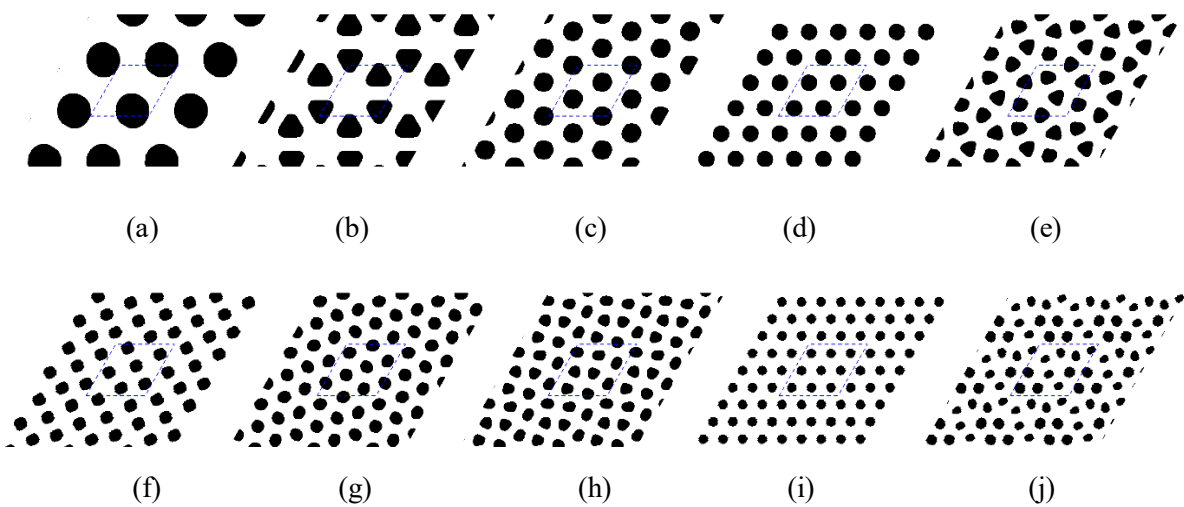


Figure 5.13. Optimized phononic bandgap crystals with C_{6v} hexagonal lattice for the $(3n)^{\text{th}}$ bandgap from $n=1$ to $n=15$ for the in-plane wave mode



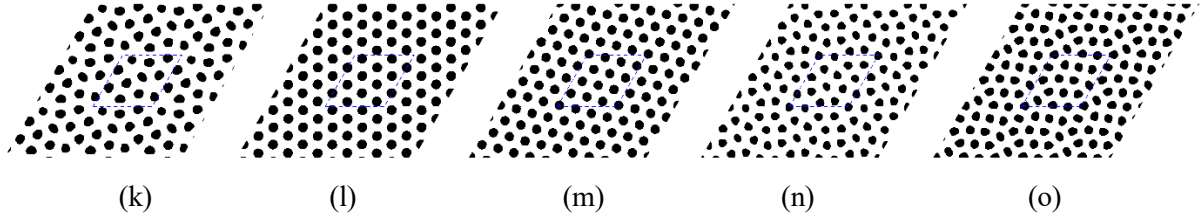


Figure 5.14. Optimized phononic bandgap crystals with C_1 hexagonal lattice for the $(3n)^{\text{th}}$ bandgap from $n=1$ to $n=15$ for the in-plane wave mode

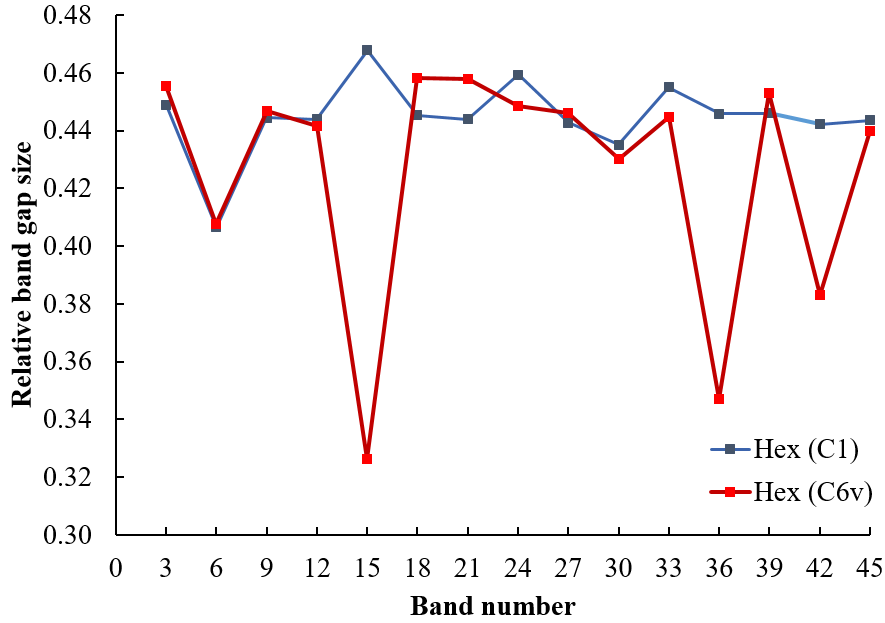


Figure 5.15. Relative phononic bandgap sizes with C_1 and C_{6v} hexagonal lattice with the $(3n)^{\text{th}}$ bandgap from $n=1$ to $n=15$ for the in-plane wave mode

The relative phononic bandgap sizes of the C_1 and C_{6v} hexagonal lattice for the in-plane wave mode are presented in Figure 5.15. The largest bandgap of the C_1 hexagonal lattice appears at the fifteenth bands, about 0.468, increasing by 7% compared with the largest bandgap of the C_{6v} hexagonal lattice, the eighteenth bandgap of 0.458. The narrowest bandgap appears at the sixth bandgap with a size of 0.386 for C_1 symmetry and the fifteenth bandgap with a size of 0.326 for the C_{6v} symmetry. The average bandgap size for the hexagonal lattice with C_1 symmetry is 0.445, having a nearly 4.5% rise compared to designs with C_{4v} symmetry with the size of 0.426. In analogy to the square lattice, we also noticed the results with the C_{6v} symmetry for the eighteenth, twenty-first, and thirty-ninth bandgaps have a slightly larger bandgap than those with the C_1 symmetry at the same bands. At these bands, the symmetric topology might be the best possible solutions.

5.3.2.3 Complete bandgaps for both out-of-plane and in-plane waves

Figure 5.16 gives the optimized PnCs with complete bandgaps and their band diagrams for the C_{6v} and C_1 hexagonal lattice. In analogy to the square lattice, the PnCs with the C_1 hexagonal lattice contains two separate scatters close to each other. However, the PnCs with the C_{6v} hexagonal lattice only have one scatter, which is similar to the previous designs with the first out-of-plane bandgap and the third in-plane bandgap. The complete bandgap size for the C_1 symmetry is 0.215, 35% bigger than that for the C_{6v} symmetry, 0.159. The optimal volume fraction of the inclusion material Pb is 0.298 for the C_1 symmetry and 0.320 for the C_{6v} symmetry. The bandgap for the C_1 symmetry resides between the first out-of-plane bandgap and the third in-plane bandgap; while for the C_{6v} symmetry, the bandgap lies between the second out-of-plane bandgap and the third in-plane bandgap. Due to the C_{6v} symmetry, the hexagonal-latticed phononic crystal can not distribute two inclusions with different sizes in a unit cell; as a result, it failed to open a bandgap between the second out-of-plane bandgap and the third in-plane bandgap.

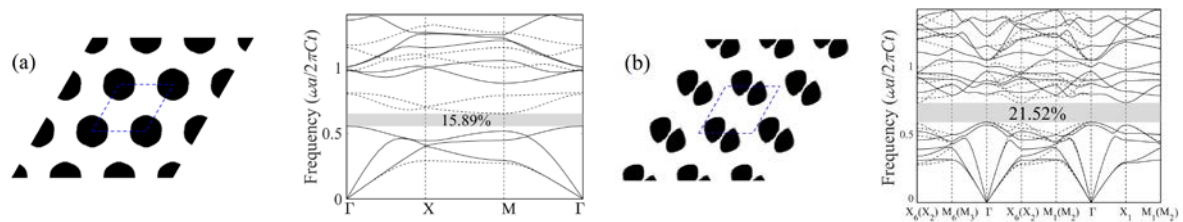


Figure 5.16. Optimized square-latticed phononic bandgap crystals and their band diagrams for the complete bandgap (a) between the first out-of-plane bandgap and the third in-plane bandgap for the C_{6v} symmetry; (b) between the second out-of-plane bandgap and the third in-plane bandgap for the C_1 symmetry. In the band diagrams, dot lines denote the bands of out-of-plane waves and solid lines denote the bands of in-plane waves.

5.4 Conclusion

This chapter has presented the bandgap maximization for two-dimensional symmetric and asymmetric solid PnCs with both square and hexagonal lattices based on FEM and BESO. The PnCs consists of Pb and epoxy. Following a simple method to generate the initial guess designs based on the PCVTs, a number of symmetric and asymmetric designs of PnCs are successfully obtained for the out-of-plane, in-plane, and complete waves for the first time. Among them, the largest bandgaps for square lattices are 0.77 for out-of-plane waves, 0.464 for in-plane waves and 0.273 for combined out-of-plane and in-plane waves, and the largest bandgaps for hexagonal lattices are 0.77 for out-of-plane waves, 0.468 for in-plane waves and 0.215 for

combined out-of-plane and in-plane waves. From our investigations, for any wave modes and lattices, the symmetry reduction have an advantageous effect on the bandgap size. However, the effect varies depending on the band order and the lattice type. For some band orders, the symmetric designs have the bigger gap size and simpler topology than the asymmetric designs; thus, at these band order, the symmetric solutions may be the best choice. For the out-of-plane wave mode, the first bandgap for the C_{6v} hexagonal lattice should be the largest. For the in-plane wave mode, the fifteenth bandgap for the C_1 hexagonal lattice is the optimal choice. The complete bandgap between the second out-of-plane bandgap and the third in-plane bandgap for the C_1 square lattice should be the best option.

Chapter 6. Conclusion of current and future works

6.1 Conclusion of current works

This thesis extended the BESO method to maximize the bandgaps of the six-fold hexagonal-latticed phononic crystals. Based on the developed BESO algorithm, topology optimization of symmetric and asymmetric two-dimensional PnCs is further investigated. Many innovative designs of PnCs with large bandgaps for out-of-plane waves, in-plane waves, and combined out-of-plane and in-plane waves are obtained. The main conclusions of this research are listed as follows:

1. The topology optimization algorithm of the six-fold hexagonal latticed phononic bandgap crystals is established based on BESO. The effectiveness of the proposed method has been demonstrated through numerical examples aiming at finding and maximizing bandgaps of out-of-plane waves, in-plane waves, and combined out-of-plane and in-plane waves.
2. The presupposed lattice type and symmetry in topology optimization have large effects on the resulting solutions. Therefore, topology optimization for both symmetric and asymmetric of square and hexagonal latticed PnCs are also investigated. Generally, asymmetric design exhibits a large bandgap than its symmetric counterpart. However, in some cases, both symmetric and asymmetric designs have the same topologies and bandgap sizes which demonstrate the symmetric ones tend to be truly optimal.
3. For some specified bandgaps of in-plane waves, topology optimization starting from a random initial design is still difficult to obtain the satisfactory solutions due to the coupled longitudinal and transverse waves. From our research, the in-plane bandgap for both square and hexagonal latticed PnCs can be easily achieved by introducing initial guess designs based on the PCVTs.
4. Many novel patterns of the PnCs are presented in this research and provide the useful guidelines in designing the desirable bandgaps of PnCs for various industry applications.

6.2 Future works

Topology optimization is proved to be a powerful technique to achieve broad phononic bandgaps. Based on our current research, the following future works are recommended:

1. Topology optimization of the three-dimensional phononic bandgap crystals is still needed for further investigation.
2. Topology optimization of the phononic bandgap crystals for the surface waves and plate waves is also recommended.
3. Designing the functional phononic devices (e.g., multiplexer, acoustic clocking, waveguide, etc.) based on topology optimization is still lacking.

Appendix 1

Element mass matrix, \mathbf{M}_e , and element stiffness matrix, \mathbf{K}_e , can be evaluated using

For out-of-plane waves:

$$\mathbf{M}_e^{\text{out}} = \rho \int_A \mathbf{N}^T \mathbf{N} dA \quad (\text{A1.1})$$

$$\mathbf{K}_e^{\text{out}} = \mu \int_A \mathbf{K}_1^{\text{out}} + \mathbf{K}_2^{\text{out}} i k_x + \mathbf{K}_3^{\text{out}} i k_y + \mathbf{K}_4^{\text{out}} (k_x^2 + k_y^2) dA \quad (\text{A1.2})$$

where

$$\mathbf{K}_1^{\text{out}} = \frac{\partial \mathbf{N}^T}{\partial x} \frac{\partial \mathbf{N}}{\partial x} + \frac{\partial \mathbf{N}^T}{\partial y} \frac{\partial \mathbf{N}}{\partial y} ;$$

$$\mathbf{K}_2^{\text{out}} = \frac{\partial \mathbf{N}^T}{\partial x} \mathbf{N} - \mathbf{N}^T \frac{\partial \mathbf{N}}{\partial x} ;$$

$$\mathbf{K}_3^{\text{out}} = \frac{\partial \mathbf{N}^T}{\partial y} \mathbf{N} - \mathbf{N}^T \frac{\partial \mathbf{N}}{\partial y} ;$$

$$\mathbf{K}_4^{\text{out}} = \mathbf{N}^T \mathbf{N}$$

For in-plane waves:

$$\mathbf{M}_e^{\text{in}} = \rho \int_A \mathbf{N}^T \mathbf{N} dA \quad (\text{A1.3})$$

$$\mathbf{K}_e^{\text{in}} = \int_A \mathbf{K}_1^{\text{in}} + \mathbf{K}_2^{\text{in}} i k_x + \mathbf{K}_3^{\text{in}} i k_y + \mathbf{K}_4^{\text{in}} k_x^2 + \mathbf{K}_5^{\text{in}} k_y^2 + \mathbf{K}_6^{\text{in}} k_x k_y dA \quad (\text{A1.4})$$

where A denotes the area of an element; and

$$\mathbf{K}_1^{\text{in}} = \mathbf{B}_1^T \mathbf{C} \mathbf{B}_1 ;$$

$$\mathbf{K}_2^{\text{in}} = \mathbf{B}_1^T \mathbf{C} \mathbf{B}_2 - \mathbf{B}_2^T \mathbf{C} \mathbf{B}_1;$$

$$\mathbf{K}_3^{\text{in}} = \mathbf{B}_1^T \mathbf{C} \mathbf{B}_3 - \mathbf{B}_3^T \mathbf{C} \mathbf{B}_1;$$

$$\mathbf{K}_4^{\text{in}} = \mathbf{B}_2^T \mathbf{C} \mathbf{B}_2;$$

$$\mathbf{K}_5^{\text{in}} = \mathbf{B}_3^T \mathbf{C} \mathbf{B}_3;$$

$$\mathbf{K}_6^{\text{in}} = \mathbf{B}_2^T \mathbf{C} \mathbf{B}_3 + \mathbf{B}_3^T \mathbf{C} \mathbf{B}_2 \quad ;$$

$$\mathbf{C} = \begin{bmatrix} \lambda + 2\mu & \lambda & 0 \\ \lambda & \lambda + 2\mu & 0 \\ 0 & 0 & \mu \end{bmatrix};$$

$$\mathbf{B}_1 = \mathbf{L}_1 \frac{\partial \mathbf{N}}{\partial x} + \mathbf{L}_2 \frac{\partial \mathbf{N}}{\partial y}; \quad \mathbf{B}_2 = \mathbf{L}_1 \mathbf{N}; \quad \mathbf{B}_3 = \mathbf{L}_2 \mathbf{N};$$

$$\mathbf{L}_1 = \begin{bmatrix} 1 & 0 \\ 0 & 0 \\ 0 & 1 \end{bmatrix}; \quad \mathbf{L}_2 = \begin{bmatrix} 0 & 0 \\ 0 & 1 \\ 1 & 0 \end{bmatrix}$$

where \mathbf{N} the shape functions of an element with respect to out-of-plane waves and in-plane waves. The shape functions are given below

For out-of-plane waves:

$$\mathbf{N} = [N_1 \quad N_2 \quad N_3 \quad N_4]$$

For in-plane waves:

$$\mathbf{N} = \begin{bmatrix} N_1 & 0 & N_2 & 0 & N_3 & 0 & N_4 & 0 \\ 0 & N_1 & 0 & N_2 & 0 & N_3 & 0 & N_4 \end{bmatrix}$$

In order to discretize rhombus unit cells, the linear 4-node square and rhombus elements are used for square and hexagonal lattice. The shape functions can be expressed with local

coordinates (ξ, η) as

$$N_1 = \frac{1}{4}(1-\xi)(1-\eta);$$

$$N_2 = \frac{1}{4}(1+\xi)(1-\eta);$$

$$N_3 = \frac{1}{4}(1+\xi)(1+\eta);$$

$$N_4 = \frac{1}{4}(1-\xi)(1+\eta).$$

The derivative of the shape functions \mathbf{N} is

$$\begin{bmatrix} \frac{\partial N_1}{\partial x} & \frac{\partial N_2}{\partial x} & \frac{\partial N_3}{\partial x} & \frac{\partial N_4}{\partial x} \\ \frac{\partial N_1}{\partial y} & \frac{\partial N_2}{\partial y} & \frac{\partial N_3}{\partial y} & \frac{\partial N_4}{\partial y} \end{bmatrix} = \mathbf{J}^{-1} \begin{bmatrix} \frac{\partial N_1}{\partial \xi} & \frac{\partial N_2}{\partial \xi} & \frac{\partial N_3}{\partial \xi} & \frac{\partial N_4}{\partial \xi} \\ \frac{\partial N_1}{\partial \eta} & \frac{\partial N_2}{\partial \eta} & \frac{\partial N_3}{\partial \eta} & \frac{\partial N_4}{\partial \eta} \end{bmatrix}$$

where \mathbf{J} is the Jacobian matrix

$$\mathbf{J} = \frac{1}{4} \begin{bmatrix} \frac{2a}{n_x} & 0 \\ a & \sqrt{3}a \\ n_x & n_y \end{bmatrix} \text{ for hexagonal lattice and } \mathbf{J} = \frac{1}{2} \begin{bmatrix} \frac{a}{n_x} & 0 \\ 0 & \frac{a}{n_y} \end{bmatrix} \text{ for square lattice,}$$

where a is the lattice constant and n_x, n_y are the total numbers of elements along two sides of the unit cell.

The differential element mass matrix and element stiffness matrix with respect to design variable x_e , are:

For out-of-plane waves:

$$\frac{\partial \mathbf{M}_e^{\text{out}}}{\partial x_e} = (\rho_2 - \rho_1) \int_A \mathbf{N}^T \mathbf{N} dA$$

$$\frac{\partial \mathbf{K}_e^{\text{out}}}{\partial x_e} = (\mu_2 - \mu_1) \int_A \mathbf{K}_1^{\text{out}} + \mathbf{K}_2^{\text{out}} i k_x + \mathbf{K}_3^{\text{out}} i k_y + \mathbf{K}_4^{\text{out}} (k_x^2 + k_y^2) dA$$

For in-plane waves:

$$\frac{\partial \mathbf{M}_e^{\text{in}}}{\partial x_e} = (\rho_2 - \rho_1) \int_A \mathbf{N}^T \mathbf{N} dA$$

$$\frac{\partial \mathbf{K}_e^{\text{in}}}{\partial x_e} = \int_A \frac{\partial \mathbf{K}_1^{\text{in}}}{\partial x_e} + \frac{\partial \mathbf{K}_2^{\text{in}}}{\partial x_e} i k_x + \frac{\partial \mathbf{K}_3^{\text{in}}}{\partial x_e} i k_y + \frac{\partial \mathbf{K}_4^{\text{in}}}{\partial x_e} k_x^2 + \frac{\partial \mathbf{K}_5^{\text{in}}}{\partial x_e} k_y^2 + \frac{\partial \mathbf{K}_6^{\text{in}}}{\partial x_e} k_x k_y dA$$

$\frac{\partial \mathbf{K}_n^{\text{in}}}{\partial x_e}$ ($n=1, 2, \dots, 6$) can be calculated by replacing \mathbf{C} with $\frac{\partial \mathbf{C}}{\partial x_e}$ in equation (A4)

$$\frac{\partial \mathbf{C}}{\partial x_e} = \begin{bmatrix} (\lambda_2 - \lambda_1) + 2(\mu_2 - \mu_1) & (\lambda_2 - \lambda_1) & 0 \\ (\lambda_2 - \lambda_1) & (\lambda_2 - \lambda_1) + 2(\mu_2 - \mu_1) & 0 \\ 0 & 0 & (\mu_2 - \mu_1) \end{bmatrix}$$

Appendix 2

In order to achieve PCVTs, we first introduce the concept of Voronoi tessellation and centroidal Voronoi tessellation, then by applying periodic boundary condition, we can compute PCVT easily.

The Voronoi tessellation can be achieved by generating n random points in a domain D , followed by computing the Voronoi tessellation in the domain D .

In the two dimensional cases, the Voronoi tessellation is a partitioning of the domain D which is a plane and a bounded convex 2D shape. A set of points $\{\mathbf{z}_i\}_{i \geq 1}$ (called seeds) will be randomly scattered in D , based on which, D will be divided into n Voronoi regions V_i defined by

$$V_i = \{\mathbf{x}(x, y) \in D \mid \|\mathbf{x} - \mathbf{z}_i\| < \|\mathbf{x} - \mathbf{z}_j\| \text{ for } j \geq 1, j \neq i\} \quad (\text{A2.1})$$

where any points in a Voronoi region V_i is closest to the corresponding seed z_i .

For a given Voronoi region V , the mass center (or centroid) \mathbf{z}^* of V is

$$\mathbf{z}_i^* = \frac{\int_{V_i} \mathbf{x} \rho(\mathbf{x}) d\mathbf{x}}{\int_{V_i} \rho(\mathbf{x}) d\mathbf{x}} \quad (\text{A2.2})$$

Repeat (1) computing Voronoi tessellation according to the seeds by eqn. (A2.1), (2) calculating new centroids by equation (A2.2), and regard the new centroids as seeds for the next iteration to start with. Then the centroidal Voronoi tessellation (CVT) is obtained until the newly calculated centroids coincide with the old centroids in the last iteration. See Figure A2.1 as an illustration for a square domain and a rhombus domain at $n = 4$.

In our case, we need to apply the periodic condition to the unit cell. An easy method to replicate 8 neighboring unit cells of the primary cell, forming a 3×3 array. In this way, the periodic Voronoi tessellation can be easily calculated by computing the 3×3 array. The Voronoi regions which lay in the primary cell constitute the PCVT. An example has been shown in

Figure A2.2 for a square domain and a rhombus domain at $n=4$, where grey shaded areas are the primary unit cells; white areas are 8 neighboring unit cells and red dots represent the centroids in their Voronoi regions.

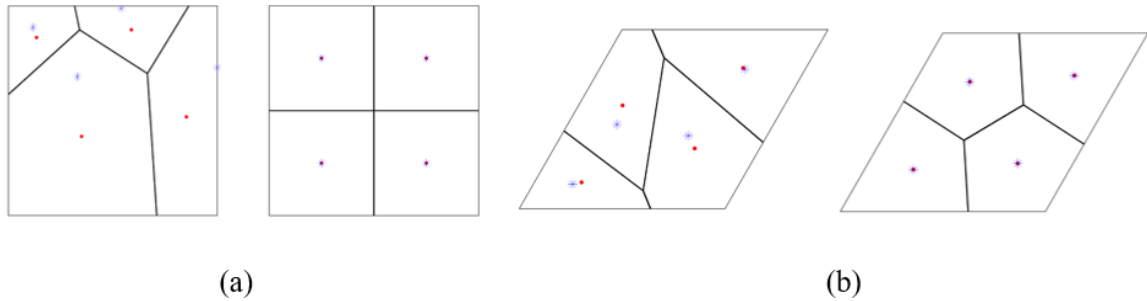


Figure A2.1. VTs and CVTs at $n=4$ for (a) square domain (b) hexagonal domain. Left: VT, Right: CVT. Blue stars are seeds and red dots indicate centroids. Voronoi regions are divided by black solid lines.

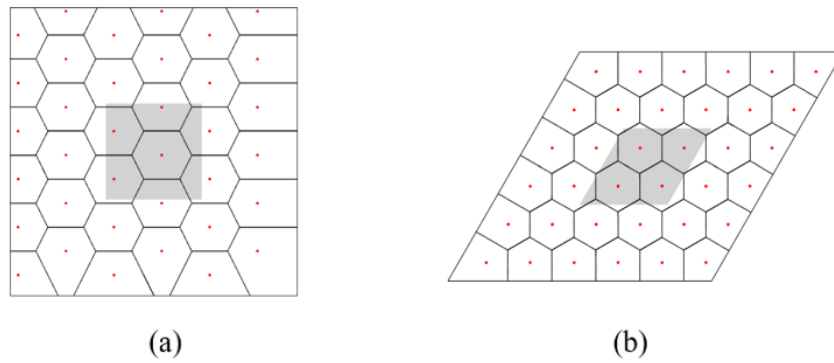


Figure A2.2. PCVTs with C_1 symmetry at $n = 4$ for (a) square domain (b) hexagonal domain

The symmetry can also be applied by initially placing the seeds meeting the symmetric requirement. Then the resulting periodic centroidal voronoi diagram will automatically be symmetric as well.

The first fifteen PCVTs for symmetric square lattice are listed in Figure A2.3, asymmetric square lattice in Figure A2.4, symmetric hexagonal lattice in Figure A2.5 and asymmetric hexagonal lattice in Figure A2.6, respectively. It is noted that the results vary depending on the initial distribution of the seeds [149]. Figure A2.4-A2.6 only lists the most possible results for each number of seeds.

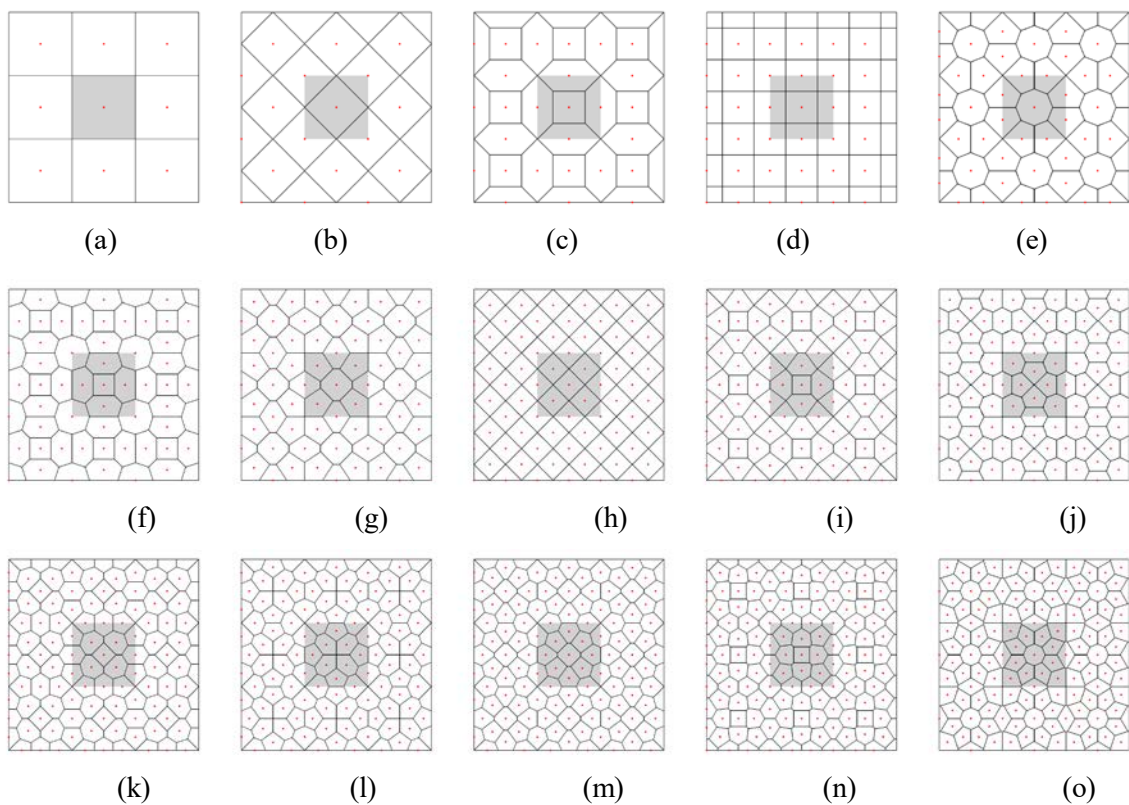


Figure A2.3. PCVTs for square unit cells with C_{4v} symmetry from $n=1$ to $n=15$

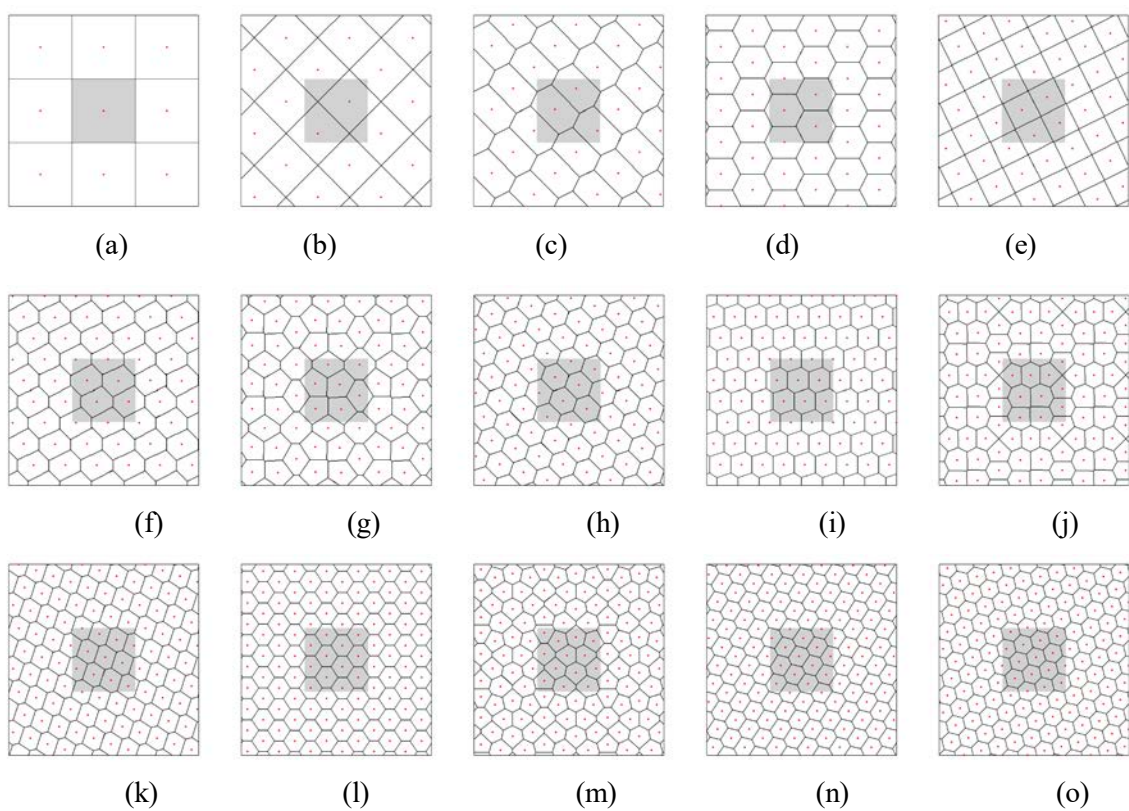


Figure A2.4. PCVTs for square unit cells with C_1 symmetry from $n=1$ to $n=15$

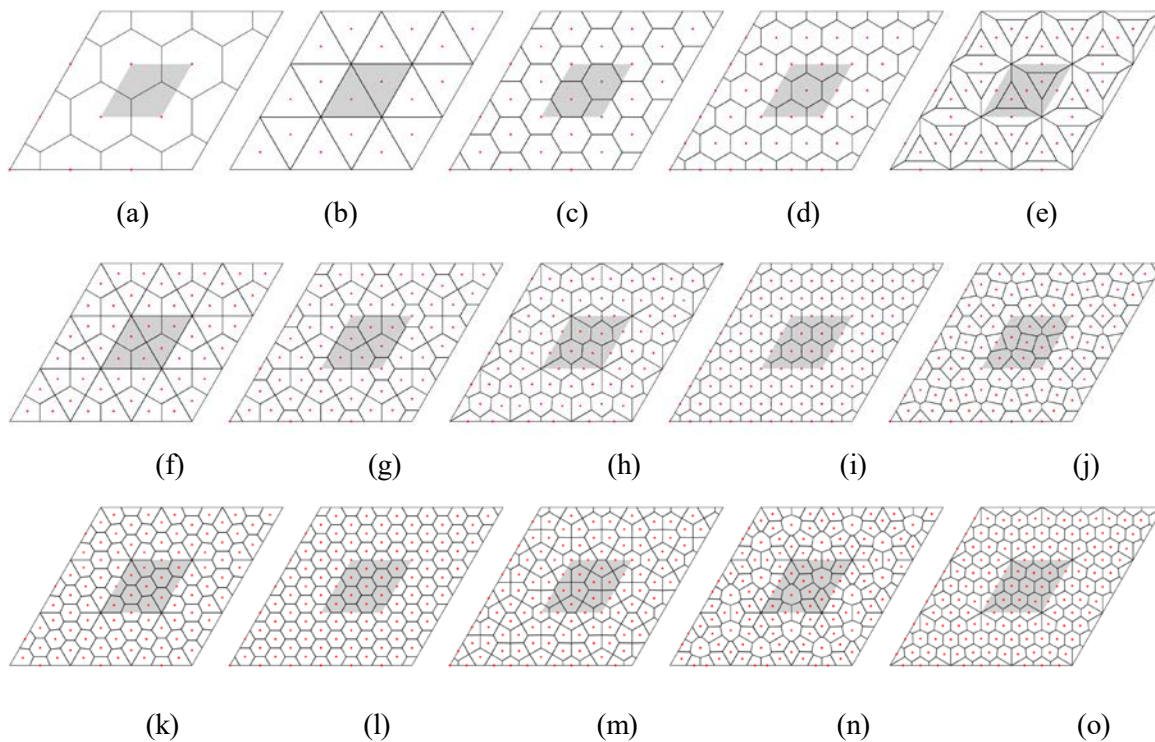


Figure A2.5. PCVTs for hexagonal unit cells with C_{6v} symmetry from $n=1$ to $n=15$

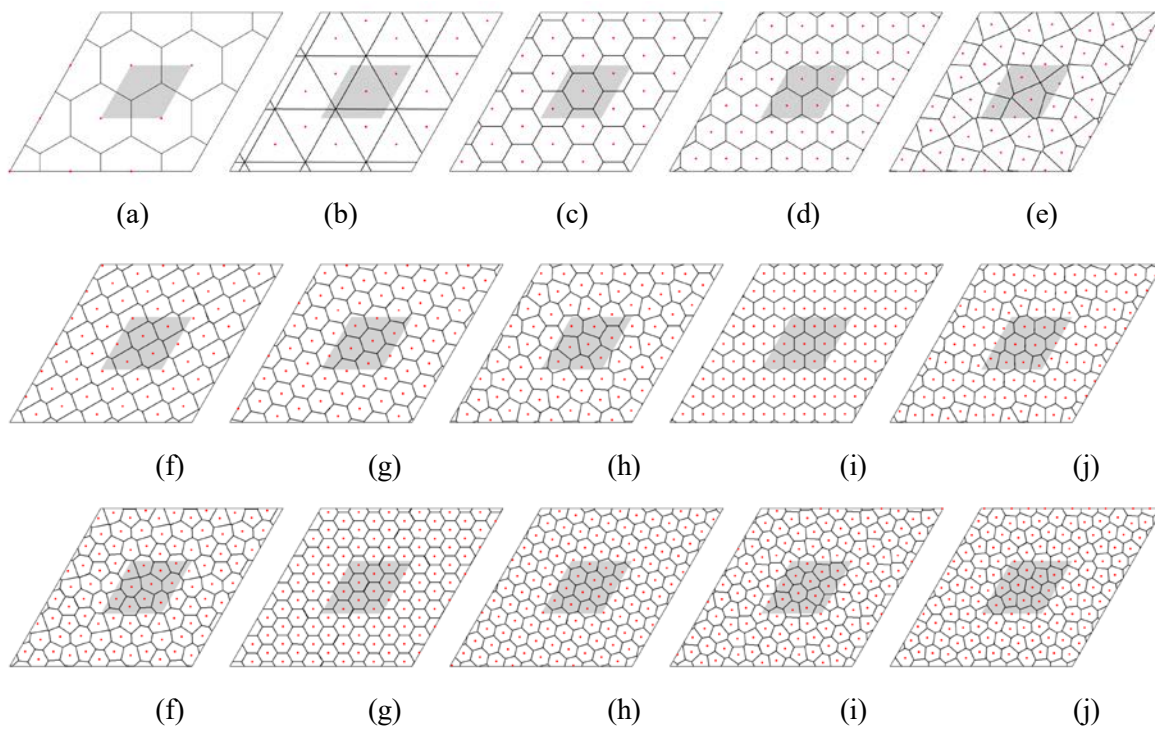


Figure A2.6. PCVTs for hexagonal unit cells with C_1 symmetry from $n=1$ to $n=15$

References:

1. Yablonovitch, E 1987, 'Inhibited spontaneous emission in solid-state physics and electronics', *Physical review letters*, vol. 58, no. 20, p. 2059.
2. John, S 1987, 'Strong localization of photons in certain disordered dielectric superlattices', *Physical review letters*, vol. 58, no. 23, p. 2486.
3. Sigalas, MM & Economou, EN 1992, 'Elastic and acoustic wave band structure', *Journal of sound and vibration*, vol. 158, no. 2, p. 377.
4. Kushwaha, MS, Halevi, P, Dobrzynski, L & Djafari-Rouhani, B 1993, 'Acoustic band structure of periodic elastic composites', *Physical review letters*, vol. 71, no. 13, p. 2022.
5. Martinezsala, R, Sancho, J, Sánchez, JV, Gómez, V, Llinares, J & Meseguer, F 1995, 'Sound-attenuation by sculpture', *nature*, vol. 378, no. 6554, p. 241.
6. Pennec, Y, Vasseur, JO, Djafari-Rouhani, B, Dobrzyński, L & Deymier, PA 2010, 'Two-dimensional phononic crystals: Examples and applications', *Surface Science Reports*, vol. 65, no. 8, p. 229.
7. Khelif, A, Choujaa, A, Benchabane, S, Djafari-Rouhani, B & Laude, V 2004, 'Guiding and bending of acoustic waves in highly confined phononic crystal waveguides', *Applied Physics Letters*, vol. 84, no. 22, p. 4400-.
8. Christensen, J, Fernandez-Dominguez, A, de Leon-Perez, F, Martin-Moreno, L & Garcia-Vidal, F 2007, 'Collimation of sound assisted by acoustic surface waves', *Nature Physics*, vol. 3, no. 12, p. 851.
9. Zhang, XD & Liu, ZY 2004, 'Negative refraction of acoustic waves in two-dimensional phononic crystals', *Applied Physics Letters*, vol. 85, no. 2, p. 341.
10. Morvan, B, Tinel, A, Hladky-Hennion, A-C, Vasseur, J & Dubus, B 2010, 'Experimental demonstration of the negative refraction of a transverse elastic wave in a two-dimensional solid phononic crystal', *Applied Physics Letters*, vol. 96, no. 10, p. 101905.
11. Vasseur, J, Djafari-Rouhani, B, Dobrzynski, L & Deymier, P 1997, 'Acoustic band gaps in fibre composite materials of boron nitride structure', *Journal of Physics: Condensed Matter*, vol. 9, no. 35, p. 7327.
12. Kushwaha, M & Halevi, P 1994, 'Band-gap engineering in periodic elastic composites', *Applied Physics Letters*, vol. 64, no. 9, p. 1085.
13. Min, R, Wu, F, Zhong, L, Zhong, H, Zhong, S & Liu, Y 2006, 'Extreme acoustic band gaps obtained under high symmetry in 2D phononic crystals', *Journal of Physics D: Applied Physics*, vol. 39, no. 10, p. 2272.
14. Su, XX, Wang, YF & Wang, YS 2012, 'Effects of Poisson's ratio on the band gaps and

- defect states in two-dimensional vacuum/solid porous phononic crystals', *Ultrasonics*, vol. 52, no. 2, p. 255.
15. Zhou, XZ, Wang, YS & Zhang, C 2009, 'Effects of material parameters on elastic band gaps of two-dimensional solid phononic crystals', *Journal of Applied Physics*, vol. 106, no. 1, p. 014903.
 16. Sigalas, M & Economou, E 1993, 'Band structure of elastic waves in two dimensional systems', *Solid State Communications*, vol. 86, no. 3, p. 141.
 17. Sigmund, O & Jensen, JS 2003, 'Systematic design of phononic band-gap materials and structures by topology optimization', *Philosophical Transactions of the Royal Society of London A: Mathematical, Physical and Engineering Sciences*, vol. 361, no. 1806, p. 1001.
 18. Gazonas, GA, Weile, DS, Wildman, R & Mohan, A 2006, 'Genetic algorithm optimization of phononic bandgap structures', *International journal of solids and structures*, vol. 43, no. 18, p. 5851.
 19. Hui-Lin, Z, Fu-Gen, W & Li-Ning, Y 2006, 'Application of genetic algorithm in optimization of band gap of two-dimensional phononic crystals', *Acta Physica Sinica*, vol. 55, no. 1, p. 275.
 20. Dong, HW, Su, XX, Wang, YS & Zhang, C 2014, 'Topological optimization of two-dimensional phononic crystals based on the finite element method and genetic algorithm', *Structural and Multidisciplinary Optimization*, vol. 50, no. 4, p. 593.
 21. Li, YF, Huang, X & Zhou, S 2016, 'Topological design of cellular phononic band gap crystals', *Materials*, vol. 9, no. 3, p. 186.
 22. Li, YF, Huang, X, Meng, F & Zhou, S 2016, 'Evolutionary topological design for phononic band gap crystals', *Structural and Multidisciplinary Optimization*, vol. 54, no. 3, p. 595.
 23. Meng, F, Li, Y, Li, S, Lin, H, Jia, B & Huang, X 2017, 'Achieving large band gaps in 2D symmetric and asymmetric photonic crystals', *Journal of Lightwave Technology*, vol. 35, no. 9, p. 1670.
 24. Wang, R, Wang, X-H, Gu, B-Y & Yang, G-Z 2001, 'Effects of shapes and orientations of scatterers and lattice symmetries on the photonic band gap in two-dimensional photonic crystals', *Journal of Applied Physics*, vol. 90, no. 9, p. 4307.
 25. Malkova, N, Kim, S, Dilazaro, T & Gopalan, V 2003, 'Symmetrical analysis of complex two-dimensional hexagonal photonic crystals', *Physical Review B*, vol. 67, no. 12, p. 125203.
 26. Kuang, W, Hou, Z & Liu, Y 2004, 'The effects of shapes and symmetries of scatterers on the phononic band gap in 2D phononic crystals', *Physics Letters A*, vol. 332, no. 5, pp. 481-490.

27. Putnis, A 1992. *An introduction to mineral sciences*. Cambridge University Press.
28. Esquivel-Sirvent, R & Coccoletzi, G 1994, 'Band structure for the propagation of elastic waves in superlattices', *The Journal of the Acoustical Society of America*, vol. 95, no. 1, p. 86.
29. Dowling, JP 1992, 'Sonic band structure in fluids with periodic density variations', *The Journal of the Acoustical Society of America*, vol. 91, no. 5, p. 2539.
30. Wu, F, Liu, Z & Liu, Y 2002, 'Acoustic band gaps in 2D liquid phononic crystals of rectangular structure', *Journal of Physics D: Applied Physics*, vol. 35, no. 2, p. 162.
31. Kafesaki, M, Sigalas, M & Economou, E 1995, 'Elastic wave band gaps in 3-D periodic polymer matrix composites', *Solid state communications*, vol. 96, no. 5, p. 285.
32. Kushwaha, M & Djafari-Rouhani, B 1996, 'Complete acoustic stop bands for cubic arrays of spherical liquid balloons', *Journal of applied physics*, vol. 80, no. 6, p. 3191.
33. Vasseur, J, Deymier, P, Frantziskonis, G, Hong, G, Djafari-Rouhani, B & Dobrzynski, L 1998, 'Experimental evidence for the existence of absolute acoustic band gaps in two-dimensional periodic composite media', *Journal of Physics: Condensed Matter*, vol. 10, no. 27, p. 6051.
34. Kushwaha, MS, Halevi, P, Martinez, G, Dobrzynski, L & Djafari-Rouhani, B 1994, 'Theory of acoustic band structure of periodic elastic composites', *Physical Review B*, vol. 49, no. 4, p. 2313.
35. Economou, E & Sigalas, M 1993, 'Classical wave propagation in periodic structures: Cermet versus network topology', *Physical Review B*, vol. 48, no. 18, p. 13434.
36. De Espinosa, FM, Jimenez, E & Torres, M 1998, 'Ultrasonic band gap in a periodic two-dimensional composite', *Physical Review Letters*, vol. 80, no. 6, p. 1208.
37. Sigalas, M & Economou, E 1996, 'Attenuation of multiple-scattered sound', *EPL (Europhysics Letters)*, vol. 36, no. 4, p. 241.
38. Kushwaha, MS 1997, 'Stop-bands for periodic metallic rods: Sculptures that can filter the noise', *Applied Physics Letters*, vol. 70, no. 24, p. 3218.
39. Garcia-Pablos, D, Sigalas, M, De Espinosa, FM, Torres, M, Kafesaki, M & Garcia, N 2000, 'Theory and experiments on elastic band gaps', *Physical Review Letters*, vol. 84, no. 19, p. 4349.
40. Laude, V 2015, *Phononic crystals: artificial crystals for sonic, acoustic, and elastic waves*, Walter de Gruyter GmbH & Co KG.
41. Liu, Y, Su, JY & Gao, L 2008, 'The influence of the micro-topology on the phononic band gaps in 2D porous phononic crystals', *Physics Letters A*, vol. 372, no. 45, pp. 6784.
42. Maldovan, M 2013, 'Sound and heat revolutions in phononics', *Nature*, vol. 503, no. 7475, p. 209.

43. Kushwaha, M & Djafari-Rouhani, B 1998, 'Giant sonic stop bands in two-dimensional periodic system of fluids', *Journal of Applied Physics*, vol. 84, no. 9, p. 4677.
44. Wu, F, Liu, Z & Liu, Y 2002, 'Acoustic band gaps created by rotating square rods in a two-dimensional lattice', *Physical Review E*, vol. 66, no. 4, p. 046628.
45. Lai, Y & Zhang, ZQ 2003, 'Large band gaps in elastic phononic crystals with air inclusions', *Applied physics letters*, vol. 83, no. 19, p. 3900.
46. Wu, TT, Huang, ZG & Lin, S 2004, 'Surface and bulk acoustic waves in two-dimensional phononic crystal consisting of materials with general anisotropy', *Physical review B*, vol. 69, no. 9, p. 094301.
47. Vasseur, J, Deymier, P, Khelif, A, Lambin, P, Djafari-Rouhani, B, Akjouj, A, Dobrzynski, L, Fettouhi, N & Zemmouri, J 2002, 'Phononic crystal with low filling fraction and absolute acoustic band gap in the audible frequency range: A theoretical and experimental study', *Physical Review E*, vol. 65, no. 5, p. 056608.
48. Zhou, XZ, Wang, YS & Zhang, C 2009, 'Effects of material parameters on elastic band gaps of two-dimensional solid phononic crystals', *Journal of Applied Physics*, vol. 106, no. 1, p. 014903.
49. Tanaka, Y & Tamura, SI 1998, 'Surface acoustic waves in two-dimensional periodic elastic structures', *Physical Review B*, vol. 58, no. 12, p. 7958.
50. Tanaka, Y & Tamura, SI 1999, 'Acoustic stop bands of surface and bulk modes in two-dimensional phononic lattices consisting of aluminum and a polymer', *Physical Review B*, vol. 60, no. 19, p. 13294.
51. Laude, V, Wilm, M, Benchabane, S & Khelif, A 2005, 'Full band gap for surface acoustic waves in a piezoelectric phononic crystal', *Physical Review E*, vol. 71, no. 3, p. 036607.
52. Pennec, Y, Djafari-Rouhani, B, Larabi, H, Vasseur, J & Hladky-Hennion, A 2008, 'Low-frequency gaps in a phononic crystal constituted of cylindrical dots deposited on a thin homogeneous plate', *Physical Review B*, vol. 78, no. 10, p. 104105.
53. Khelif, A, Aoubiza, B, Mohammadi, S, Adibi, A & Laude, V 2006, 'Complete band gaps in two-dimensional phononic crystal slabs', *Physical Review E*, vol. 74, no. 4, p. 046610.
54. Vasseur, J, Deymier, P, Djafari-Rouhani, B, Pennec, Y & Hladky-Hennion, A 2008, 'Absolute forbidden bands and waveguiding in two-dimensional phononic crystal plates', *Physical Review B*, vol. 77, no. 8, p. 085415.
55. Khelif, A, Achaoui, Y, Benchabane, S, Laude, V & Aoubiza, B 2010, 'Locally resonant surface acoustic wave band gaps in a two-dimensional phononic crystal of pillars on a surface', *Physical Review B*, vol. 81, no. 21, p. 214303.
56. Mohammadi, S, Eftekhar, A, Khelif, A, Moubchir, H, Westafer, R, Hunt, W & Adibi,

- A 2007, 'Complete phononic bandgaps and bandgap maps in two-dimensional silicon phononic crystal plates', *Electronics Letters*, vol. 43, no. 16, pp. 898-899.
57. Liu, Z, Zhang, X, Mao, Y, Zhu, Y, Yang, Z, Chan, CT & Sheng, P 2000, 'Locally resonant sonic materials', *Science*, vol. 289, no. 5485, p. 1734.
 58. Croënne, C, Lee, E, Hu, H & Page, J 2011, 'Band gaps in phononic crystals: Generation mechanisms and interaction effects', *AIP Advances*, vol. 1, no. 4, p. 041401.
 59. Yi, G & Youn, BD 2016, 'A comprehensive survey on topology optimization of phononic crystals', *Structural and Multidisciplinary Optimization*, vol. 54, no. 5, p. 1315.
 60. Sigalas, M & Economou, EN 1993, 'Band structure of elastic waves in two dimensional systems', *Solid State Communications*, vol. 86, no. 3, p. 141.
 61. Cao, Y, Hou, Z & Liu, Y 2004, 'Finite difference time domain method for band-structure calculations of two-dimensional phononic crystals', *Solid state communications*, vol. 132, no. 8, p. 539.
 62. Tanaka, Y, Tomoyasu, Y & Tamura, SI 2000, 'Band structure of acoustic waves in phononic lattices: Two-dimensional composites with large acoustic mismatch', *Physical Review B*, vol. 62, no. 11, p. 7387.
 63. Veres, IA, Berer, T & Matsuda, O 2013, 'Complex band structures of two dimensional phononic crystals: Analysis by the finite element method', *Journal of Applied Physics*, vol. 114, no. 8, p. 083519.
 64. Psarobas, I, Stefanou, N & Modinos, A 2000, 'Scattering of elastic waves by periodic arrays of spherical bodies', *Physical Review B*, vol. 62, no. 1, p. 278.
 65. Zhang, Y, Ni, Z, Han, L, Zhang, ZM & Chen, H 2011, 'Study of improved plane wave expansion method on phononic crystal', *Optoelectron Adv Mater*, vol. 5, no. 8, p. 870.
 66. Taflove, A & Hagness, SC 2005, *Computational electrodynamics: the finite-difference time-domain method*, Artech house.
 67. Gedney, SD 2011, 'Introduction to the finite-difference time-domain (FDTD) method for electromagnetics', *Synthesis Lectures on Computational Electromagnetics*, vol. 6, no. 1, p. 1.
 68. Lucklum, R, Ke, M & Zubtsov, M 2012, 'Two-dimensional phononic crystal sensor based on a cavity mode', *Sensors and Actuators B: Chemical*, vol. 171, p. 271.
 69. Khelif, A, Choujaa, A, Djafari-Rouhani, B, Wilm, M, Ballandras, S & Laude, V 2003, 'Trapping and guiding of acoustic waves by defect modes in a full-band-gap ultrasonic crystal', *physical Review B*, vol. 68, no. 21, p. 214301.
 70. Sun, JH & Wu, TT 2006, 'Propagation of surface acoustic waves through sharply bent two-dimensional phononic crystal waveguides using a finite-difference time-domain

- method', *Physical Review B*, vol. 74, no. 17, p. 174305.
71. Sun, JH & Wu, TT 2007, 'Propagation of acoustic waves in phononic-crystal plates and waveguides using a finite-difference time-domain method', *Physical Review B*, vol. 76, no. 10, p. 104304.
 72. Su, XX, Li, JB & Wang, YS 2010, 'A postprocessing method based on high-resolution spectral estimation for FDTD calculation of phononic band structures', *Physica B: Condensed Matter*, vol. 405, no. 10, p. 2444.
 73. Hrennikoff, A 1941, 'Solution of problems of elasticity by the framework method', *Journal of applied mechanics*, vol. 8, no. 4, p. 169.
 74. Courant, R 1943, 'Variational methods for the solution of problems of equilibrium and vibrations', *Bulletin of the American mathematical Society*, vol. 49, no. 1, p. 1.
 75. Meng, F, Huang, X & Jia, B 2015, 'Bi-directional evolutionary optimization for photonic band gap structures', *Journal of Computational Physics*, vol. 302, p. 393.
 76. Badreddine Assouar, M & Oudich, M 2011, 'Dispersion curves of surface acoustic waves in a two-dimensional phononic crystal', *Applied Physics Letters*, vol. 99, no. 12, p. 123505.
 77. Li, H, Tian, Y, Ke, Y, He, S & Luo, W 2014, 'Analysis of Rayleigh surface acoustic waves propagation on piezoelectric phononic crystal with 3-D finite element model,' *Ultrasonics Symposium (IUS), 2014 IEEE International*, IEEE, p. 2533.
 78. Yao, ZJ, Yu, GL & Wang, YS 2013, 'Point Defect States of Phononic Crystal Thin Plates—An Application of Finite Element Method,' *Advanced Materials Research*, Trans Tech Publ, p. 1419.
 79. Dong, HW, Su, XX & Wang, Y-S 2014, 'Multi-objective optimization of two-dimensional porous phononic crystals', *Journal of Physics D: Applied Physics*, vol. 47, no. 15, p. 155301.
 80. Vatanabe, SL, Paulino, GH & Silva, EC 2014, 'Maximizing phononic band gaps in piezocomposite materials by means of topology optimization', *The Journal of the Acoustical Society of America*, vol. 136, no. 2, p. 494.
 81. Yang, S, Page, JH, Liu, Z, Cowan, ML, Chan, CT & Sheng, P 2004, 'Focusing of sound in a 3D phononic crystal', *Physical review letters*, vol. 93, no. 2, p. 024301.
 82. Bucay, J, Roussel, E, Vasseur, J, Deymier, P, Hladky-Hennion, A, Pennec, Y, Muralidharan, K, Djafari-Rouhani, B & Dubus, B 2009, 'Positive, negative, zero refraction, and beam splitting in a solid/air phononic crystal: Theoretical and experimental study', *Physical Review B*, vol. 79, no. 21, p. 214305.
 83. Liang, B, Guo, X, Tu, J, Zhang, D & Cheng, J 2010, 'An acoustic rectifier', *Nature materials*, vol. 9, no. 12, p. 989.

84. Pennec, Y, Djafari-Rouhani, B, Vasseur, JO, Khelif, A and Deymier, PA 2004. 'Tunable filtering & demultiplexing in phononic crystals with hollow cylinders', *Physical Review E*, vol 69, no 4, p.046608.
85. Chen, H & Chan, C 2007, 'Acoustic cloaking in three dimensions using acoustic metamaterials', *Applied physics letters*, vol. 91, no. 18, p. 183518.
86. Torrent, D & Sánchez-Dehesa, J 2008, 'Acoustic cloaking in two dimensions: a feasible approach', *New Journal of Physics*, vol. 10, no. 6, p. 063015.
87. Brûlé, S, Javelaud, E, Enoch, S & Guenneau, S 2014, 'Experiments on seismic metamaterials: Molding surface waves', *Physical review letters*, vol. 112, no. 13, p. 133901.
88. Wen, J, Wang, G, Yu, D, Zhao, H & Liu, Y 2005, 'Theoretical and experimental investigation of flexural wave propagation in straight beams with periodic structures: Application to a vibration isolation structure', *Journal of Applied Physics*, vol. 97, no. 11, p. 114907.
89. Cheng, Z & Shi, Z 2013, 'Novel composite periodic structures with attenuation zones', *Engineering Structures*, vol. 56, p. 1271.
90. Yan, Y, Cheng, Z, Menq, F, Mo, Y, Tang, Y & Shi, Z 2015, 'Three dimensional periodic foundations for base seismic isolation', *Smart Materials and Structures*, vol. 24, no. 7, p. 075006.
91. Xiang, H, Shi, Z, Wang, S & Mo, Y 2012, 'Periodic materials-based vibration attenuation in layered foundations: experimental validation', *Smart Materials and Structures*, vol. 21, no. 11, p. 112003.
92. Yan, Y, Laskar, A, Cheng, Z, Menq, F, Tang, Y, Mo, Y & Shi, Z 2014, 'Seismic isolation of two dimensional periodic foundations', *Journal of Applied Physics*, vol. 116, no. 4, p. 044908.
93. Cheng, Z & Shi, Z 2014, 'Vibration attenuation properties of periodic rubber concrete panels', *Construction and Building Materials*, vol. 50, p. 257.
94. Shin, H, Qiu, W, Jarecki, R, Cox, JA, Olsson III, RH, Starbuck, A, Wang, Z & Rakich, PT 2013, 'Tailorable stimulated Brillouin scattering in nanoscale silicon waveguides', *Nature communications*, vol. 4, p. 1944.
95. Yao, Y, Wu, F, Hou, Z & Liu, Y 2007, 'Propagation properties of elastic waves in semi-infinite phononic crystals and related waveguides', *The European Physical Journal B-Condensed Matter and Complex Systems*, vol. 58, no. 4, p. 353.
96. Khelif, A, Deymier, P, Djafari-Rouhani, B, Vasseur, J & Dobrzynski, L 2003, 'Two-dimensional phononic crystal with tunable narrow pass band: Application to a waveguide with selective frequency', *Journal of applied physics*, vol. 94, no. 3, p. 1308.
97. Chandra, H, Deymier, P & Vasseur, J 2004, 'Elastic wave propagation along

- waveguides in three-dimensional phononic crystals', *Physical Review B*, vol. 70, no. 5, p. 054302.
98. Benchabane, S, Gaiffe, O, Salut, R, Ulliac, G, Laude, V & Kokkonen, K 2015, 'Guidance of surface waves in a micron-scale phononic crystal line-defect waveguide', *Applied Physics Letters*, vol. 106, no. 8, p. 081903.
 99. Sun, JH & Wu, TT 2005, 'Analyses of mode coupling in joined parallel phononic crystal waveguides', *Physical Review B*, vol. 71, no. 17, p. 174303.
 100. Veselago, VG 1968, 'The electrodynamics of substances with simultaneously negative values of ϵ and μ ', *Soviet physics uspekhi*, vol. 10, no. 4, p. 509.
 101. Luo, C, Johnson, SG, Joannopoulos, J & Pendry, J 2002, 'All-angle negative refraction without negative effective index', *Physical Review B*, vol. 65, no. 20, p. 201104.
 102. Sukhovich, A, Jing, L & Page, JH 2008, 'Negative refraction and focusing of ultrasound in two-dimensional phononic crystals', *Physical Review B*, vol. 77, no. 1, p. 014301.
 103. Li, J & Chan, C 2004, 'Double-negative acoustic metamaterial', *Physical Review E*, vol. 70, no. 5, p. 055602.
 104. Zhang, P, Valfells, Á, Ang, LK, Luginsland, JW & Lau, YY 2017. '100 years of the physics of diodes', *Applied Physics Reviews*, vol. 4, no. 1, p. 011304.
 105. Liang, B, Yuan, B & Cheng, JC 2009, 'Acoustic diode: Rectification of acoustic energy flux in one-dimensional systems', *Physical review letters*, vol. 103, no. 10, p. 104301.
 106. Boehler, N, Theocharis, G & Daraio, C 2011, 'Bifurcation-based acoustic switching and rectification', *Nature materials*, vol. 10, no. 9, p. 665.
 107. Li, XF, Ni, X, Feng, L, Lu, MH, He, C & Chen, YF 2011, 'Tunable unidirectional sound propagation through a sonic-crystal-based acoustic diode', *Physical review letters*, vol. 106, no. 8, p. 084301.
 108. Hwan Oh, J, Woong Kim, H, Sik Ma, P, Min Seung, H & Young Kim, Y 2012, 'Inverted bi-prism phononic crystals for one-sided elastic wave transmission applications', *Applied Physics Letters*, vol. 100, no. 21, p. 213503.
 109. Yuan, B, Liang, B, Tao, J-C, Zou, X-Y & Cheng, J-C 2012, 'Broadband directional acoustic waveguide with high efficiency', *Applied Physics Letters*, vol. 101, no. 4, p. 043503.
 110. Song, AL, Chen, TN, Wang, XP & Wan, L-L 2016, 'Waveform-preserved unidirectional acoustic transmission based on impedance-matched acoustic metasurface and phononic crystal', *Journal of Applied Physics*, vol. 120, no. 8, p. 085106.
 111. Zhu, X, Zou, X, Liang, B & Cheng, J 2010, 'One-way mode transmission in one-dimensional phononic crystal plates', *Journal of Applied Physics*, vol. 108, no. 12, p.

124909.

112. Cicek, A, Adem Kaya, O & Ulug, B 2012, 'Refraction-type sonic crystal junction diode', *Applied Physics Letters*, vol. 100, no. 11, p. 111905.
113. Li, RQ, Liang, B, Li, Y, Kan, W-W, Zou, XY & Cheng, J-C 2012, 'Broadband asymmetric acoustic transmission in a gradient-index structure', *Applied Physics Letters*, vol. 101, no. 26, p. 263502.
114. Huang, X & Xie, YM 2010, *Evolutionary topology optimization of continuum structures: methods and applications*, John Wiley & Sons.
115. Michell, AGM 1904, 'LVIII. The limits of economy of material in frame-structures', *The London, Edinburgh, and Dublin Philosophical Magazine and Journal of Science*, vol. 8, no. 47, p. 589.
116. Bendsøe, MP & Kikuchi, N 1988, 'Generating optimal topologies in structural design using a homogenization method', *Computer methods in applied mechanics and engineering*, vol. 71, no. 2, p. 197.
117. Hassani, B & Hinton, E 1998, 'A review of homogenization and topology optimization I—homogenization theory for media with periodic structure', *Computers & Structures*, vol. 69, no. 6, p. 707.
118. Bendsøe, MP & Sigmund, O 2003 *Topology Optimization: Theory, Methods and Applications*, Springer.
119. van Dijk, NP, Maute, K, Langelaar, M & Van Keulen, F 2013, 'Level-set methods for structural topology optimization: a review', *Structural and Multidisciplinary Optimization*, vol. 48, no. 3, p. 437.
120. Xie, YM & Steven, GP 1993, 'A simple evolutionary procedure for structural optimization', *Computers & structures*, vol. 49, no. 5, p. 885.
121. Xie, YM & Steven, GP 1997, 'Basic evolutionary structural optimization', in *Evolutionary Structural Optimization*, Springer, p. 12.
122. Querin, O, Steven, G & Xie, YM 1998, 'Evolutionary structural optimisation (ESO) using a bidirectional algorithm', *Engineering computations*, vol. 15, no. 8, p. 1031.
123. Kumar, M, Husian, M, Upreti, N & Gupta, D 2010, 'Genetic algorithm: Review and application', *International Journal of Information Technology and Knowledge Management*, vol. 2, no. 2, p. 451.
124. Mullen, RJ, Monekosso, D, Barman, S & Remagnino, P 2009, 'A review of ant algorithms', *Expert systems with Applications*, vol. 36, no. 6, p. 9608.
125. Gen, M & Cheng, R 2000, *Genetic algorithms and engineering optimization*, John Wiley & Sons.
126. Mitchell, M 1998, *An introduction to genetic algorithms*, MIT press.

127. Bendsøe, MP 1989, 'Optimal shape design as a material distribution problem', *Structural and multidisciplinary optimization*, vol. 1, no. 4, p. 193.
128. Sigmund, O & Maute, K 2013, 'Topology optimization approaches', *Structural and Multidisciplinary Optimization*, vol. 48, no. 6, p. 1031.
129. Rozvany, GI 2009, 'A critical review of established methods of structural topology optimization', *Structural and multidisciplinary optimization*, vol. 37, no. 3, p. 217.
130. Huang, X & Xie, YM 2007, 'Convergent and mesh-independent solutions for the bi-directional evolutionary structural optimization method', *Finite Elements in Analysis and Design*, vol. 43, no. 14, p. 1039.
131. Li, Q, Steven, G & Xie, YM 2001, 'A simple checkerboard suppression algorithm for evolutionary structural optimization', *Structural and Multidisciplinary Optimization*, vol. 22, no. 3, p. 230.
132. Rozvany, GI & Querin, OM 2002, 'Combining ESO with rigorous optimality criteria', *International journal of vehicle design*, vol. 28, no. 4, p. 294.
133. Huang, X, Li, Y, Zhou, S & Xie, YM 2014, 'Topology optimization of compliant mechanisms with desired structural stiffness', *Engineering Structures*, vol. 79, p. 13.
134. Hussein, MI, Hamza, K, Hulbert, GM, Scott, RA & Saitou, K 2006, 'Multiobjective evolutionary optimization of periodic layered materials for desired wave dispersion characteristics', *Structural and Multidisciplinary Optimization*, vol. 31, no. 1, p. 60.
135. Hussein, MI, Hamza, K, Hulbert, GM & Saitou, K 2007, 'Optimal synthesis of 2D phononic crystals for broadband frequency isolation', *Waves in Random and Complex Media*, vol. 17, no. 4, p. 491.
136. Dong, HW, Su, XX, Wang, YS & Zhang, C 2014, 'Topology optimization of two-dimensional asymmetrical phononic crystals', *Physics Letters A*, vol. 378, no. 4, p. 434.
137. Chen, Y, Huang, X, Sun, G, Yan, X & Li, G 2017, 'Maximizing spatial decay of evanescent waves in phononic crystals by topology optimization', *Computers & Structures*, vol. 182, p. 430.
138. Bilal, OR & Hussein, MI 2012, 'Topologically evolved phononic material: breaking the world record in band gap size', *SPIE OPTO*, p. 826911.
139. Dong, HW, Wang, YS, Wang, YF & Zhang, C 2015, 'Reducing symmetry in topology optimization of two-dimensional porous phononic crystals', *AIP Advances*, vol. 5, no. 11, p. 117149.
140. Kittel, C 2005, *Introduction to solid state physics*, Wiley.
141. Huang, X, Zuo, Z & Xie, YM 2010, 'Evolutionary topological optimization of vibrating continuum structures for natural frequencies', *Computers & structures*, vol. 88, no. 5, p. 357.

142. Sigmund, O & Hougaard, K 2008, 'Geometric properties of optimal photonic crystals', *Physical review letters*, vol. 100, no. 15, p. 153904.
143. Villeneuve, PR & Piche, M 1992, 'Photonic band gaps in two-dimensional square and hexagonal lattices', *Physical Review B*, vol. 46, no. 8, p. 4969.
144. Li, YF, Meng, F, Li, S, Jia, B, Zhou, S & Huang, X 2017 'Optimal design of phononic band gaps for in-plane modes', *accepted by Physical Letter A*,
145. Laude, V, Achaoui, Y, Benchabane, S & Khelif, A 2009, 'Evanescent Bloch waves and the complex band structure of phononic crystals', *Physical Review B*, vol. 80, no. 9, p. 092301.
146. Deymier, PA 2013, *Acoustic metamaterials and phononic crystals*, Springer Science & Business Media.
147. Wen, F, David, S, Checoury, X, El Kurdi, M & Boucaud, P 2008, 'Two-dimensional photonic crystals with large complete photonic band gaps in both TE and TM polarizations', *Optics express*, vol. 16, no. 16, p. 12278.
148. Zhang, J, Emelianenko, M & Du, Q 2012, 'PERIODIC CENTROIDAL VORONOI TESSELLATIONS', *International Journal of Numerical Analysis & Modeling*, vol. 9, no. 4, p. 950
149. Yan, D-M, Wang, K, Lévy, B & Alonso, L 2011, 'Computing 2D periodic centroidal Voronoi tessellation,' *Voronoi Diagrams in Science and Engineering (ISVD), 2011 Eighth International Symposium on*, IEEE, p 177.

List of publications

1. Zhang, Z, Li, YF, Meng, F & Huang X 2017, 'Topological design of phononic band gap crystals with sixfold symmetric hexagonal lattice', *Computational Materials Science*, vol. 139, p. 97.
2. Zhang, Z, Li, YF, Meng, F and Huang X 'Optimal design of 2D asymmetric phononic bandgap crystals' (In preparation).